Strojniški vestnik
Journal of Mechanical Engineering

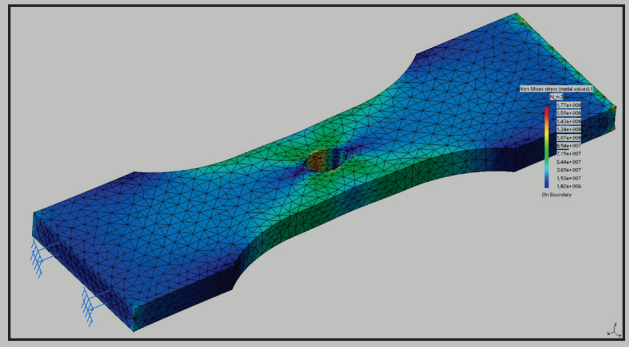

no. 5
year 2019
volume 65

Strojniški vestnik – Journal of Mechanical Engineering (SV-JME)

Aim and Scope
The international journal publishes original and (mini)review articles covering the concepts of materials science, mechanics, kinematics, thermodynamics, energy and environment, mechatronics and robotics, fluid mechanics, tribology, cybernetics, industrial engineering and structural analysis.
The journal follows new trends and progress proven practice in the mechanical engineering and also in the closely related sciences as are electrical, civil and process engineering, medicine, microbiology, ecology, agriculture, transport systems, aviation, and others, thus creating a unique forum for interdisciplinary or multidisciplinary dialogue.
The international conferences selected papers are welcome for publishing as a special issue of SV-JME with invited co-editor(s).

Editorial Office
University of Ljubljana, Faculty of Mechanical Engineering
SV-JME, Aškerčeva 6, SI-1000 Ljubljana, Slovenia
Phone: 386 (0)1 4771 137
Fax: 386 (0)1 2518 567
info@sv-jme.eu, http://www.sv-jme.eu

Print: Papirografika, printed in 300 copies

Founders and Publishers
University of Ljubljana, Faculty of Mechanical Engineering, Slovenia
University of Maribor, Faculty of Mechanical Engineering, Slovenia
Association of Mechanical Engineers of Slovenia
Chamber of Commerce and Industry of Slovenia, Metal Processing Industry Association

Cover:
Simulations of product's behaviour under operating conditions represent a foundation of a contemporary product design. Despite the immense processing power and complex simulation tools it is still impossible to fully predict the product's response to real operating conditions. Therefore, the experimental testing is a complementary supplement of simulations in every R&D process.

Image courtesy:
University of Ljubljana, Faculty of Mechanical Engineering, Laboratory for Structure Evaluation, Slovenia

ISSN 0039-2480, ISSN 2536-2948 (online)

General information
Strojniški vestnik – Journal of Mechanical Engineering is published in 11 issues per year (July and August is a double issue).

Institutional prices include print & online access: institutional subscription price and foreign subscription €100,00 (the price of a single issue is €10,00); general public subscription and student subscription €50,00 (the price of a single issue is €5,00). Prices are exclusive of tax. Delivery is included in the price. The recipient is responsible for paying any import duties or taxes. Legal title passes to the customer on dispatch by our distributor. Single issues from current and recent volumes are available at the current single-issue price. To order the journal, please complete the form on our website. For submissions, subscriptions and all other information please visit: *http://www.sv-jme.eu.*

You can advertise on the inner and outer side of the back cover of the journal. The authors of the published papers are invited to send photos or pictures with short explanation for cover content.

We would like to thank the reviewers who have taken part in the peer-review process.

The journal is subsidized by Slovenian Research Agency.

Strojniški vestnik - Journal of Mechanical Engineering is available on *https://www.sv-jme.eu*.

Contents

Strojniški vestnik - Journal of Mechanical Engineering
volume 65, (2019), number 5
Ljubljana, may 2019
ISSN 0039-2480

Published monthly

Papers

Jernej Klemenc, Bojan Podgornik: An Improved Model for Predicting the Scattered S-N Curves 265
Xi Zhang, Tianlu Zhang, Xiangyu Geng, Jianfeng Hong, Jinjun Wu: Study on the Effects of Hierarchical Wavy Morphology on Clearance Flow 276
Xianbin Du, Youqun Zhao, Qiang Wang, Hongxun Fu, Fen Lin: Grounding Characteristics of a Non-Pneumatic Mechanical Elastic Tire in a Rolling State with a Camber Angle 287
Jiwen Chen, Xin Li, Hongjuan Yang, Chen Wang: Innovative Design of a Vertical and Transverse Elevator in Double Shafts, Based on TRIZ Theory 297
Abdulrahaman Shuaibu Ahmad, Wu Yunxin, Gong Hai, Liu Lei: Determination of the Effect of Cold Working Compression on Residual Stress Reduction in Quenched Aluminium Alloy 2219 Block 311
Alexey Fomin, Wsevolod Ivanov: Development of a Mixing Mechanism with a Complex Motion of the End-effector 319

Strojniški vestnik - Journal of Mechanical Engineering 65(2019)5, 265-275

DOI:10.5545/sv-jme.2018.5918 Original Scientific Paper
Received for review: 2018-12-07
Received revised form: 2019-04-24
Accepted for publication: 2019-05-10

An Improved Model for Predicting the Scattered S-N Curves

Jernej Klemenc[1,*] – Bojan Podgornik[2]
[1]University of Ljubljana, Faculty of Mechanical Engineering, Slovenia
[2]Institute of Metals and Technology, Slovenia

In this article an improved neural network model is presented that allows us to predict the scattered S-N curves. The model is capable of predicting the S-N curve in its high-cycle and very-high-cycle fatigue domains by considering also the increased scatter of the fatigue-life data below the knee point of the S-N curve. The scatter of the fatigue-life data for an arbitrary amplitude-stress level is modelled with a two-parametric Weibull's probability density function, the parameters of which are varied as a function of the amplitude-stress level. The parameters of the S-N curve trend and its scatter distribution are not fixed, but depend on the parameters of the production process via a serial-hybrid neural network. The article presents the theoretical background and the application in the case of real experimental fatigue data for 51CrV4 spring steel manufactured with two different manufacturing technologies and two different heat treatments.
Keywords: 51CrV4 steel, conventional manufacturing technology, electro-slag remelting, S-N curve, serial hybrid neural network

Highlights
- *A model for predicting S-N curves and their scatter for 51CrV4 steel was built.*
- *The model is capable of predicting the S-N curves in the transition zone between high-cycle and very high-cycle fatigue domains.*
- *The scatter of S-N curves is described by Weibull probability density function.*
- *The model is based on a serial hybrid neural network.*

0 INTRODUCTION

To evaluate structural reliability of dynamically loaded components it is necessary to know the scatter of the loading spectra as well as the scatter of the fatigue-life durability curve of the structural material **[1]** to **[7]**. Structures that are made from spring steels are typically subjected to a large number of load cycles. For this reason, a S-N fatigue-life curve is normally used to predict the fatigue life of such structures. In the past it was presumed that a fatigue-life limit $S_{a;FL}$ exists at a certain number of load-cycles-to-failure N_{FL}, e.g., for structural steels the fatigue-life limit should occur between 2×10^6 **[8]** and 10^8 **[9]** load-cycles-to-failure, see Fig. 1. However, it turned out that for most metallic structural materials there is no fatigue-life limit **[10]**. What exists in practice is a so-called Haibach's knee point, below which the slope of the S-N curve is reduced. This part of the S-N curve is usually referred to as a very-high-cycle domain. Haibach **[11]** proposed a model for the S-N curve in which the slope below its knee-point is $2k$–1, if its slope in the high-cycle domain is k, see Fig. 1.

Additionally many other researchers have shown that the slope of the S-N curve in the very-high-cycle domain is reduced (**[12]** to **[14]**). What is common to all these cases is that, not only the slope, but also the scatter of the experimental fatigue-life data, is significantly changed (i.e. increased) below the knee point of the S-N curve, see Fig. 2.

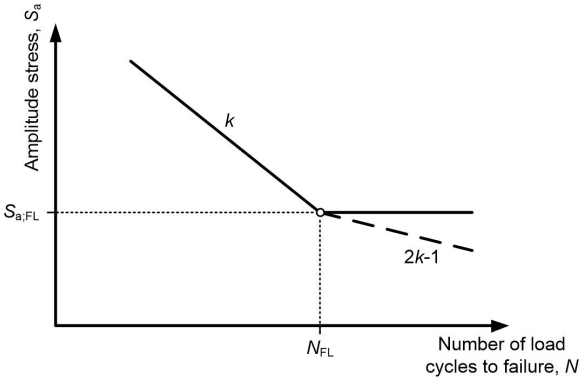

Fig. 1. *A S-N fatigue-life curve*

It was further shown **[13]** and **[14]** that the slope of the fatigue-life curve in the very-high-cycle domain is much smaller than the one proposed by Haibach. In order to make reliable predictions of the structure's fatigue life in the high-cycle and very-high-cycle domains one must be able to model the variable trend as well as the variable scatter of the number of load-cycles-to-failure for these two domains of the S-N curve.

The shape of the S-N curve in the vast neighbourhood of the knee point between the high-cycle and very-high-cycle fatigue domains of the S-N

*Corr. Author's Address: University of Ljubljana, Faculty of Mechanical Engineering , Aškerčeva 6, 1000 Ljubljana, Slovenia jernej.klemenc@fs.uni-lj.si

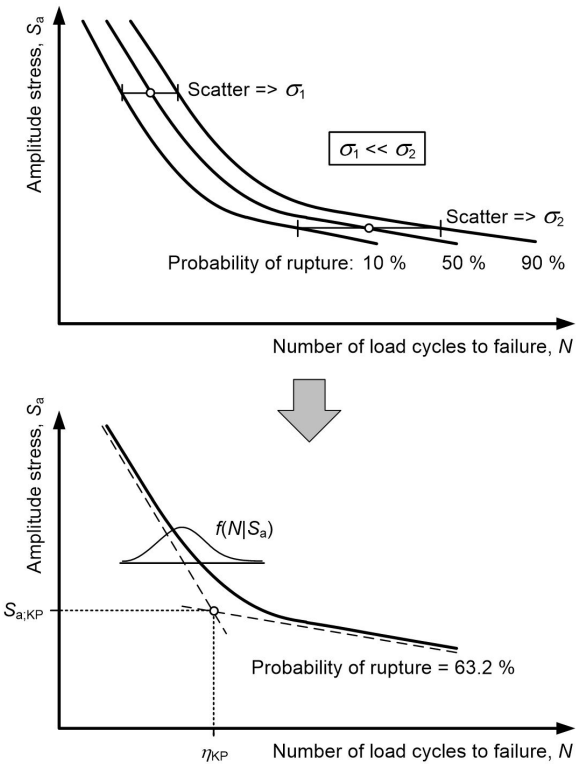

Fig. 2. *Scatter of the S-N curve in the high-cycle and very-high-cycle fatigue domains*

curve is similar to the shape of the Coffin-Manson curve **[15]** in the neighbourhood of the transition between the low-cycle elastic-plastic domain and the high-cycle elastic domain of the fatigue-life curve. For this reason it is possible to model the S-N curve in the high-cycle and the very-high-cycle domains with a similar form:

$$S_a = a \cdot N^{-b} + c \cdot N^{-(b+d)}; \quad a,b,c,d > 0, \qquad (1)$$

where S_a represents the amplitude stress, N is the number of load-cycles-to-failure and *a, b, c, d* are parameters dependent on the material. We have shown before **[16]** that it is possible to model the fatigue-life curve of such a shape together with its scatter by applying a Weibull's two-parametric probability density function (PDF) to describe the scatter of the number of load-cycles-to-failure for an arbitrary amplitude-stress level:

$$N \to f(N \mid S_a) = \frac{\beta}{\eta} \cdot \left(\frac{N}{\eta}\right)^{\beta-1} \cdot \exp\left[-\left(\frac{N}{\eta}\right)^{\beta}\right]. \qquad (2)$$

In that study we have presumed that the Weibull's scale parameter η (which represents the number of load-cycles-to-failure at a 0.632 probability of rupture) was dependent on the amplitude-strain level ε_a via Coffin-Manson equation and that the Weibull's shape parameter β was constant **[16]**. However, there is a huge difference between the scatter of the ε-N curve and the scatter around the knee point between the high-cycle and very-high-cycle domains of the S-N curve. While the width of the scatter band of the ε-N curve is constant below and above its knee point, this is not the case for the knee point between the high-cycle and very-high-cycle domains of the S-N curve. In the latter case, the width of the scatter band of the S-N curve in the very-high-cycle domain is much larger than in the high-cycle domain, see Fig. 2. For this reason it is not possible to describe the scatter of such durability curve using a two-parametric Weibull PDF from Eq. (2) with a constant shape parameter β. On the contrary, to model the S-N curve around the knee point between the high-cycle and very-high-cycle fatigue domains the Weibull's shape parameter β should also depend on the amplitude-stress level S_a.

The objective was to build a model for predicting the S-N curves and their scatter for a specific spring steel. Since the material's characteristics depend on the manufacturing technology and the heat treatment of such steels, these influential factors should be considered when modelling the corresponding S-N curves. The S-N curves can vary a great deal between differently produced and/or heat-treated steels, even for similar operating conditions. That is why we decided to apply a serial hybrid neural networks to build the model that is able to predict the S-N curve and its scatter as a function of the manufacturing technology and the heat treatment. A similar approach was successfully applied before, for modelling the dependence of the S-N and ε-N curves on the operating conditions (**[17]** and **[18]**). In the scientific literature there exist a number of articles on the application of neural networks for modelling and predicting durability curves. However, most of them are based on either multi-layer perceptrons or basis functions. With such an approach it is difficult to embed into a neural network an analytical model that is capable for predicting trend and scatter of the durability curve. Since the approach from Klemenc et al. **[18]** was proved to be successful we modified it in such a way that a new model is capable of predicting the S-N curve in its high-cycle and very-high-cycle fatigue domains by considering also the increased scatter of the fatigue-life data below the knee point of the S-N curve. The manufacturing technology and the heat treatment were the inputs to the neural network and the parameters of the S-N curve and its scatter were its outputs.

Such a comprehensive model of the S-N curves with a capability of considering the increased scatter in the transition between the high-cycle and very-high-cycle domains has not been presented in the literature yet. A further innovation was to combine this model with the neural network in order to model the relationship between the parameters of the S-N curve and the applied manufacturing technology. The theory is explained in detail in section 1, experimental data are presented in section 2 and the results are presented and discussed in section 3.

1 THEORETICAL BACKGROUND

1.1 Variable-Scatter Model for the S-N Curve

To model the S-N curves and their scatter for a 51CrV4 spring steel a similar statistical model as used in [16] was applied. Following this approach, the scatter of the number of load-cycles-to-failure N for an arbitrary amplitude-stress level S_a was described using a two-parametric Weibull's PDF, see Eq. (2) in section 1. The trend of the S-N curve in the neighbourhood of the knee-point was linked directly to the Weibull's scale parameter η:

$$S_a = a \cdot \eta(S_a)^{-b} + c \cdot \eta(S_a)^{-(b+d)}; \quad a,b,c,d > 0, \tag{3}$$

with the Weibull's shape parameter β that is now dependent on the loading level S_a:

$$\beta = \beta(S_a) = f \cdot \left[1 + \frac{g}{1+\exp\left[-h \cdot (S_a - S_{KP})\right]}\right], \quad f \geq 1; \quad g,h,S_{KP} > 0. \tag{4}$$

With this equation the shape parameter β changes continuously and smoothly from the value of f at very low amplitude-stress levels to the value of $(f \cdot g)$ at high amplitude-stress levels. The transition gradient between the two limit values depends on the parameter h, with the steepest gradient occurring at the amplitude-stress value S_{KP}. When combined with the scale parameter η from Eq. (3) a small scatter is obtained at high amplitude-stress levels and an increased scatter is obtained at the lower amplitude-stress levels that correspond to the very-high-cycle fatigue domain.

To avoid illogical shape of the durability curves around the knee point $S_a = S_{KP}$ two limit conditions are defined:

1. The parameter g should never exceed the following value of g_{lim}:

$$g \leq g_{\lim} = \max\left\{3, \frac{b+d}{5 \cdot b} - 1\right\}. \tag{5}$$

2. The parameter h should never exceed the following value of h_{lim}:

$$h \leq h_{\lim} = \frac{2 \cdot \min\left\{4, \frac{b+d}{5 \cdot b}\right\}}{S_{KP} \cdot f \cdot g}. \tag{6}$$

The two conditions in Eqs. (5) and (6) limit the transition gradient between the small and large values of the shape parameter β relative to the trend-curve slope ratio $(b+d)/b$. The knee-point stress S_{KP} is calculated as a cross-section of the two asymptotes of Eq. (3), see Fig. 2:

$$S_{KP} = a \cdot \eta_{KP}^{b}, \tag{7}$$

$$\eta_{KP} = \exp\left[\frac{\ln(a) - \ln(c)}{-d}\right]. \tag{8}$$

In this way the S-N curve and its scatter in the neighbourhood of the knee point between the high-cycle and very-high-cycle fatigue domains is modelled with seven parameters: a, b, c, d, f, g and h. These parameters can be estimated using a numerical optimisation process.

1.2 Serial Hybrid Multilayer Perceptron

Since the material characteristics of the spring steel are dependent on the manufacturing technology and the heat treatment, they are also reflected in the trend and scatter of the corresponding S-N curve. This means that the parameters, a, b, c, d, f, g and h from subsection 1.1 are not constant, but they differ according to the applied production process. To model this relationship, the serial hybrid multilayer perceptron (SHMP) neural network according to Agarwal [19] was applied.

The multilayer perceptron (MP) is linked in series with the analytical model of the S-N curve and its scatter from Eqs. (3) and (4), see also Fig. 3 ([20] and [21]). This means that the MP is applied first for modelling the dependence of the parameters a, b, c, d, f, g and h on the manufacturing technology and the heat treatment. Then the analytical model is used only for modelling the S-N curve and its scatter after the seven parameters are predicted by the MP.

The result of each fatigue-life test was the number-of-cycles-to-failure N_l for the given amplitude-stress level $S_{a;l}$, the manufacturing technology and the heat treatment. Therefore the data points for training and/or testing the SHMP have the following form: $\{(\mathbf{x}_l, S_{a;l}, N_l) l = 1, ..., n\}$. The vector of the input independent variables $\mathbf{x}$ represents the

parameters of the applied production process. The l^{th} amplitude-stress level $S_{a;l}$ is the independent variable of the analytical model from subsection 1.1 and Fig. 3. The l^{th} number-of-cycles-to-failure N_l is the SHMP's dependent variable and n is the total number of sample points. Having this in mind, Eqs. (2) to (4) are changed as follows:

$$N = N(\mathbf{x}, S_a) \rightarrow f\left(N|\eta,\beta\right) = \frac{\beta}{\eta}\cdot\left(\frac{N}{\eta}\right)^{\beta-1}\cdot \cdot\exp\left[-\left(\frac{N}{\eta}\right)^{\beta}\right], \quad (2)$$

$$\eta = \eta(\mathbf{x}, S_a) \rightarrow S_a = a(\mathbf{x})\cdot\eta(\mathbf{x}, S_a)^{-b(\mathbf{x})} + + c(\mathbf{x})\cdot\eta(\mathbf{x}, S_a)^{-(b(\mathbf{x})+d(\mathbf{x}))}, \quad (9)$$

$$\beta = \beta(\mathbf{x}, S_a) = = f(\mathbf{x})\cdot\left[1+\frac{g(\mathbf{x})}{1+\exp\left[-h(\mathbf{x})\cdot(S_a - S_{KP}(\mathbf{x}))\right]}\right]. \quad (10)$$

The output of neuron z_j is equal to the weighted sum of M_i outputs z_i from the preceding layer, modified by an activation function φ_j:

$$z_j = \varphi_j\left(\sum_{i=1}^{M_i} w_{ij}\cdot z_i + \Theta_j\right), \quad (11)$$

where w_{ij} are the synaptic weights and Θ_j is the threshold of the neuron. In our case the activation function was a tanh() function for the hidden neurons and a linear function for the output neurons. This activation function was used instead of the more commonly used sigmoid function, because it turned out that a convergence of a training process was much better with the tanh() than with the sigmoid function in the studied case. The inputs x_i to the MP model were the components of the condition vector $\mathbf{x}$. The output neurons z_k are applied for calculating the parameters a, b, c, d, f, g and h. The relations between these parameters and the neural outputs z_k must fulfill the restraints from Eqs. (3) and (4) and ensure the robustness of the model:

$$a = a(\mathbf{x}) = 10000\cdot\frac{\exp(z_k^a)}{1+\exp(z_k^a)},$$

$$b = b(\mathbf{x}) = 0.01+0.99\cdot\frac{\exp(z_k^b)}{1+\exp(z_k^b)},$$

$$c = c(\mathbf{x}) = 10^7\cdot\frac{\exp(z_k^c)}{1+\exp(z_k^c)},$$

$$d = d(\mathbf{x}) = 0.01+0.99\cdot\frac{\exp(z_k^d)}{1+\exp(z_k^d)},$$

$$f = f(\mathbf{x}) = 1+4\cdot\frac{\exp(z_k^f)}{1+\exp(z_k^f)},$$

$$g = g(\mathbf{x}) = 3\cdot\frac{\exp(z_k^g)}{1+\exp(z_k^g)},$$

$$h = h(\mathbf{x}) = 0.1\cdot\frac{\exp(z_k^h)}{1+\exp(z_k^h)}. \quad (12)$$

These restraints were extensively tested in a preliminary study involving two different spring steels, a cold-drawn structural steel and two complex-phase steels.

The cost function for the SHMP model was a maximum-likelihood function E_{ML} according to

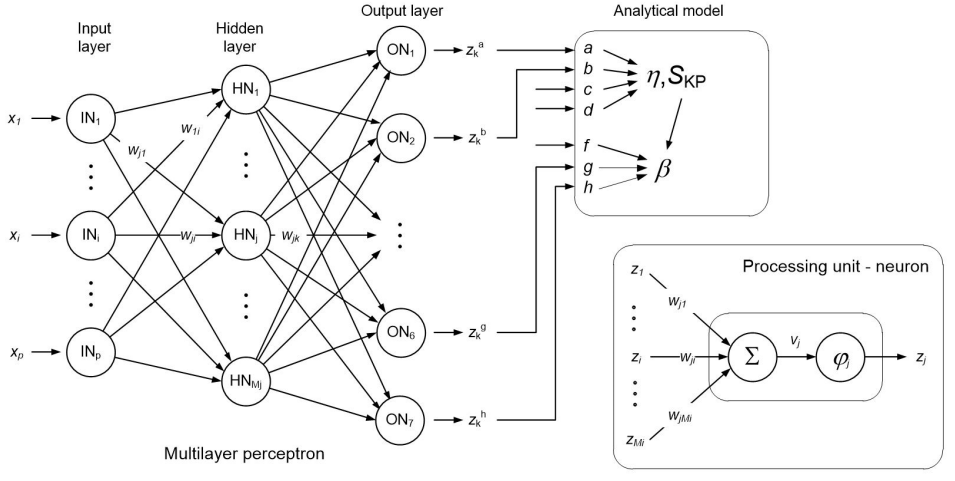

Fig. 3. *Topology of the applied serial hybrid multilayer perceptron*

$$E_{ML} = -\ln(ML) = -\ln\left(\prod_{l=1}^{n}\left[f(N_l \mid \eta_{pred,l}, \beta_{pred,l})\right]^{\delta_l} \cdot \left[1 - F(N_l \mid \eta_{pred,l}, \beta_{pred,l})\right]^{1-\delta_l}\right),$$

$$E_{ML} = \sum_{l=1}^{n} e_{ML}(l) = \sum_{l=1}^{n} -\left\{\delta_l \cdot \ln\left[f(N_l \mid \eta_{pred,l}, \beta_{pred,l})\right] + (1-\delta_l) \cdot \ln\left[1 - F(N_l \mid \eta_{pred,l}, \beta_{pred,l})\right]\right\} =$$

$$= \sum_{l=1}^{n} -\left(\delta_l \cdot \ln\left[\frac{\beta_{pred,l}}{\eta_{pred,l}} \cdot \left(\frac{N_l}{\eta_{pred,l}}\right)^{\beta_{pred,l}-1} \cdot \exp\left(-\left(\frac{N_l}{\eta_{pred,l}}\right)^{\beta_{pred,l}}\right)\right] + (1-\delta_l) \cdot \ln\left[\exp\left(-\left(\frac{N_l}{\eta_{pred,l}}\right)^{\beta_{pred,l}}\right)\right]\right). \quad (13)$$

Pascual and Meeker [22]. Using this cost function the failed specimens as well as run-outs are considered for estimating the S-N curve and its scatter. For the fatigue failure a fatigue-failure identifier δ_l is set to 1 and for the run-outs it is set to 0 in the E_{ML} cost function, see Eq. (13).

To calculate the error $e_{ML}(l)$ for each sample l, the parameters a, b, c, d, f, g and h are predicted first by the MP for the input vector $\mathbf{x}_i$. From these parameters and the value of $S_{a;l}$ the Weibull's scale parameter $\eta_{pred;l}$ is calculated with Eq. (9) using the Newton-Raphson method. The shape parameter $\beta_{pred;l}$ is calculated with Eq. (10).

The training of the SHMP model was carried out numerically with an error back-propagation algorithm and an epoch-based training. The gradients of the cost function E_{ML} for the synaptic weights w_{ij} were calculated as the sum of the gradients of the individual samples: $\partial E_{ML} / \partial w_{ij} = \sum_{l=1}^{n} \partial e_{ML}(l) / \partial w_{ij}$. In every iteration of the training process the synaptic weights were adapted as follows [23]:

$$\Delta w_{ij}(t) = -\theta_{ij}(t+1) \cdot \left.\frac{\partial E_{ML}}{\partial w_{ij}}\right|_{(t)} + \alpha \cdot \Delta w_{ij}(t-1). \quad (14)$$

The training process proceeds until the modelled S-N curves with their scatter agree with the experimental results for the different vectors $\mathbf{x}_i$. The training-rate parameter θ_{ij} in Eq. (15) was added to consider the past gradient changes according to the delta-bar-delta rule [21].

The sample gradients $\partial e_{ML}(l) / \partial w_{ij}$ were calculated as follows ([21] and [22]):

$$\partial e_{ML}(l) / \partial w_{ij} = \Delta_j \cdot z_i, \quad (15)$$

where Δ_j is the error of the neuron j in the next layer to which the neuron i sends its signal. The next layer of neurons is either a hidden or an output layer. To calculate the errors Δ_j in the output layer of the MP the partial derivatives $\partial e_{ML}(l) / \partial z_k$ for the output neurons z_k must be calculated for each sample $(\mathbf{x}_l, S_{a;l}, N_l, \delta_l)$:

$$\frac{\partial e_{ML}(l)}{\partial z_k^{par}} = \left\{\frac{\partial e_{ML}(l)}{\partial \eta_{pred,l}} \cdot \frac{\partial \eta_{pred,l}}{\partial par} + \frac{\partial e_{ML}(l)}{\partial \beta_{pred,l}} \cdot \frac{\partial \beta_{pred,l}}{\partial S_{KP}} \cdot \frac{\partial S_{KP}}{\partial par}\right\} \cdot \frac{\partial par}{\partial z_k^a} \; ; \quad par = a,b,c,d,$$

$$\frac{\partial e_{ML}(l)}{\partial z_k^{par}} = \frac{\partial e_{ML}(l)}{\partial \beta_{pred,l}} \cdot \frac{\partial \beta_{pred,l}}{\partial par} \cdot \frac{\partial par}{\partial z_k^h} \; ; \; par = f,g,h. \quad (16)$$

For reasons of clarity, the marking of the dependence on the vector $\mathbf{x}$ is omitted in Eq. (16) and the corresponding partial derivatives are listed in the appendix.

1.3 Selecting the Optimal SHMP Model

The SHMP model should represent the experimental data $\{(\mathbf{x}_l, S_{a;l}, N_l, \delta_l); l = 1, ..., n\}$ in the best possible way, but if the SHMP topology is too complex a data over-fit can occur. So the complexity should sometimes be sacrificed to avoid the over-fitting of the SHMP model. In our study we decided to choose the optimal topology of the SHMP model using the Akaike information criterion (AIC) [23]:

$$AIC = 2 \cdot n_w + 2 \cdot \ln(E_{ML}), \quad (17)$$

where n_w is the number of synaptic weights in the MP and E_{ML} is the final value of the cost function. The smaller the value of the AIC criterion, the better the SHMP topology. In addition to the original form of the AIC criterion, we also applied its modification with a second-order correction for small samples [24]:

$$AIC_{c,BA} = AIC + \frac{2 \cdot n_w \cdot (n_{w+1})}{n - n_w - 1}. \quad (18)$$

2 EXPERIMENTAL DATA

Cylindrical specimens according to the ASTM E 606-92 standard [25] were prepared by Institute of Metals

and Technology. They were cut from 51CrV4 steel bars in the rolling direction and manufactured by turning. In the middle the specimens were polished to an average roughness R_a of 0.2 μm, see Fig. 4. The steel bars were produced by two manufacturing routes. The reference series was prepared by a conventional manufacturing technology, i.e. continuous casting and hot rolling. The alternative series was first continuously cast, then electro-slag remelted (ESR) in order to obtain more uniform microstructure and finally hot rolled.

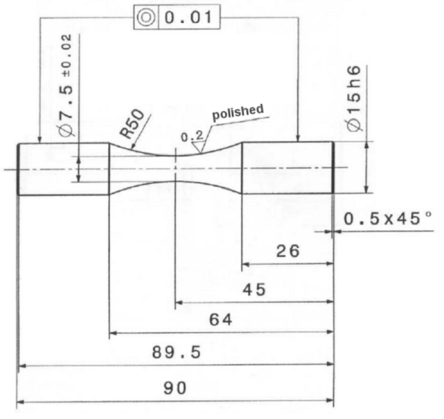

Fig. 4. *Cylindrical specimen used for the fatigue experiments*

Cylindrical test specimens from both series were subjected to two different heat treatment procedures. The first heat treatment of the specimens consisted of heating to 870 °C, soaking for 10 minutes, which was followed by quenching in N_2 gas at 5 bar and a fast cooling rate of 7.5 °C/s until 60 °C. The second heat treatment of the specimens was performed at the same austenitizing temperature of 870 °C but a slower cooling rate of 2.7 °C/s was obtained by reducing N_2 gas pressure to 1.05 bar. In both cases the specimens were finally tempered at 475 °C for 1 h.

Therefore four different groups of specimens were obtained: two different manufacturing technology routes combined with two different heat treatments. Altogether 101 specimens were manufactured with at least 23 specimens in each group [26].

The fatigue-life experiments were carried out at the universal dynamic servo-hydraulic test stand Instron 8802. A Dynacell load sensor was used for force measurements and the experiments were load-controlled. The axial loading of the cylindrical specimens was fully reversed (R = –1). The experiments were carried out at a room temperature of 21 °C at different amplitude-stress levels (500 MPa to 780 MPa) until the fatigue failure occurred. The testing frequency was 30 Hz. If the number of loading cycles exceeded 1 million without the fatigue failure the experiment run was terminated in order to reduce the experimental time and cost, since it follows from the literature that the fatigue failure between 1 million and 2 millions of loading cycles is highly unlikely for these kind of high-strength steels [12]. The experimental results are presented in Fig. 5.

3 RESULTS AND DISCUSSION

3.1 Defining the SHMP Topologies and Pre-Processing the Data

There are two independent parameters that represent the input for the SHMP (a binary variable indicating

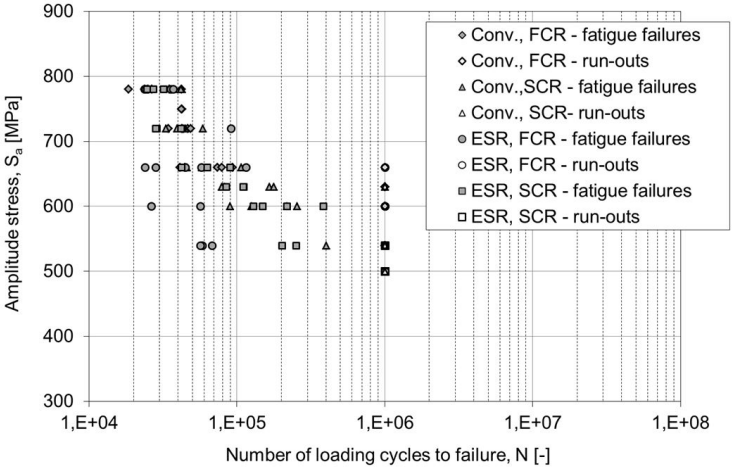

Fig. 5. *Experimental fatigue-life data for 51CrV4 steel (abbreviations: conv.=conventional manufacturing technology, ESR=electro-slag remelting, FCR= fast cooling rate, SCR=slow cooling rate)*

the manufacturing technology and a real-valued variable indicating the cooling rate after the warming-up phase), so the number of neurons in the SHMP input layer was two. The seven parameters a, b, c, d, f, g and h were predicted by the SHMP. Therefore, there were seven neurons in the output layer of the SHMP. All the SHMPs had one hidden layer and four different topologies consisting of 2 (NN_1), 3 (NN_2), 6 (NN_3) or 9 (NN_4) neurons in the hidden layer.

The training set was composed of all the n = 101 samples in Fig. 5. Many training processes were carried out with different initial values of the synaptic weights and training-rate parameters. A number of iterations were limited to 2,000,000 for each training process. The details on the training processes are listed in Table 1 for the best achieved cost functions. Variations of the cost-functions E_{ML} during these training processes are presented in Fig. 6.

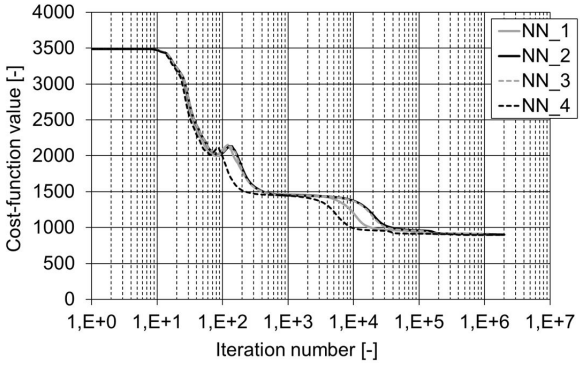

Fig. 6. *A cost-function history during the training process*

3.2 Prediction Results

We can see from Table 1 that the NN_4 topology with the largest number of neurons in the hidden layer resulted in the lowest value of the E_{ML} cost function that was achieved before 1 million of training iterations with no further reduction in the cost-function, see Fig. 6.

However, this result is misleading, because the NN_4 topology had almost as much synaptic weights as there was the number of training samples. That is why this topology may be improper, since it is prone to data over-fitting.

From the viewpoint of the AIC and $AIC_{c,BA}$ criteria, the best topology was NN_1, with two neurons in the hidden layer. The good score in the two AIC criteria was only due to its small number of synaptic weights, because its cost function was the highest. This implies that its fit of the S-N curves to the experimental data is not the best – see Figs. 7 and 8 for a comparison of the modelled S-N curves.

To assess the prediction quality of the SHMP models the S-N curves with their scatter were additionally estimated on a case-by-case basis. The seven parameters a, b, c, d, f, g and h for each of the four S-N curves were estimated using the real-valued genetic algorithm (**[27]** and **[28]**). The S-N curves, which were estimated using the genetic algorithm, are presented with a black color in Figs. 7 and 8.

It can be concluded from Table 1 and Figs. 7 and 8 that the best fit to the fatigue-life data is achieved with the NN_3 and NN_4 topologies. This

Table 1. *Summary of the applied SHMP topologies and their training processes*

SHMP topology		NN_1	NN_2	NN_3	NN_4
Basic data about the SHMP topologies and their training processes	No. of input neurons	2	2	2	2
	No. of output neurons	7	7	7	7
	Act. function of output neurons	linear	linear	linear	linear
	No. of hidden layers and neurons	1 layer, 2 neurons	1 layer, 3 neurons	1 layer, 6 neurons	1 layer, 9 neurons
	Act. function of hidden neurons	tanh()	tanh()	tanh()	tanh()
	Initial value of the parameter η	10^{-8}	10^{-8}	10^{-8}	10^{-8}
	Value of the parameter α	10^{-2}	10^{-2}	10^{-2}	10^{-2}
	Initial (final) value of the param. κ	5×10^{-12}	10^{-11}	10^{-11}	5×10^{-12}
	Initial (final) value of the param. γ	0.995	0.99	0.99	0.995
	Value of the parameter ξ	0.7	0.7	0.7	0.7
	No. of train. Samples per epoch	101	101	101	101
	Iteration no. for the minimum CF	2000000	2000000	2000000	786200
Cost function values and the AIC criteria values for the trained SHMP	Smallest value of the CF E_{ML}	901.53	901.39	897.41	896.71
	Number of synaptic weights n_w	27	37	67	97
	AIC criterion	955.5311	975.3921	1031.407	1090.708
	$AIC_{c,BA}$ criterion	976.2434	1020.027	1307.528	7428.041

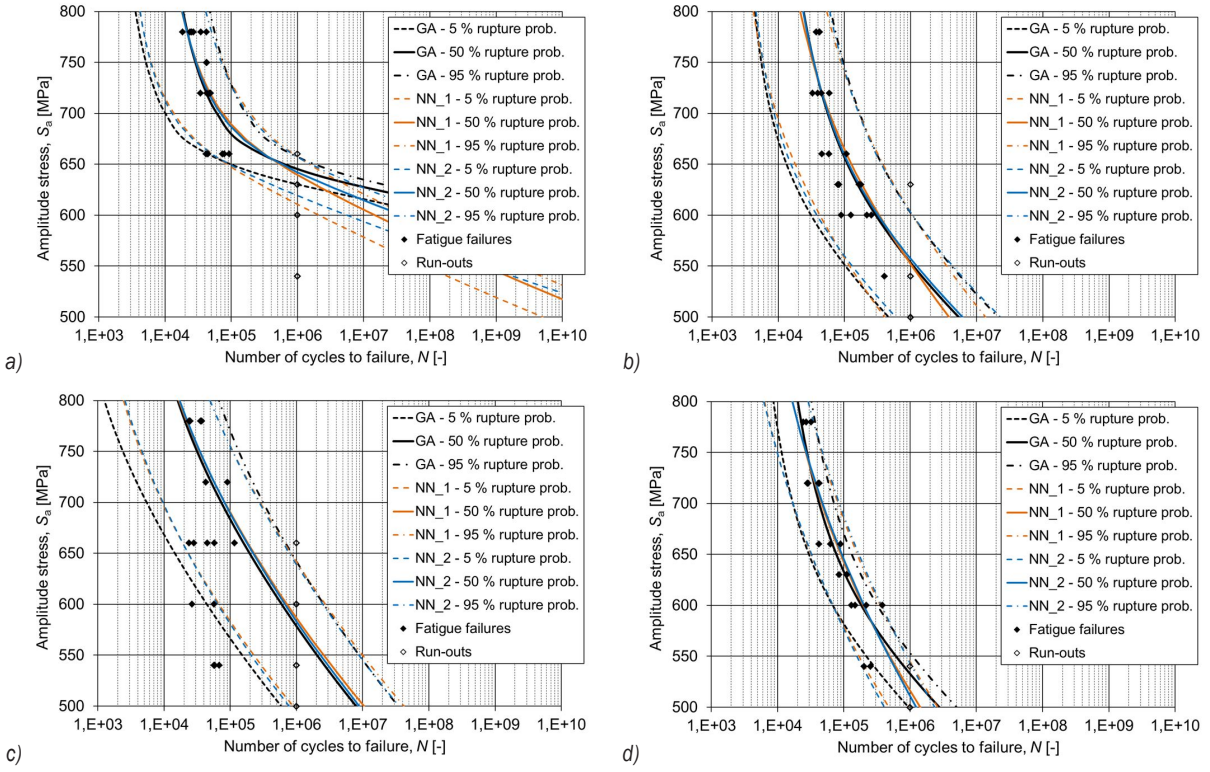

Fig. 7. *Modelled S-N curves for the SHMP topologies NN_1 and NN_2; a) Conv., FCR, b) Conv., SCR, c) ESR, FCR, d) ESR, FCR*

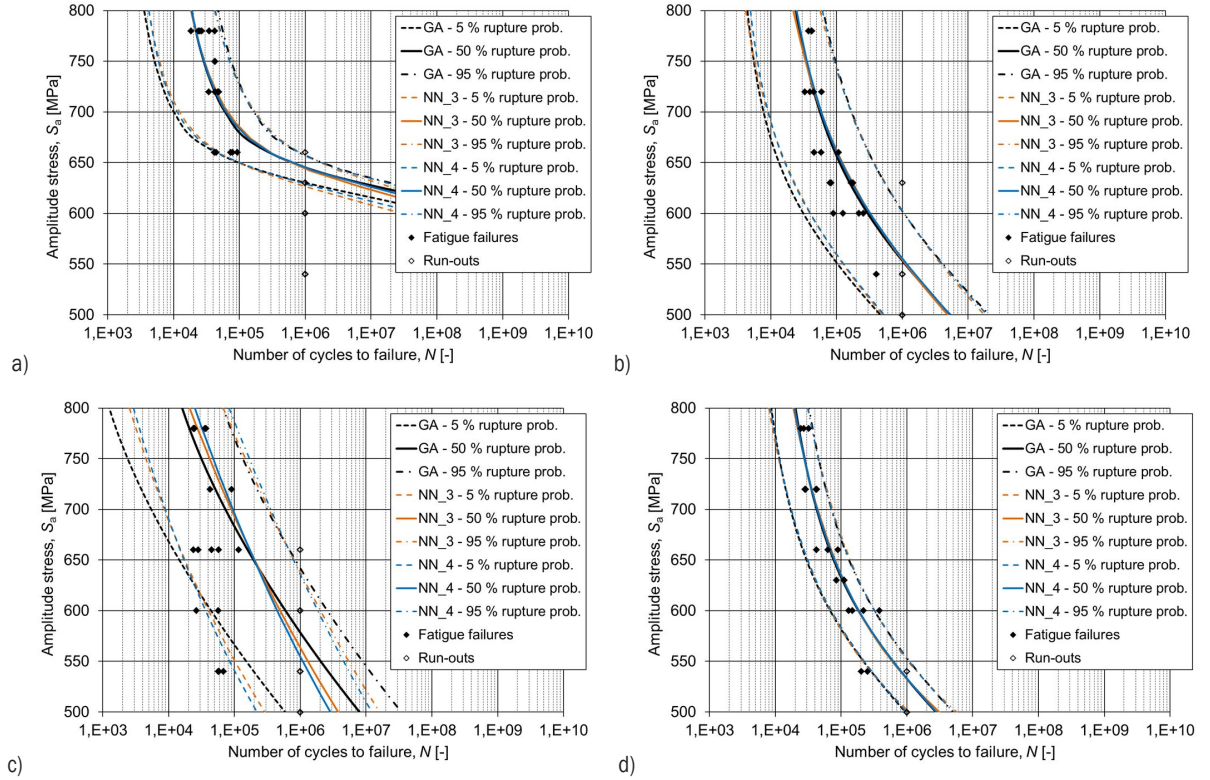

Fig. 8. *Modelled S-N curves for the SHMP topologies NN_3 and NN_4; a) Conv., FCR, b) Conv., SCR, c) ESR, FCR, d) ESR, SCR*

means that the most appropriate topology was NN_3 with less neurons in the hidden layer, because the discrepancy in the cost functions for the topologies is almost insignificant. Due to the relatively small number of training data the NN_3 topology has better generalisation ability and is less prone to the data-overfitting. Besides, it resulted in the lower values of the two *AIC* and criteria when compared to the NN_4 topology.

By comparing the S-N curves modelled with the SHMP and the genetic algorithm, it can be concluded that the modelled S-N curves do not differ a lot for the NN_3 and NN_4 topologies. This means that the SHMP topologies NN_3 and NN_4 were successfully applied for modelling the fatigue-life data of the 51CrV4 steel. The only exception is the S-N curve model for the data set that corresponds to the ESR manufacturing combined with the fast cooling rate during quenching. In this case the transition zone between the high-cycle- and very-high-cycle-fatigue domains is very broad in both directions (S_a and N). This is very difficult to model with a SHMP, given the fact that the same transition zone is much narrower for the other three data sets. For this reason it was extremely difficult to build a good S-N curve model, even if we try to do it individually with the genetic algorithm.

From the presented results it can be concluded that the introduced SHMP model is capable of modelling the S-N curve and its scatter well, also in the neighbourhood of a knee point between the high-cycle- and very-high-cycle-fatigue domains. Of course, since there is always a problem with a relatively small number of experimental fatigue-life data one should always try to find the simplest possible SHMP model that still enables fairly good predictions of the S-N curves and their scatter. The applied SMHP is general, which means that it can be applied for modelling the S-N curves and their scatter for arbitrary (metallic) materials, if the appropriate experimental data are available and the fatigue-life data-sets have approximately equal size for different manufacturing technologies.

4 CONCLUSION

In this article a procedure is presented for predicting the S-N curves and their scatter for 51CrV4 spring steel on the basis of experimental fatigue-life data that was obtained for different manufacturing technologies and heat treatments. The procedure is based on the application of a multilayer perceptron neural network, into which an analytical shape of the bi-linear S-N log-log curve was incorporated with the Weibull PDF describing its scatter. The results presented in the article were obtained for four combinations of the manufacturing technologies and quenching cooling rates. Different SHMP topologies were applied and each of them was trained with 101 experimentally obtained samples.

The results presented in the article show that it is possible to simultaneously estimate the parameters of the S-N curves and their scatter on the basis of the experimental data for different combinations of manufacturing technologies and heat treatments. The selection of a suitable SHMP topology should be made very carefully. It is almost always possible to obtain a good fit to the training data, if complex SHMP topologies with large numbers of neurons in the hidden layer are applied. On the other hand, such topologies can over-fit the data, especially if the number of synaptic weights in the SHMP model is comparable or larger than the number of data points in the training set. For this reason two variations of the AIC were applied in the research to select the proper SHMP topology. It turned out that the AIC criterion alone was not enough to estimate the most appropriate SHMP topology. So, when choosing the optimal SHMP model, one should make a trade-off between the simplicity of the SHMP model and its ability to generalise (but not over-fit) the experimental data. A general rule-of-thumb would be that there should be at least a few times more data points in the training set than there are synaptic weights in the SHMP model.

5 ACKNOWLEDGEMENT

The authors acknowledge the financial support from the Slovenian Research Agency (ARRS) for supporting the research programme P2-0182 R&D evaluations.

6 REFERENCES

[1] Nagode, M., Klemenc, J., Fajdiga, M. (2001). Parametric modelling and scatter prediction of rainflow matrices. *International Journal of Fatigue*, vol. 23, no. 6, p. 525-532, **DOI:10.1016/S0142-1123(01)00007-X**.

[2] Tovo, R. (2001). On the fatigue reliability evaluation of structural components under service loading. *International Journal of Fatigue*, vol. 23, no. 7, p. 587-598, **DOI:10.1016/S0142-1123(01)00021-4**.

[3] Zhao, Y.X., Yang, B., Zhai, Z.Y. (2008). The framework for a strain-based fatigue reliability analysis. *International Journal of Fatigue*, vol. 30, no. 3, p. 493-501, **DOI:10.1016/j.ijfatigue.2007.04.006**.

[4] O'Connor, P., Kleyner, A. (2012). *Practical Reliability Engineering, 5th ed*. John Willey & Sons, New York.

[5] Xiao, Z., Zhao, Q.Y., Lin, F., Zhu, M.M., Deng, J.Y. (2018). Studying the fatigue life of a non-pneumatic wheel by using finite-life design for life prediction. *Strojniški vestnik - Journal of Mechanical Engineering*, vol. 64, no. 1, p. 56-67, **DOI:10.5545/sv-jme.2017.4695**.

[6] Moral Portalés R., Bochons Sania M.d.M., Klemenc, J. (2018). Theoretical framework for estimating a product's reliability using a variable-amplitude loading spectrum and a stress-based approach. *Fatigue and Fracture of Engineering Materials and Structures*, vol. 41, no. 8, p. 1662-1673, **DOI:10.1111/ffe.12804**.

[7] Gróza, M., Váradi, K. (2018). Fatigue design of ferritic-pearlitic nodular cast iron components with surface discontinuities. *Strojniški vestnik - Journal of Mechanical Engineering*, vol. 64, no. 6, p. 373-382, **DOI:10.5545/sv-jme.2017.5120**.

[8] Buxbaum, O. (1986). *Betriebsfestigkeit*. Verlag Stahleisen, Düsseldorf.

[9] EUROCODE 3 (2005). *Design of Steel Structures – Part 1-9: Fatigue*. European committee for standardization, Brussels.

[10] Bathias, C. (1999). There is no infinite fatigue life in metallic materials. *Fatigue & Fracture of Engineering Materials & Structures*, vol. 22, no. 7, p. 559-565, **DOI:10.1046/j.1460-2695.1999.00183.x**.

[11] Haibach, E. (2006). *Betriebsfestigkeit, Verfahren und Daten zur Bauteilberechnung. 3. Auflage*. Springer-Verlag, Berlin Heidelberg.

[12] Toplack, G., Eichlseder, W., Godor, I., Leitner, H. (2003). Influence of size and type of loading on S/N-Curve. *ESIS - Cumulative Fatigue Damage Conference Proceedings*, p. 187-191.

[13] Schaumann, P., Steppler, S. (2013). Fatigue tests of axially loaded butt welds up to very high cycles. *Procedia Engineering*, vol. 66, p. 88-97, **DOI:10.1016/j.proeng.2013.12.065**.

[14] Wagener, R., Hensel, J. (2014). Einflussgrößen auf die Lage des Abknickpunktes der Wöhlerlinie für den Schwingfestigkeitsnachweis von Schweiß verbindungen (IGF 16602N), from *https://www.dvsev.de/fv/neu/indexcfm?Navigation=Forschungsergebnisse&PID=783&CFID=70346917&CFTOKEN=97080438*, accessed on 2018-26-10. Result score too low

[15] Dowling, N.E. (2012). *Mechanical Behaviour of Materials, 4th ed.* Pearson Education, Upper Saddle River.

[16] Klemenc, J., Fajdiga, M. (2013). Joint estimation of E-N curves and their scatter using evolutionary algorithms. *International Journal of Fatigue*, vol. 56, p. 42-53, **DOI:10.1016/j.ijfatigue.2013.08.005**.

[17] Bučar, T., Nagode, M., Fajdiga, M. (2006). A neural network approach to describing the scatter of S-N curves. *International Journal of Fatigue*, vol. 28, no. 4, p. 311-323, **DOI:10.1016/j.ijfatigue.2005.08.002**.

[18] Klemenc, J., Janezic, M., Fajdiga, M. (2012). Modelling the scatter of E-N curves using a serial hybrid neural network. *Neural Computing and Applications*, vol. 21, no. 7, p. 1517-1530, **DOI:10.1007/s00521-012-0828-2**.

[19] Agarwal, M. (1997). Combining neural and conventional paradigms for modelling, prediction and control. *International Journal of System Science*, vol. 28, no. 1, p. 65-81.

[20] Bishop, C.M. (2005). *Neural Networks for Pattern Recognition*. Clarendon Press, Oxford.

[21] Haykin, S. (2009). *Neural Networks and Learning Machines*. Pearson education, New York.

[22] Pascual, F.G., Meeker, W.Q. (1999). Estimating fatigue curves with the random fatigue-limit model. *Technometrics*, vol. 41, no. 4, p. 277-290, **DOI:10.2307/1271342**.

[23] Akaike, H. (1974). A new look at the statistical model identification. *IEEE Transactions on Automatic Control*, vol. 19, no. 6, p. 716-723, **DOI:10.1109/TAC.1974.1100705**.

[24] Burnham, K.P., Anderson, D.R. (2002). Model Selection and Multimodel Inference: A Practical Information-Theoretic Approach, 2nd edition. Springer Verlag.

[25] ASTM E606-92(2004)e1: Standard Practice for Strain-Controlled Fatigue Testing. *ASTM International*, West Conshohocken, **DOI:10.1520/E0606-92R04E01**.

[26] Podgornik, B., Leskovšek, V., Godec, M., Senčič, B. (2014). Microstructure refinement and its effect on properties of spring steel. *Materials Science & Engineering: A, Structural Materials: Properties, Microstructure and Processing*, vol. 599, p. 81-86, **DOI:10.1016/j.msea.2014.01.054**.

[27] Temby, L., Vamplew, P., Berry A. (2005). Accelerating real-valued genetic algorithms using mutation-with-momentum. *The 18th Australian Joint Conference on Artificial Intelligence*, vol 3809, Springer, Berlin, Heidelberg, **DOI:10.1007/11589990_149e**.

[28] Klemenc, J. (2015). Influence of fatigue–life data modelling on the estimated reliability of a structure subjected to a constant-amplitude loading. *Reliability Engineering and System Safety*, vol. 142, p. 238-247, **DOI:10.1016/j.ress.2015.05.026**.

7 APPENDIX

$$\frac{\partial e_{ML}(l)}{\partial \eta_{pred,l}} = -\left\{ \delta_l \cdot \frac{\beta_{pred,l}}{\eta_{pred,l}} \cdot \left[\left(\frac{N_l}{\eta_{pred,l}} \right)^{\beta_{pred,l}} - 1 \right] + (1-\delta_l) \cdot \frac{\beta_{pred,l}}{\eta_{pred,l}} \cdot \left(\frac{N_l}{\eta_{pred,l}} \right)^{\beta_{pred,l}} \right\}, \tag{A.1}$$

$$\frac{\partial e_{ML}(l)}{\partial \beta_{pred,l}} = -\left\{ \delta_l \cdot \left[\frac{1}{\beta_{pred,l}} + \ln\left(\frac{N_l}{\eta_{pred,l}} \right) \cdot \left(1 - \left(\frac{N_l}{\eta_{pred,l}} \right)^{\beta_{pred,l}} \right) \right] - (1-\delta_l) \cdot \ln\left(\frac{N_l}{\eta_{pred,l}} \right) \cdot \left(\frac{N_l}{\eta_{pred,l}} \right)^{\beta_{pred,l}} \right\}, \tag{A.2}$$

$$\frac{\partial \beta_{pred,l}}{\partial S_{KP}} = -f \cdot g \cdot h \cdot \frac{\exp\left[h \cdot (S_{a,l} - S_{KP})\right]}{\left\{1 + \exp\left[h \cdot (S_{a,l} - S_{KP})\right]\right\}^2}, \quad \text{(A.3)}$$

$$\frac{\partial \eta_{pred,l}}{\partial a} = \frac{1}{a \cdot b \cdot \eta_{pred,l}^{-1} + c \cdot (b+d) \cdot \eta_{pred,l}^{-d-1}}, \quad \text{(A.4)}$$

$$\frac{\partial S_{KP}}{\partial a} = S_{KP} \cdot \frac{\partial \ln(S_{KP})}{\partial a} = S_{KP} \cdot \left[\frac{1}{a} \cdot \left(1 + \frac{b}{d}\right)\right], \quad \text{(A.5)}$$

$$\frac{\partial a}{\partial z_k^a} = \frac{a}{1 + \exp(z_k^a)}, \quad \text{(A.6)}$$

$$\frac{\partial \eta_{pred,l}}{\partial b} = \frac{-S_{a,l} \cdot \ln(\eta_{pred,l})}{a \cdot b \cdot \eta_{pred,l}^{-b-1} + c \cdot (b+d) \cdot \eta_{pred,l}^{-b-d-1}}, \quad \text{(A.7)}$$

$$\frac{\partial S_{KP}}{\partial b} = S_{KP} \cdot \frac{\partial \ln(S_{KP})}{\partial b} = S_{KP} \cdot \frac{\ln(a) - \ln(c)}{d}, \quad \text{(A.8)}$$

$$\frac{\partial b}{\partial z_k^b} = \frac{b - 0.01}{1 + \exp(z_k^b)}, \quad \text{(A.9)}$$

$$\frac{\partial \eta_{pred,l}}{\partial c} = \frac{1}{a \cdot b \cdot \eta_{pred,l}^{d-1} + c \cdot (b+d) \cdot \eta_{pred,l}^{-1}}, \quad \text{(A.10)}$$

$$\frac{\partial S_{KP}}{\partial c} = S_{KP} \cdot \frac{\partial \ln(S_{KP})}{\partial c} = S_{KP} \cdot \left[\frac{-b}{c \cdot d}\right], \quad \text{(A.11)}$$

$$\frac{\partial c}{\partial z_k^c} = \frac{c}{1 + \exp(z_k^c)}, \quad \text{(A.12)}$$

$$\frac{\partial \eta_{pred,l}}{\partial d} = \frac{-c \cdot \ln(\eta_{pred,l})}{a \cdot b \cdot \eta_{pred,l}^{d-1} + c \cdot (b+d) \cdot \eta_{pred,l}^{-1}}, \quad \text{(A.13)}$$

$$\frac{\partial S_{KP}}{\partial d} = S_{KP} \cdot \frac{\partial \ln(S_{KP})}{\partial d} = S_{KP} \cdot \left(\frac{-b}{d^2}\right) \cdot \left[\ln(a) - \ln(c)\right], \quad \text{(A.14)}$$

$$\frac{\partial d}{\partial z_k^d} = \frac{d - 0.01}{1 + \exp(z_k^d)}, \quad \text{(A.15)}$$

$$\frac{\partial \beta_{pred,l}}{\partial f} = 1 + \frac{g}{1 + \exp\left[-h \cdot (S_{a,l} - S_{KP})\right]}, \quad \text{(A.16)}$$

$$\frac{\partial f}{\partial z_k^f} = \frac{f - 1}{1 + \exp(z_k^f)}, \quad \text{(A.17)}$$

$$\frac{\partial \beta_{pred,l}}{\partial g} = \frac{f}{1 + \exp\left[-h \cdot (S_{a,l} - S_{KP})\right]}, \quad \text{(A.18)}$$

$$\frac{\partial g}{\partial z_k^g} = \frac{g}{1 + \exp(z_k^g)}, \quad \text{(A.19)}$$

$$\frac{\partial \beta_{pred,l}}{\partial h} = f \cdot g \cdot (S_{a,l} - S_{KP}) \cdot \frac{\exp\left[h \cdot (S_{a,l} - S_{KP})\right]}{\left\{1 + \exp\left[h \cdot (S_{a,l} - S_{KP})\right]\right\}^2}, \quad \text{(A.20)}$$

$$\frac{\partial h}{\partial z_k^h} = \frac{h}{1 + \exp(z_k^h)}, \quad \text{(A.21)}$$

Strojniški vestnik - Journal of Mechanical Engineering 65(2019)5, 276-286
DOI:10.5545/sv-jme.2018.5922
Original Scientific Paper
Received for review: 2018-12-17
Received revised form: 2019-03-18
Accepted for publication: 2019-04-11

Study on the Effects of Hierarchical Wavy Morphology on Clearance Flow

Xi Zhang[1,*] – Tianlu Zhang[1] – Xiangyu Geng[1] – Jianfeng Hong[1] – Jinjun Wu[2]
[1]China University of Mining & Technology, School of Mechanical Electronic & Information Engineering, China
[2]China Academy of Machinery Science & Technology, China

This paper aims to explore the influences of multilevel sinusoidal structures on clearance flow by using numerical and experimental methods. A hierarchical sinusoidal morphology was proposed to design the gap between matching surfaces in water hydraulic systems. The specimens with the 0th order, the 1st order and the 2nd order sinusoidal structures were machined by a three dimensional (3D) printer, and their clearance leakage flow was tested on a water hydraulic annular clearance test rig. An extensive simulation study on the effects of waved surfaces with varying amplitudes and wavelengths on leakage was presented. Both the experimental and numerical results show that introducing hierarchical morphology on clearance surfaces will reduce leakage. Moreover, it was found that the leakage decreases with the increase of the ratio of the amplitude to wavelength. Further study of the flow field reveals that the leakage reduction of the 2nd order sinusoidal model is obtained due to the extra vortexes of various scales and the narrower width of the main flow and lower velocity. Moreover, our results indicate that the waved surface induces a micro-hydrodynamic effect that creates an additional load carrying capability, which is helpful for separating the matching surfaces to reduce wear. The study is beneficial to investigate the potential for improving efficiency through the optimization of gap design.

Keywords: hierarchical sinusoidal morphology, clearance flow, water, leakage

Highlights

- *A hierarchical sinusoidal morphology was proposed to design matching surfaces clearances.*
- *The effects of waved surfaces with different amplitudes and wavelengths on leakage were investigated.*
- *Hierarchical vortexes were found, load carrying ability and fluid erosion were discussed by analysing the pressure and velocity fields in the hierarchical sinusoidal models.*
- *Hierarchical morphology on matching surfaces not only can reduce leakage but also has advantages for reducing mechanical wear and fluid erosion, which is difficult by narrowing gaps.*

0 INTRODUCTION

Clearances broadly exist in hydraulic components, such as the matching clearances of piston/cylinder, swash plate/slipper pad and cylinder block/valve plate, etc., in which most of the energy is dissipated by friction and leakage [1]. With the increasing demand for an environmentally friendly, non-flammable, readily available and hygienic fluid medium in hydraulic systems, water used as a pressure medium has caused renewed interest. However, the kinematic viscosities of water and mineral oil are 1 m^2/s and 29 m^2/s at room temperature at atmospheric pressure, respectively. Lower viscosity is accompanied by poorer lubricity and larger leakage. For certain matching clearances, the leakage rate of water is larger than that of oil, which will cause more internal and external leakages for water hydraulic systems [2]. Therefore, smaller clearances have to be considered in order to achieve reduced leakage. However, narrower gaps in water hydraulic components will cause mechanical wear [1] and [3] and fluid erosion [4] due to the poor lubrication of water, which will enlarge gaps, leading to more leakage [5].

Surface topography technology has emerged in recent years as an effective method to reduce energy dissipation [6] to [8]. Recent works on various forms and shapes of surface texturing for high efficiency [9] and [10], energy-saving [11] and [12] and long performance life [13] and [14] have been carried out, which has already succeeded in many industrial applications [8], [15] and [16], such as seals [17] and [18], bearings [19] and [20] and gears [21] and [22]. An attempt to optimize piston topography to minimize energy dissipation within the piston cylinder interface was made by Wondergem and Ivantysynova [23] and Ivantysynova [24], who proposed a barrel-like piston. Ivantysynova and Lasaar [25] demonstrated the potential of an advanced gap design using computer simulation. The load carrying ability, piston friction force and gap flow were computed for all investigated surface variations, and then an improved barrel-like piston was proposed to reduce energy dissipation generated by piston/cylinder assembly. Kleist [26] also studied pistons with different shapes for radial piston

*Corr. Author's Address: China University of Mining & Technology, School of Mechanical Electronic & Information Engineering, Beijing, China; zhangx@cumtb.edu.cn

machines. The results showed that the piston with surface morphology has lower friction and leakage comparable to the traditional one. Ivantysynova and Baker [27] applied a sinusoidal micro-structured waved surface to the valve plate gap surface for reducing power loss, and their results show that the waved surface significantly reduce power losses at lower operating pressures; however, the leakage of waved surface designs are higher than that of the standard designs, which is caused by larger gap heights. Pelosi and Ivantysynova [28] numerically studied the cylinder block with a brass bushing. Their results showed that the wavy surface, caused by the thermal deformation of the brass bushing, has an impact on the energy dissipation generated by viscous friction and leakage flow. Shin and Kim [29] studied the influence of various peak-to-valley amplitudes and wavelengths of surface waviness on leakage power loss and friction power loss. Their results revealed that proper surface design can improve reliability and power efficiency. Shen and Khonsari [10] investigated the tribological and sealing performance of a piston ring with a specially designed textured surface in a diesel engine. They found that lasered pockets led to a reduction of up to about 15 % in the total friction between cylinder liner and piston assembly and also improved the sealing performance compared to untextured piston rings. For piston ring-liners (PRL), recent developments in ring surface modification through laser surface texturing have shown promising results in improving tribological characteristics. Usman and Park [12] considered asymmetric PRL contact of a textured piston ring in a distorted bore, and found that optimized surface textures improve the tribological performance of a PRL interface, whereas textures with large lateral aspect ratios have a detrimental effect. Rao et al. [16] studied the performance of the cylinder liner-piston ring with different surface textures (1 mm, 2 mm, 3 mm, and 4 mm widths) in marine diesel settings; the results showed that the 2 mm groove structure of the cylinder liner is more favourable for improving the wear performances at low speed, whereas a 3 mm groove structure of the cylinder liner is more suitable for improving the wear performance at higher speeds. Taken together, plentiful efforts have been carried out to improve the tribological properties and sealing performance via the rational design of surface morphology. However, little attention is paid to the effects of hierarchical morphology on the gap flow. Interestingly, many biological materials are hierarchically structured with wavy morphology, for example, towel gourd tendrils [30] and bovine horns [31].

Inspired by the unique hierarchical structures in nature, this paper proposed a hierarchical sinusoidal morphology for designing clearances between matching surfaces in water hydraulic systems in which poorer lubricity and larger leakage occur due to the lower viscosity of water. We tested the leakage flow of the models with 0th order, 1st order, and 2nd order sinusoidal structures on the water hydraulic annular clearance test rig. Further studies on the effects of waved surfaces with various amplitudes and wavelengths on leakage were carried out using numerical simulation. The velocity and pressure fields generated in the clearances were analysed to give further explanations of experimental observation. Both the experimental and simulated results suggest that hierarchical sinusoidal structures in the clearances between matching surfaces are beneficial to leakage reduction.

1 EXPERIMENTAL

1.1 Generation of the 2nd Order Sinusoidal Hierarchical Wave

The 2nd order sinusoidal curves were obtained based on the following equations[31]. As shown in Fig. 1, the sine arc length from the origin point O to an arbitrary point $N(p_1, q_1)$ can be described as follows:

$$s = \int_0^p \sqrt{1+\left(dq_1/dp_1\right)^2}\,dp_1 = \int_0^p \sqrt{1+\left[\frac{2\pi A_1}{\lambda_1}\cos\left(\frac{2\pi}{\lambda_1}p_1\right)\right]^2}\,dp_1, \quad (1)$$

where A_1 and λ_1 are the amplitude and wavelength of the 1st order sinusoidal curve C_1, p_1 and q_1 are horizontal and vertical coordinates, respectively. The sinusoidal 2nd order hierarchical wave C_2 is superimposed on the 1st order wave, and its amplitude A_2 and wavelength λ_2 can be calculated on the curvilinear coordinate system along C_1:

$$q_2 = A_2 \sin(\frac{2\pi}{\lambda_2}s). \quad (2)$$

Likewise, the 2nd order sinusoidal curve can be described by the equation in the XOY coordinate system with p as its free parameter:

$$x = p_1 - q_2 \sin\alpha, \quad (3)$$

$$y = q_1 + q_2 \cos\alpha, \quad (4)$$

where α is given by

$$\alpha = \tan^{-1}\left[\frac{2\pi A_1}{\lambda_1}\cos\left(\frac{2\pi}{\lambda_1}p_1\right)\right]. \quad (5)$$

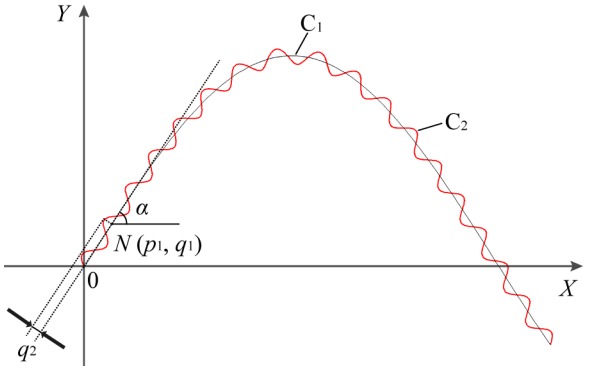

Fig. 1. *Illustration of the method for generating the 2nd order hierarchical wave*

1.2 Test Specimens

Three kinds of models were designed: 0th order model, 1st order sinusoidal model, and 2nd order sinusoidal model, as shown in Fig. 2. The clearance, δ, equals 0.2 mm. Compared to the 0th order model, the 1st order model is characterized by sinusoidal waviness with amplitude A_1 and wavelength λ_1. The 2nd order model has two-level hierarchical sinusoidal structures; apparently, it was superimposed on the 1st order sinusoidal structure with the amplitude $A_2 < A_1$ and wavelength $\lambda_2 < \lambda_1$.

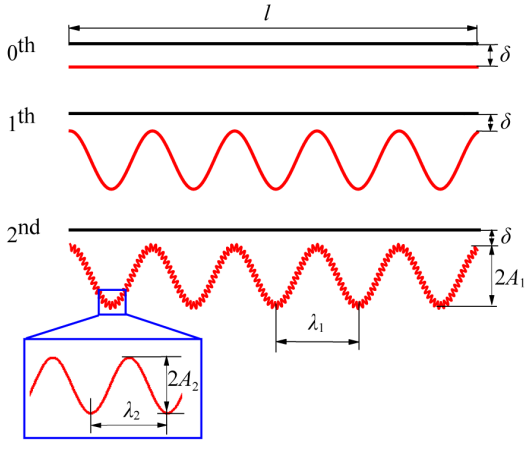

Fig. 2. *The clearance models with the 0th order, the 1st order, and the 2nd order sinusoidal morphology*

Three dimensional (3D) printing technology was considered to manufacture these models, and Lite 600 3D printer with 0.05 mm print precision was employed. The material used is Acrylonitrile Butadiene Styrene (ABS). The parameters of the 3D printed specimens are shown in Table 1, while 3D printed specimens are shown in Fig. 3. The whole length of the specimen is 131 mm, including both the work length 111 mm and the interference fit length 10 mm on its either ends. Enlarged views of the specimen are shown in Fig. 4.

Table 1. *The design and printed parameters of specimens*

Specimen	0th order	1st order	2nd order
Designed amplitude and wavelength [mm]	λ_1=0 λ_2=0 A_1=0 A_2=0	λ_1=10 λ_2=0 A_1=0.1250 A_2=0	λ_1=10 λ_2=1 A_1=0.1250 A_2=0.0500
Printed amplitude and wavelength [mm]	λ_1=0 λ_2=0 A_1=0 A_2=0	λ_1=10.0030 λ_2=0 A_1=0.1242 A_2=0	λ_1=10.0012 λ_2=1.0063 A_1=0.1310 A_2=0.0637
Design diameter [mm]	31.6000	31.6000	31.6000
Printed diameter [mm]	31.5460	31.5333	31.0547
Design clearance [mm]	0.2000	0.2000	0.2000
Printed clearance [mm]	0.2271	0.2334	0.4727

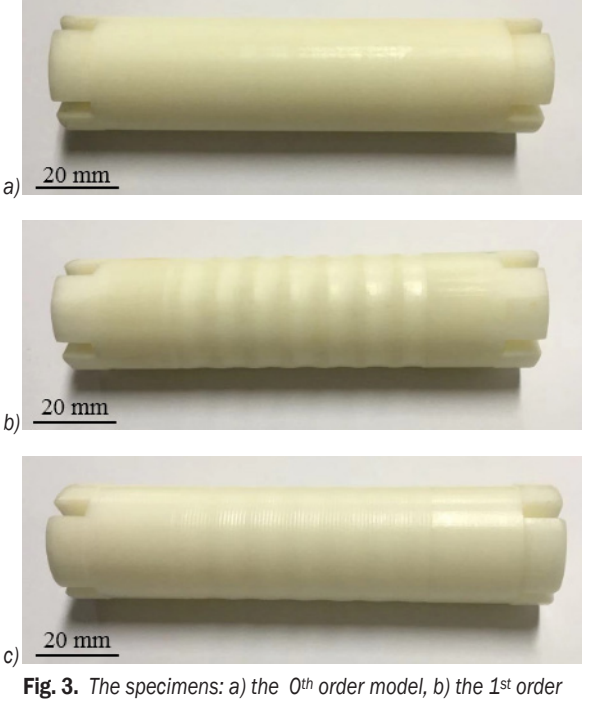

Fig. 3. *The specimens: a) the 0th order model, b) the 1st order model and c) the 2nd order model*

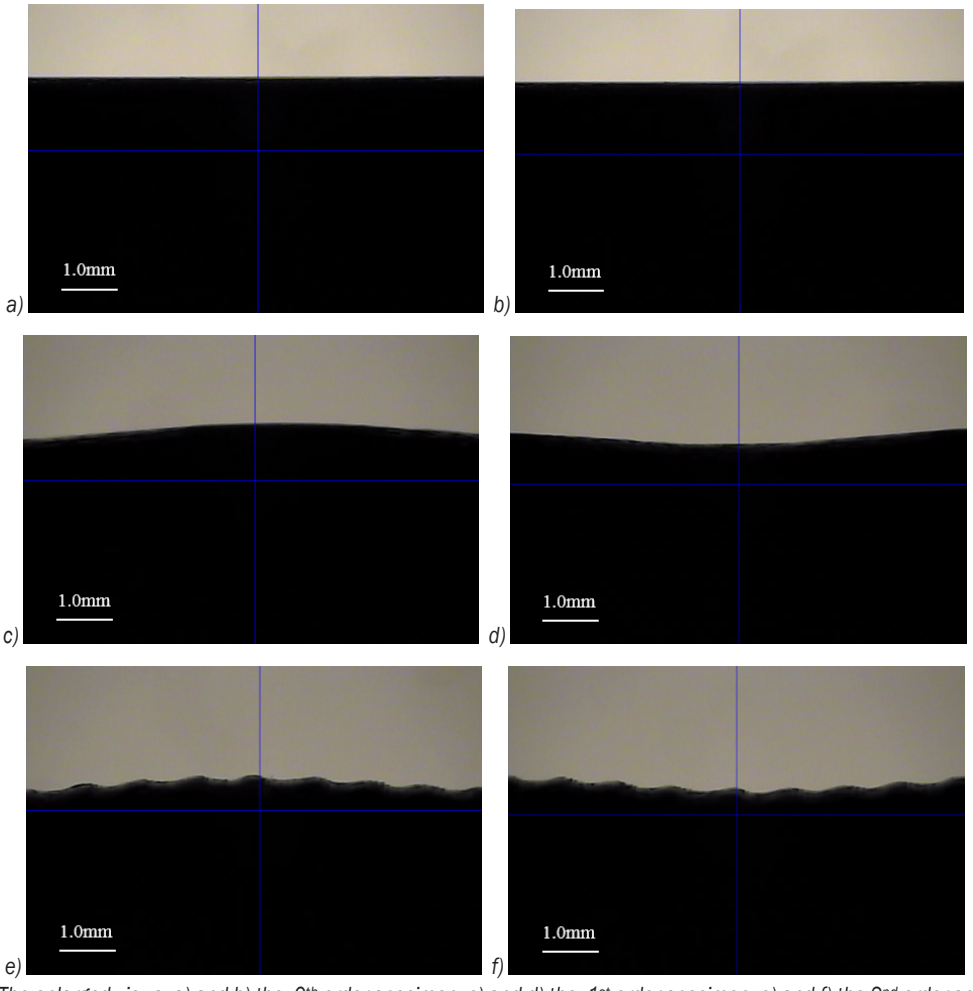

Fig. 4. *The enlarged views: a) and b) the 0th order specimen, c) and d) the 1st order specimen, e) and f) the 2nd order specimen*

1.3 Test Procedure and Results

In our leakage experiments, the internal diameter of the cylinder was 32.0 mm. As shown in Fig. 5, the interference fits between the cylinder and both ends of specimens were used to ensure the same clearance in the circumferential. The water pump was used, and the pressure difference between the inlet and outlet of the test cylinder was set to 0.2 MPa by regulating the throttle valve. The flow through the clearance between the cylinder and specimen was measured by the flow sensor. Clearance leakage flow of the 0th, the 1st, and 2nd order specimens were tested respectively on the water hydraulic annular clearance test rig. Obtained experimental data are displayed in Table 2. The results showed that the specimen with 2nd order structures has the largest gap size but the lowest leakage. It is well known that the larger clearance size will result

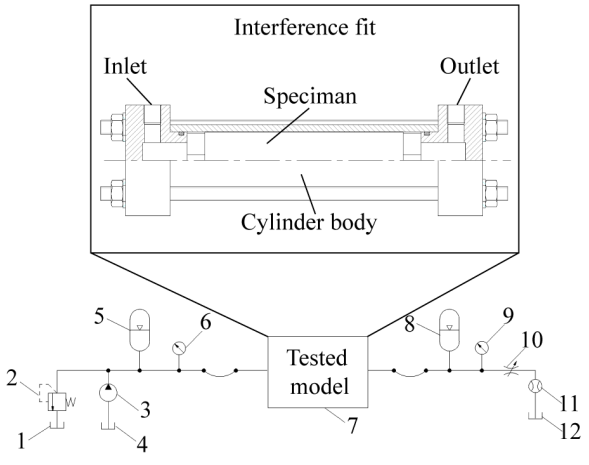

Fig. 5. *The schematic of the water hydraulic annular clearance test rig* (1, 4, 12 water tank, 2 hydraulic relief valve, 3 water pump, 5, 8 accumulator, 6, 9 pressure sensor, 7 rested model, 10 throttle valve, 11 flow sensor)

in larger leakage flow. Therefore, compared to the 0th order and the 1st order structures, the 2nd order structures can more effectively reduce the clearance leakage. Furthermore, the mechanism underlying the reduced leakage caused by the 2nd order structures was still unclear; thus, the numerical simulation was used to further study the effect of hierarchical sinusoidal morphology on clearance flow.

Table 2. *A comparison of numerical simulation results with experimental data*

Specimen	0th order	1st order	2nd order
Leakage by experiment [kg/s]	0.1352	0.1647	0.1302
Leakage by simulation [kg/s]	0.1426	0.1794	0.1421
Deviation [%]	5.5	8.9	9.1

2 NUMERICAL APPROACH

Reynolds number is the criteria to estimate the flow state, and it is defined as follows:

$$\mathrm{Re} = \frac{\rho v d_{\mathrm{H}}}{\mu}, \tag{6}$$

where ρ is the density, v is the velocity, μ is the viscosity, and d_{H} is the hydraulic diameter. For the annular gap, $d_{\mathrm{H}} = 2h$, h is the unilateral clearance size. Critical flow q_{c} can be written as:

$$\begin{aligned} q_{\mathrm{c}} = A v_{\mathrm{c}} &= \frac{\mathrm{Re}_{\mathrm{c}}\,\mu}{\rho d_{\mathrm{H}}} \cdot \pi\left(r_1 + r_2\right) h \\ &= \frac{\mathrm{Re}_{\mathrm{c}}\,\mu\pi\left(r_1 + r_2\right)}{2\rho}, \end{aligned} \tag{7}$$

where Re_{c} is the critical Reynolds number, r_1 is the inner radius of the cylinder, and r_2 is the radius of the specimen. While the flow is larger than q_{c}, the fluid flow transfer is from laminar to turbulent. For the tested models, the mass flow is larger than q_{c}; then it can be deduced that turbulent flow is generated in the clearance between the specimen and the cylinder.

Leakage flow is defined by the pressure difference over the seal. The clearance sealing performance of water hydraulic components under various pressure difference have been studied: 0.02 MPa **[32]**, 0.2 MPa **[33]** and **[34]**, 0.4 MPa **[33]**, 0.41 MPa **[35]**, 0.6 MPa **[33]**, 1.5 MPa **[36]**, 2 MPa **[36]** and **[37]**, 2.5 MPa **[36]**, 5 MPa **[38]**, 10 MPa **[38]**, 15 MPa **[38]**, 20 MPa **[38]**.In this article, the pressure difference between the inlet and outlet was set as 0.2 MPa. A two-dimensional (2D) axisymmetric model was adopted, and water was chosen as the working fluid. The clearances of the 0th order, the 1st order, and the 2nd order models were set as 0.2271 mm, 0.2334 mm, and 0.4727 mm, respectively, which were consistent with the clearance sizes used in experiments. To replicate conditions of the experimental setup, matching surfaces were treated as wall boundaries for numerical simulations. This study has been carried out with the commercial computational fluid dynamics (CFD) package from ANSYS FLUENT. A re-normalisation group (RNG) $k-\varepsilon$ model was used to predict the clearance turbulent flow. This model is a two-equation turbulence model that is derived by using renormalization group methods **[39]**; it significantly improves the responsiveness to the effects of rapid strain and streamline curvature **[40]** and **[41]** and predicts more swirls and has better treatment of near-wall turbulence effects **[42]** and **[43]**. It predicted well the numerical results that agree with experimental results. The SIMPLEC algorithm is implemented in FLUENT, and the pressure-based solver and Green-Gauss node-based gradient treatment were chosen to obtain fast and accurate converging solutions for unstructured triangular grids. 2nd order discretization scheme was used for all governing equations. The desired convergence target was that the root mean square residuals of the momentum and mass equations, energy equation, and turbulence equations would reach 10^{-5}.

The whole mesh generation process was carried out in Pointwise 17.4 software. The computational model was qualified with unstructured triangular mesh, and the schematic diagrams of the grid are shown in Fig. 6. Refined meshes are adapted at both the inlet/outlet and wall boundaries to capture the detailed flowing behaviour, while relatively coarser mesh was used in other regions. Furthermore, grid dependence and convergence studies were performed, as depicted in Fig. 7. The selected nodes number of computational models in this paper is around 150,000 to 200,000. With this resolution, obtaining a stationary solution required approximately 200 minutes on an Intel E5 workstation with 32G/2133ECC. Finally, the mass flow of the 0th order, the 1st order and the 2nd order models were calculated numerically. The results are shown in Table 2; it can be seen from the numerical simulation results that the 2nd order one has the least leakage flow, and the 1st order one is with the largest flow. Furthermore, numerical simulation has shown a good agreement with experimental data, with errors of less than 10 %. The simulation methods were verified with our experiments.

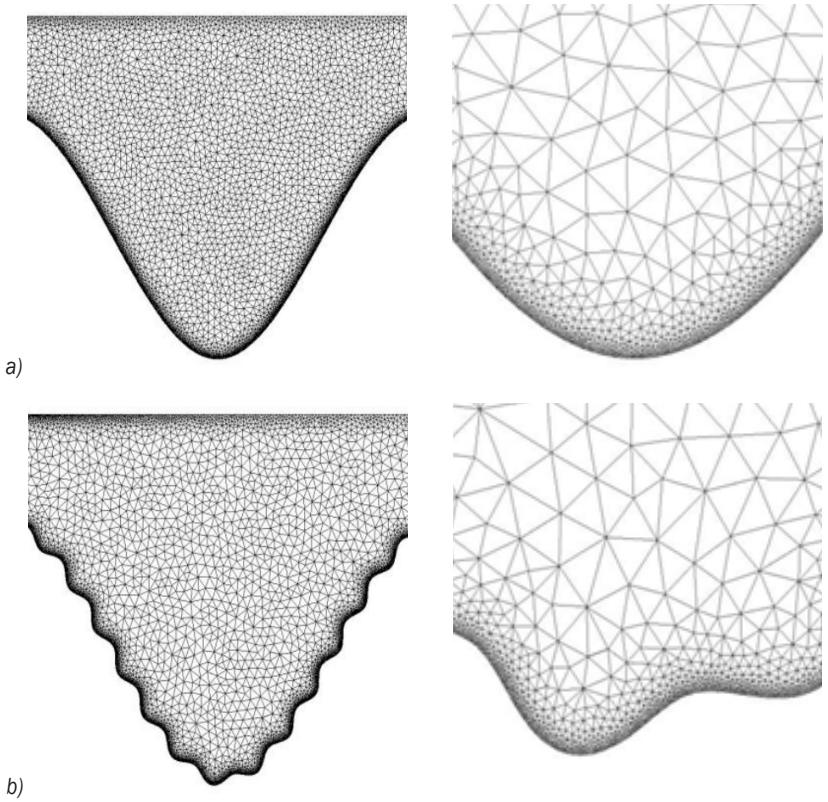

Fig. 6. *Meshes used for models: a) The 1st order model; b) the 2nd order model*

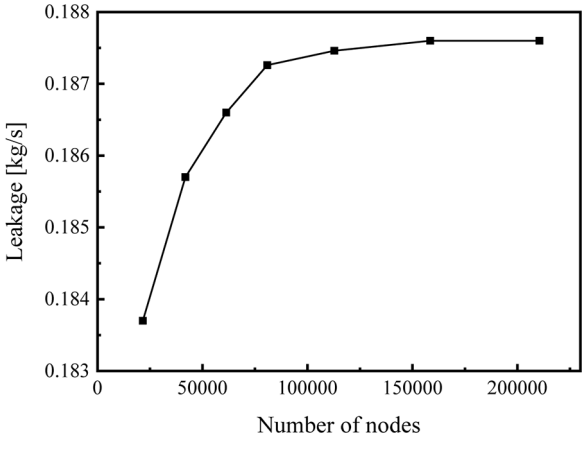

Fig. 7. *An example of grid dependence of the CFD results*

3 THE EFFECT OF VARIOUS SINUSOIDAL MORPHOLOGY ON LEAKAGE

3.1 Simulation Models

The numerical investigation for the effect of multilevel sinusoidal morphology on leakage was carried out with various amplitudes and wavelengths. Matching surfaces were assumed to be rigid bodies, and the temperature of the fluid was assumed to be constant in this paper, in order to focus on the influences of the surface morphology on clearance flow. The 1st order models were controlled by the amplitude A_1 of 0.25 mm, 0.5 mm and 1.0 mm, and the wavelength λ_1 within the range of 0.125 mm to 10 mm. The parameters of the 2nd order model, A_2 equals to 0.01 mm, 0.03 mm and 0.05 mm, respectively, and λ_2 takes value in 0.02 mm to 0.4 mm. As shown in Fig. 2, three kinds of 2D axisymmetric models were calculated. The length, l, was set to be 10 mm, the clearance, δ, equals to 0.2 mm.

3.2 Influence of the 1st Order Sinusoidal Morphology on Sealing Performance

A dimensionless parameter, Q_1/Q_0, was introduced to estimate the seal efficiency of the 1st order model compared to the 0th order one, and another dimensionless parameter, ε_1, was defined by A_1/λ_1, to characterize the surface shape of the 1st order sinusoidal morphology. Firstly, the 0th order

model was simulated numerically, giving numerical leakage flow of Q_0=0.5545 kg/s. Similarly, leakage Q_1 for the waved surface of varying amplitudes and wavelengths, for 1st order models were obtained and compared with the 0th order model under the same operating conditions. As shown in Fig. 8, the water leakage Q_1/Q_0 decreases firstly and then increases with the increments in parameter ε_1. The lowest leakage Q_1 was achieved at A_1=1 mm, ε_1=4 with up to 43.3 % reduction in $(1-Q_1/Q_0)$. However, as the small value of parameter ε_1 is taken, the sealing performance is worsened by the 1st order sinusoidal structure. Specifically, as the value of ε_1 is less than 0.15, 0.2 and 0.4 for the three models respectively (A_1=0.25 mm, 0.5 mm and 1.0 mm), the value of Q_1/Q_0 is more than 1.

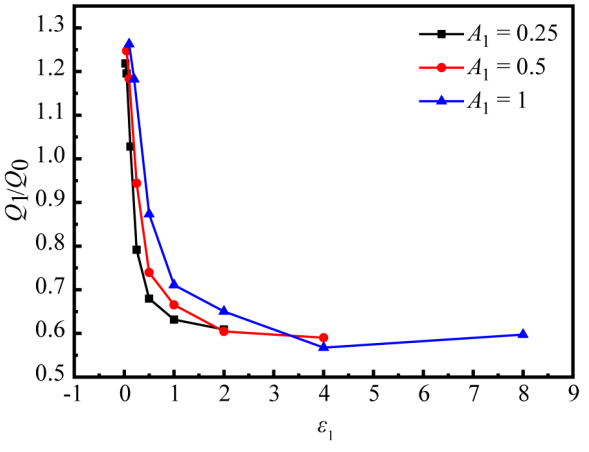

Fig. 8. *The seal efficiency of the 1st order models*

3.3 Influence of the 2nd Order Sinusoidal Morphology on Sealing Performance

The 2nd order models with sinusoidal morphology superimposed on the 1st order model of A_1=0.25 mm and λ_1=1 mm were established and computed. The dimensionless parameter ε_2 was defined by A_2/λ_2, to characterize the waved shape of the 2nd order sinusoidal morphology. Fig. 9 depicts the sealing efficiency of the 2nd order sinusoidal morphology models. The leakages of the 2nd order models are lower than that of the 1st order models. In detail, it can be seen that the maximum leakage reduction $(1-Q_2/Q_1)$ is 18 %, which means the sealing efficiency is effectively improved by the 2nd order sinusoidal morphology. However, when the parameter ε_2 is relatively small, larger leakage is generated due to the existence of larger clearance fields and less energy dissipation.

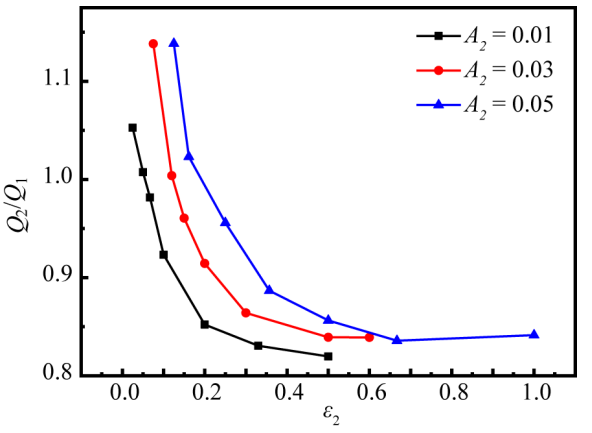

Fig. 9. *The seal efficiency of the 2nd order models*

4 FLUID FIELD ANALYSIS

To further explore the sealing performance of the 1st order and the 2nd order models, their streamlines distributions were plotted in Figs. 10a and b, respectively. The enlarged local views of the 2nd order wavy teeth were also presented in Fig. 10c for better observation. As indicated in Fig. 10a, one big rotating vortex is observed in each cell of the 1st order model, which causes a decrease in leakage by dissipating fluid kinetic energy. Similarly, for the 2nd order model, a big vortex is also generated in the middle region of each cavity, as shown in Fig. 10b. More interestingly, numerous 3rd order vortexes with reverse rotation can be found in the 2nd order wavy cavities. Moreover, the tertiary vortexes can also be found at the teeth tips of the throttling area of the 2nd order model, as shown in Fig. 10c. All the vortexes in various levels will contribute to dissipate more fluid kinetic energy resulting in a reduction in leakage in the case of the 2nd order model. In addition, compared to the 1st order model, a narrower-width main flow was generated by introducing the hierarchical sinusoidal morphology in the 2nd order model, which would lead to less leakage in the 2nd order model.

The velocity of the main flow along the X direction plays a major role in surface wear and gap leakage. The X component of velocity contour was shown in Fig. 11. The results show that the velocity of flow in clearance is 6 m/s to 13 m/s in the 1st order model, but 4 m/s to 11 m/s in the 2nd order model. Lower velocity along the X direction in the 2nd order model helps achieve less fluid erosion between the matching surfaces, and it also gives a further explanation for its lower leakage. The high-velocity fluid through the clearances will cause the fluid

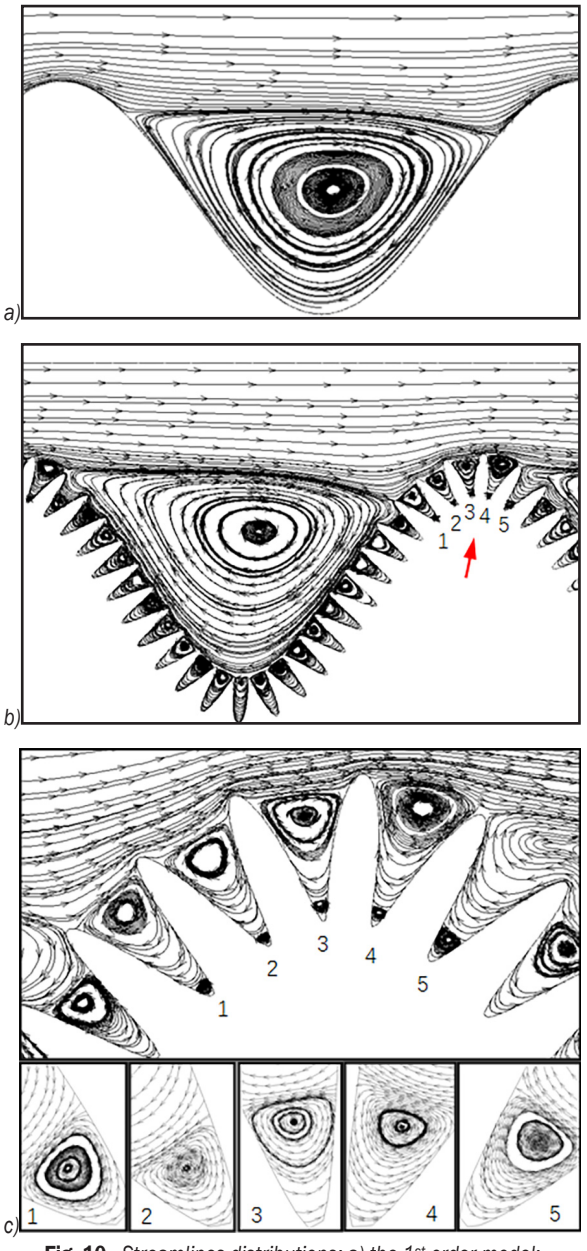

Fig. 10. *Streamlines distributions: a) the 1st order model; b) the 2nd order model; c) the enlarged views of the 2nd order models (arrows in b)*

erosion, called "wire drawing". Moreover, the wear of the matching surfaces will also inevitably enlarge the clearance, which will increase the leakage. Fig. 12 depicts the statistical results of velocity magnitudes in the flow field of the 1st order and 2nd order models. The velocity magnitude in about 70 % fluid fields is less than 3 m/s for the 1st order model. Comparatively, about 85 % zones of the 2nd order model are with the velocity of less than 1 m/s.

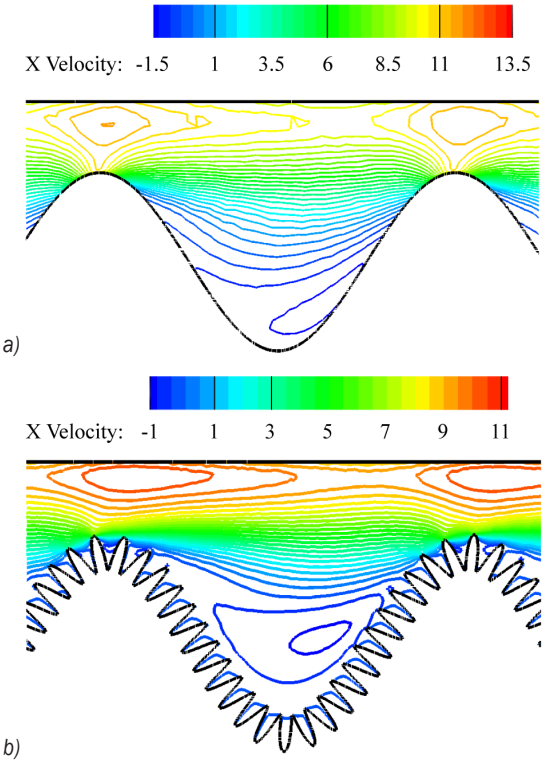

Fig. 11. *The X velocity component contours: a) the 1st order model; b) the 2nd order model*

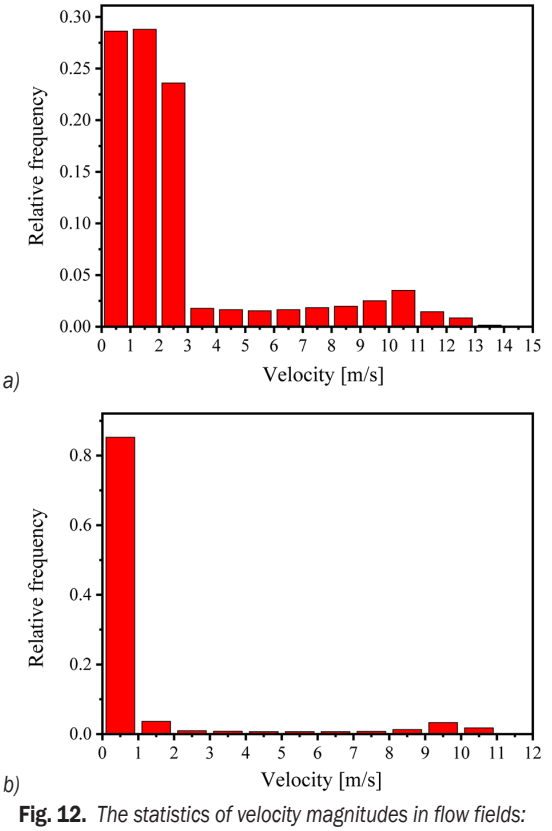

Fig. 12. *The statistics of velocity magnitudes in flow fields: a) the 1st order model; b) the 2nd order model*

Surfacing texturing is a powerful method of enhancing hydrodynamic load carrying capacity. As indicated in Fig. 13, the pressure distribution of models with the 0th order, 1st order and 2nd order structures were given respectively. Firstly, the pressure decreases smoothly from the inlet to the outlet for the 0th order model but drops gradually for the 1st order and 2nd order models, and the pressure in the 2nd order gap drops faster than that of the other two models. Moreover, the waved surface generated numbers of convergent wedge-shaped areas in the clearance, causing changes in the thickness of the fluid film, which contribute to additional hydrodynamic pressure generation. As shown in Figs. 13b and c, the pressure mainly dropped at peaks but remained stable in the chambers of waved troughs. Furthermore, for each peak in the waved surface, there is a corresponding peak in the pressure field. A micro-hydrodynamic effect was induced by the waved surface and created an additional load carrying capability, separating the matching surfaces.

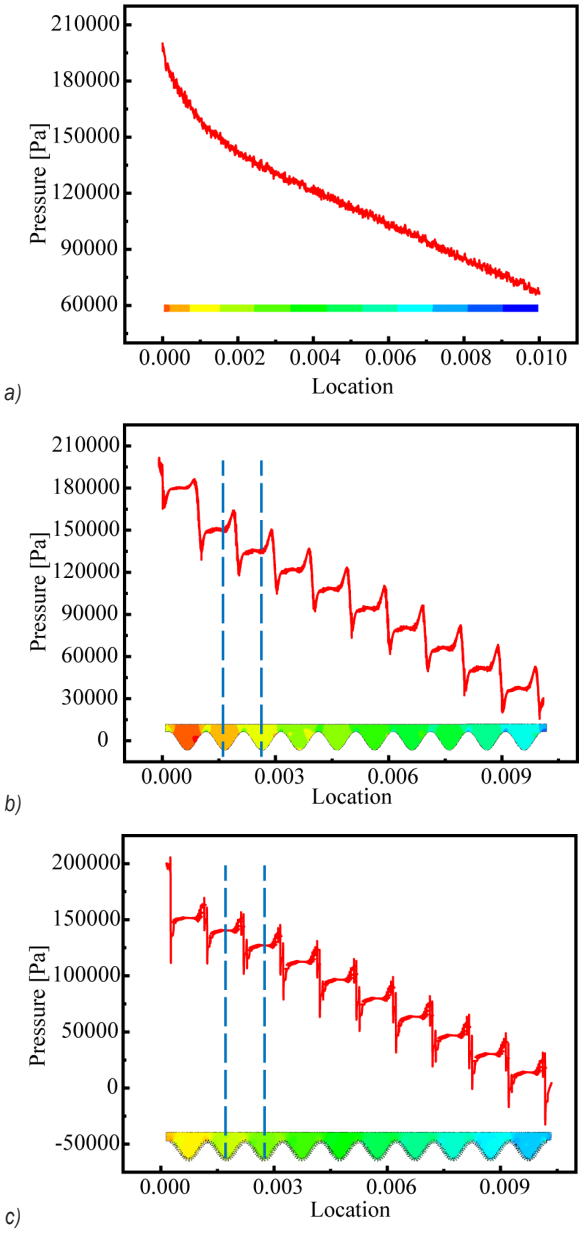

Fig. 13. *Comparisons of pressure distribution: a) the 0th order model; b) the 1st order model; c) the 2nd order model*

5 CONCLUSIONS

The hierarchical sinusoidal morphology was introduced to the clearance of matching surfaces in water hydraulic systems where poorer lubricity and larger leakage exist due to the lower viscosity of water. Both the numerical and experimental results show that introducing hierarchical morphology on matching surfaces will reduce leakage. The models of the 0th order, the 1st order and the 2nd order with various amplitudes and wavelengths were studied. For the 1st order and the 2nd order models, the leakage reduces with the increase in the ratio of the amplitude to wavelength. Further study of the flow field reveals that the significant leakage reductions of the 2nd order sinusoidal models are obtained due to the extra vortexes of various scales in the 2nd order wavy cavities, which dissipate more fluid kinetic energy, contributing towards a mechanism to reduce leakage. In addition, the narrower width of the main flow and lower X component of velocity in the 2nd order models compared to that of the 1st order models also make contributions to the lower leakage. Moreover, the waved surfaces produce changes in the thickness of the fluid film, which contributes to create an additional load carrying capability and reduce wear. We conclude that the exciting results obtained from introducing the hierarchical waved surface have a huge potential application to reduce energy loss in hydraulic systems and give a new way to design clearances between matching surfaces.

6 ACKNOWLEDGEMENTS

Supports from the National Natural Science Foundation of China (Grant No. 51475197) are acknowledged.

7 NOMENCLATURE

A_1 amplitude of 1st order cosinoidal waviness, [mm]
A_2 amplitude of 2nd order cosinoidal waviness, [mm]
λ_1 wavelength of 1st order consinoidal waviness, [mm]
λ_2 wavelength of 2nd order consinoidal waviness, [mm]
ε_1 dimensionless parameter, defined by A_1/λ_1
ε_2 dimensionless parameter, defined by A_2/λ_2
Q_0 leakage of straight labyrinth seal, [kg/s]
Q_1 leakage of 1st order labyrinth seal, [kg/s]
Q_2 leakage of 2nd order labyrinth seal, [kg/s]
L length of labyrinth seals, [mm]
δ clearance of labyrinth seals, [mm]
ρ density, [kg/m^3]
μ Viscosity, [Pa·s]
d_H hydraulic diameter, [mm]
v Velocity, [m/s]
h unilateral clearance size, [mm]
q_c critical flow, [kg/s]

8 REFERENCES

[1] Lim, G.H., Chua, P.S.K., He, Y.B. (2003). Modern water hydraulics-the new energy-transmission technology in fluid power. *Applied Energy*, vol. 76, no. 1-3, p. 239-246, **DOI:10.1016/s0306-2619(03)00064-3**.

[2] Urata, E. (1999). Technological aspects of the new water hydraulics. *Proceedings of The 6th Scandinavian International Conference on Fluid Power*, p. 21-34.

[3] Krutz, G.W., Chua, P.S. (2004). Water hydraulics–theory and applications. *Workshop on Water Hydraulics, Agricultural Equipment Technology Conference*, p. 8-10.

[4] Koskinen, K.T., Leino, T., Riipinen, H. (2008). Sustainable development with water hydraulics-possibilities and challenges. *Proceedings of the JFPS International Symposium on Fluid Power*, no. 7-1, p. 11-18, **DOI:10.5739/isfp.2008.11**.

[5] Etsion, I. (2004). State of the art in laser surface texturing. *ASME 7th Biennial Conference on Engineering Systems Design and Analysis*, p. 585-593, **DOI:10.1115/ESDA2004-58058**.

[6] Pantelis, D.I., Pantazopoulos, G., Antoniou, S.S. (1997). Wear behavior of anti-galling surface textured gray cast iron using pulsed-Co_2 laser treatment. *Wear*, vol. 205, no. 1-2, p. 178-185, **DOI:10.1016/s0043-1648(96)07339-5**.

[7] Dumitru, G., Romano, V., Weber, H.P, Haefke, H., Gerbig, Y., Pflüger, E. (2000). Laser microstructuring of steel surfaces for tribological applications. *Applied Physics A*, vol. 70, no. 4, p. 485-487, **DOI:10.1007/s003390051073**.

[8] Bifeng, Y., Dashu, G., Shao, S., Bo, X., Hekun, J. (2018). Research on the profile design of surface texture in piston ring of internal combustion engine. *Journal of Tribology*, vol. 140, no. 6, p. 061701, **DOI:10.1115/1.4039957**.

[9] Wang, X., Kato, K., Adachi, K., Aizawa, K. (2001). The effect of laser texturing of SiC surface on the critical load for the transition of water lubrication mode from hydrodynamic to mixed. *Tribology International*, vol. 34, no. 10, p. 703-711, **DOI:10.1016/S0301-679X(01)00063-9**.

[10] Shen, C., Khonsari, M. (2016). Tribological and sealing performance of laser pocketed piston rings in a diesel engine. *Tribology Letters*, vol. 64, no. 2, p. 26, **DOI:10.1007/s11249-016-0757-9**.

[11] Erinosho, M.F., Akinlabi, E.T. (2018). Influence of laser power on improving the wear properties of laser-deposited Ti-6Al-4V+B4C composite. *Strojniski vestnik - Journal of Mechanical Engineering*, vol. 64, no. 7-8, p. 488-495, **DOI:10.5545/sv-jme.2018.5362**.

[12] Usman, A., Park, C.W. (2017). Numerical investigation of tribological performance in mixed lubrication of textured piston ring-liner conjunction with a non-circular cylinder bore. *Tribology International*, vol. 105, p. 148-157, **DOI:10.1016/j.triboint.2016.09.043**.

[13] Nanbu, T., Ren, N., Yasuda, Y., Zhu, D., Wang, Q.J. (2008). Micro-textures in concentrated conformal-contact lubrication: Effects of texture bottom shape and surface relative motion. *Tribology Letters*, vol. 29, no. 3, p. 241-252, **DOI:10.1007/s11249-008-9302-9**.

[14] Shen, C. (2016). *Design of Surface Texture for the Enhancement of Tribological Performance*. PhD thesis Louisiana State University and Aqricultural and Mechanical College, Baton Rouge.

[15] Zabala, B., Igartua, A., Férnandez, X., Priestner, C., Ofner, H., Knaus, O., Abramczuk, M., Tribotte, P., Girot, F., Roman, E., Nevshupa, R. (2017). Friction and wear of a piston ring/cylinder liner at the top dead centre: Experimental study and modelling. *Tribology International*, vol. 106, p. 23-33, **DOI:10.1016/j.triboint.2016.10.005**.

[16] Rao, X., Sheng, C., Guo, Z., Yuan, C. (2019). Influence of surface groove width on tribological performance for cylinder liner-piston ring components. *Tribology Transactions*, in Press, p. 1-10, **DOI:10.1080/10402004.2018.1539201**.

[17] Etsion, I., Halperin, G. (2002). A laser surface textured hydrostatic mechanical seal. *Tribology Transactions*, vol. 45, no. 3, p. 430-434, **DOI:10.1080/10402000208982570**.

[18] Etsion, I. (2013). Modeling of surface texturing in hydrodynamic lubrication. *Friction*, vol. 1, no. 3, p. 195-209, **DOI:10.1007/s40544-013-0018-y**.

[19] Han, Y., Fu, Y. (2018). Investigation of surface texture influence on hydrodynamic performance of parallel slider bearing under transient condition. *Meccanica*, vol. 53, no. 8, p. 2053-2066, **DOI:10.1007/s11012-017-0809-8**.

[20] Kango, S., Sharma, R.K., Pandey, R.K. (2014). Comparative analysis of textured and grooved hydrodynamic journal bearing. *Proceedings of the Institution of Mechanical Engineers, Part J: Journal of Engineering Tribology*, vol. 228, no. 1, p. 82-95, **DOI:10.1177/1350650113499742**.

[21] Bergseth, E., Sjöberg, S.r., Björklund, S. (2012). Influence of real surface topography on the contact area ratio in differently manufactured spur gears. *Tribology International*, vol. 56, p. 72-80, **DOI:10.1016/j.triboint.2012.06.014**.

[22] Bergseth, E., Olofsson, U., Lewis, R., Lewis, S. (2012). Effect of gear surface and lubricant interaction on mild wear. *Tribology Letters*, vol. 48, no. 2, p. 183-200, **DOI:10.1007/s11249-012-0004-y**.

[23] Wondergem, A.M., Ivantysynova, M. (2014). The impact of the surface shape of the piston on power losses. *In 8th FPNI Ph. D Symposium on Fluid Power*, p. V001T02A008, **DOI:10.1115/fpni2014-7843**.

[24] Ivantysynova, M. (2012). The piston cylinder assembly in piston machines–a long journey of discovery. *Proceedings of 8th IFK International Conference on Fluid Power*, p. 307-332.

[25] Ivantysynova, M., Lasaar, R. (2004). An investigation into micro-and macrogeometric design of piston/cylinder assembly of swash plate machines. *International Journal of Fluid Power*, vol. 5, no. 1, p. 23-36, **DOI:10.1080/14399776.2004.10781181**.

[26] Kleist, A. (1997). Design of hydrostatic bearing and sealing gaps in hydraulic machines: a new simulation tool. *5th Scandinavian International Conference on Fluid Power*, p. 157-169.

[27] Ivantysynova, M., Baker, J. (2009). Power loss in the lubricating gap between cylinder block and valve plate of swash plate type axial piston machines. *International Journal of fluid power*, vol. 10, no. 2, p. 29-43, **DOI:10.1080/14399776.2009.10780976**.

[28] Pelosi, M., Ivantysynova, M. (2011). Surface deformations enable high pressure operation of axial piston pumps. *ASME Dynamic Systems and Control Conference and ASME Symposium on Fluid Power and Motion Control*, p. 193-200, **DOI:10.1115/dscc2011-5979**.

[29] Shin, J.-H., Kim, K.-W. (2014). Effect of surface non-flatness on the lubrication characteristics in the valve part of a swash-plate type axial piston pump. *Meccanica*, vol. 49, no. 5, p. 1275-1295, **DOI:10.1007/s11012-014-9893-1**.

[30] Wang, J.-S., Wang, G., Feng, X.-Q., Kitamura, T., Kang, Y.-L., Yu, S.-W., Qin, Q.-H. (2013). Hierarchical chirality transfer in the growth of towel gourd tendrils. *Scientific Reports*, vol. 3, p. 3102, **DOI:10.1038/srep03102**.

[31] Li, B.-W., Zhao, H.-P., Qin, Q.-H., Feng, X.-Q., Yu, S.-W. (2012). Numerical study on the effects of hierarchical wavy interface morphology on fracture toughness. *Computational Materials Science*, vol. 57, p. 14-22, **DOI:10.1016/j.commatsci.2011.01.032**.

[32] Saba Y., Basim A., Nehad A.(2014). Prediction of carry-over coefficient for fluid flow through teeth on rotor labyrinth seals using computational fluid dynamics. *Iraqi Journal of Mechanical and Material Engineering*, vol. 14, no. 3, p. 346-366.

[33] Ma, R., Wang, K. (2010). CFD numerical simulation and experimental study of effects of screw-sleeve fitting clearance upon triangular thread labyrinth screw pump (LSP) performance. *Journal of Applied Fluid Mechanics*, vol. 3, no. 1, p. 75-81.

[34] Watson, C., Untaroiu, A., Wood, H.G., Weaver, B.K., Morgan, N., Jin, H. (2016). Response surface mapping of performance for helical groove seals with incompressible flow. *ASME Turbo Expo: Turbomachinery Technical Conference and Exposition*, p. V07BT31A036, **DOI:10.1115/gt2016-57945**.

[35] Demko, J.A., Morrison, G.L., Rhode, D.L. (1989). The prediction and measurement of incompressible flow in a labyrinth seal. *Journal of Engineering for Gas Turbines and Power*, vol. 111, no. 4, p. 697-702, **DOI:10.1115/1.3240315**.

[36] Marsis, E., Morrison, G. (2013). Leakage and rotordynamics numerical study of circular grooved and rectangular grooved labyrinth seals. *ASME Turbo Expo: Turbine Technical Conference and Exposition*, p. V07AT29A028, **DOI:10.1115/GT2013-96001**.

[37] Zhao, W., Nielsen, T.K., Billdal, J.T. (2010). Effects of cavity on leakage loss in straight-through labyrinth seals. *IOP Conference Series: Earth and Environmental Science*, vol. 12, p. 012002, **DOI:10.1088/1755-1315/12/1/012002**.

[38] Strmčnik, E., Majdič, F. (2017). Comparison of leakage level in water and oil hydraulics. *Advances in Mechanical Engineering*, vol. 9, no. 11, p. 1-12, **DOI:10.1177/1687814017737723**.

[39] Smith, L.M., Woodruff, S.L. (1998). Renormalization-group analysis of turbulence. *Annual Review of Fluid Mechanics*, vol. 30, no. 1, p. 275-310, **DOI:10.1146/annurev.fluid.30.1.275**.

[40] Govardhan, M., Sampat, D.L. (2005). Computational studies of flow through cross flow fans-effect of blade geometry. *Journal of Thermal Science*, vol. 14, no. 3, p. 220-229, **DOI:10.1007/s11630-005-0005-3**.

[41] Myong, H.K., Yang, S.Y. (2003). Numerical study on flow characteristics at blade passage and tip clearance in a linear cascade of high performance turbine blade. *KSME International Journal*, vol. 17, no. 4, p. 606-616, **DOI:10.1007/bf02984462**.

[42] Nayak, K., Ansari, A., Musthafa, M., De, S. (2013). The effect of rub-grooves on leakage and windage heating in labyrinth seals with honeycomb lands. *43rd AIAA/ASME/SAE/ASEE Joint Propulsion Conference & Exhibit*, p. 5737, **DOI:10.2514/6.2007-5737**.

[43] Pospelov, A.Y., Zharkovskii, A.A. (2015). Effect of the parameters of a computational model on the prediction of hydraulic turbine characteristics. *Power Technology and Engineering*, vol. 49, no. 3, p. 159-164, **DOI:10.1007/s10749-015-0591-5**.

Strojniški vestnik - Journal of Mechanical Engineering 65(2019)5, 287-296
DOI:10.5545/sv-jme.2018.5845
Original Scientific Paper
Received for review: 2018-11-28
Received revised form: 2019-03-22
Accepted for publication: 2019-04-03

Grounding Characteristics of a Non-Pneumatic Mechanical Elastic Tire in a Rolling State with a Camber Angle

Xianbin Du[1,*] – Youqun Zhao[2] – Qiang Wang[1] – Hongxun Fu[3] – Fen Lin[2]
[1]Shandong University of Science and Technology, College of Transportation, China
[2]Nanjing University of Aeronautics and Astronautics, College of Energy and Power Engineering, China
[3]Shandong University of Technology, School of Transportation and Vehicle Engineering, China

A non-pneumatic mechanical elastic tire (ME wheel) was introduced, and the grounding characteristics of the ME wheel under a rolling condition with a camber angle were investigated with the combination of finite element simulation and experimental research. According to the ME wheel structure and material characteristics, a numerical simulation model of the ME wheel was established using the finite element (FE) method. The stiffness tests were carried out to verify the accuracy of the simulation model of the ME wheel. To highlight the advantages of the ME wheel, an inflatable tire was selected as the reference tire, and the grounding characteristics of these two tires with different camber angles were compared and analysed in free rolling, braking, and driving conditions. Different slip ratio values for the ME wheel and inflatable tire were applied in driving conditions to analyse the influence of the slip ratio on the grounding characteristics. The obtained results indicated that both the ME wheel and inflatable tire will gradually suffer partial wear of the tread surface as the camber angle increases, but the pressure concentration of the inflatable tire is more serious. The research can provide a basis for structural optimization and comprehensive mechanical performance analysis of the ME wheel.

Keywords: wheel, grounding characteristics, finite element analysis, contact pressure, camber angle

Highlights

- *An innovative safety tire with a catenary structure was introduced.*
- *An FE model of ME wheel which includes material nonlinear, large deformation and the anisotropy of rubber was established.*
- *The influence of the camber angle on the grounding characteristics of the ME wheel was analysed.*
- *The grounding characteristics of the ME wheel under different rolling states were compared and analysed with an inflatable tire.*
- *As the camber angle increases, both the ME wheel and inflatable tire will suffer partial wear of the tread, but it is more serious with the inflatable tire.*

0 INTRODUCTION

The invention of the inflatable tire was a great advancement. It brings comfort and convenience to people, but it also brings new troubles such as nailing, leaking, and puncture **[1]** and **[2]**. According to the statistics from the transportation department of China, serious traffic accidents caused by tire leakage and bursting accounted for nearly 50 % of the total accidents, especially on expressways **[3]**.

To solve the problem of tire inflation-free and safety, many research and production departments have been devoted to the study of safety tire technology and achieved many positive results **[4]** to **[6]**. Michelin launched an inflation-free radial tire called "Tweel"; it is a single unit that replaces the current inflatable tire assembly **[7]**. Narasimhan et al. **[8]** analysed the influence of material factors on the vertical stiffness and vibration characteristics of the Tweel during the rolling state. Ma et al. **[9]** studied the interaction between the Tweel and soil using the finite element (FE) method, and the established model can be utilized to analyse traction characteristics on a particular terrain. Kim and Kim **[10]** analysed the load-carrying properties and ground pressure of a non-pneumatic tire with a hexagonal honeycomb structure. In addition, the application of leak-proof technology and run-flat tires has also greatly improved the safety of vehicles.

The mechanical elastic (ME) wheel investigated in the paper was a non-pneumatic safety tire with catenary structure, and it was developed to improve the mobility and safety of vehicles under harsh environment and driving conditions, such as rugged terrain and macadam pavement **[11]** and **[12]**. Since the ME wheel adopts a non-inflatable design, there is no danger of air leakage, puncture, etc. during the rolling process. Moreover, due to the use of a catenary structure, the ME wheel not only has the comfort and manoeuvrability of inflatable tires but also has the durability and damage resistance of airless tires.

As the basis of the vehicle system dynamics, many difficulties exist in the study of tire-pavement interaction. This is mainly due to the composite

*Corr. Author's Address: Shandong University of Science and Technology, Qingdao, China, duxianbin@sdust.edu.cn

structure of a tire and its complex force and rolling conditions in the process of interaction with the pavement [13] and [14]. To deeply study the mechanical properties of tires, researchers have carried out a great deal of theoretical and experimental work and achieved fruitful results [15] to [17]. Song et al. [18] studied the temperature distribution of a tire under the rolling condition by the FE method. Nishiyama et al. [19] used a combination of finite element and discrete element to analyse the tire traction performance, and a new element conversion algorithm for interchanging between finite element and discrete element was developed to increase the computational efficiency. A tire-road coupled simulation system, which considers the viscoelastic characteristics of road and temperature fields, was developed by Han et al. [20] to analysed the track in various conditions. Tamada and Shiraishi [21] introduced a method of wear process simulation to predict the uneven wear of the tire, and the transformation of tire pattern shape and wear energy can be easily obtained with this method. Based on the mixed Lagrangian-Eulerian method, Wei et al. [22] and [23] proposed a new method to analyse the rolling noise of the tire. By comparing the simulation data with the test data, this new method has reliable prediction accuracy. Anderson and McPillan [24] studied the trade-off between tire wear and handling with a multi-objective optimization method and scaling factors derived from the Michelin TameTire model.

It can be seen that many achievements and experiences have been obtained in the study of tire mechanics. However, the research on the tire mechanics considering the effect of the camber angle is still relatively rare due to the complexity of the camber performance [25]. Kagami et al. [26] proposed an analytical method to analyse the contact deformation of a tire with the camber angle, and the predicted results were compared with the measured results. El-Gawwad et al. [27] presented a multi-spoke tire model to analyse the tire-terrain interaction and studied the effect of the camber angle on the tire performance.

Generally, the camber angle has a significant influence on the wheel steering and the rational selection of alignment parameters. The presence of the camber angle will result in a pair of opposite lateral forces on the tire, which will directly affect the lateral stability, dynamic and abnormal tread wear of the vehicle, especially in emergency situations such as sharp turn, obstacle avoidance, and overtaking. Therefore, it is necessary to study the grounding characteristics of ME wheel when considering the effect of the camber angle.

The primary objective of this research is to study the grounding characteristics of the ME wheel with camber angle in free rolling, braking and driving conditions. The cord-rubber composite was simulated by rebar model and the ME wheel finite element model was verified through the stiffness test. The pressure distribution of ME wheel and inflatable tire with different rolling conditions and camber angles were simulated, and the obtained simulation results were compared and discussed in detail. The research results can be a basis for the ME wheel structure optimization and compressive performance analysis.

1 MAIN STRUCTURE COMPOSITION

As a new type of safety tire, the ME wheel adopts an ingenious structural arrangement, which simplifies the traditional wheel and tire into an integrated structure. Fig. 1 shows the physical prototype of the ME wheel, and its main components include an external flexible tire body, a suspension hub, and multiple sets of hinges that are evenly distributed along the circumference of the ME wheel. The hinge mechanism is a three-bar structure. When the ME wheel is subjected to lateral force, a certain lateral deformation will occur due to the elasticity of the flexible tire body structure. The lateral stiffness of the ME wheel is larger than that of pneumatic tires under the same conditions so that the handling stability of the vehicle can be well ensured.

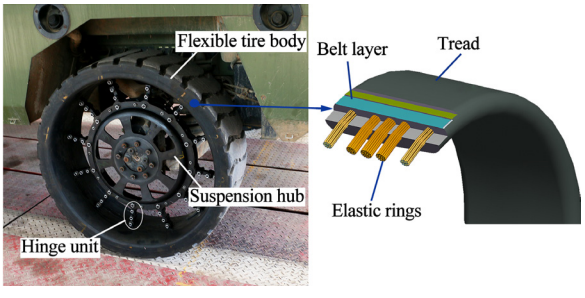

Fig. 1. *Main structure composition of ME wheel*

According to the physical dimension of the ME wheel, a 37×12.5R16.5 type inflatable tire with a similar outer diameter and width was selected as a comparative reference tire for the grounding characteristics of the ME wheel, as shown in Fig. 2. The main physical dimensions of the ME wheel and the reference inflatable tire are shown in Table 1.

Fig. 2. *Reference inflatable tire*

Table 1. *Comparison of key geometric parameters between the ME wheel and inflatable tire*

Tire type	Overall diameter [mm]	Tread width [mm]	Rim diameter [mm]	Aspect ratio
ME wheel	943.5	312.0	-	-
Inflatable tire	939.8	317.5	419.1	0.82

2 NUMERICAL SIMULATION MODELLING

2.1 ME Wheel Model

FE analysis discretizes the continuous geometric structure into finite elements and sets finite nodes in each element; thus, the continuum is discretized into a set of elements connected by nodes. The FE method has been an essential part of tire research, and various mechanical properties of the tire can be analysed according to different material properties, geometric contours, loads and boundary conditions [28] and [29].

The flexible tire body of a ME wheel contains multiple layers of cord-rubber composites with different mechanical properties, and the materials constituting ME wheel mainly include rubber, fibre cord, alloy steel and spring steel. Since rubber is a hyper-elastic material with a nearly incompressible volume, the Mooney-Rivlin constitutive model was utilized to describe the behaviour of it. The determination of the material parameters for the ME wheel was displayed in reference [30].

The three-dimensional (3D) FE model of the ME wheel, established by ABAQUS, was shown in Fig. 3. In the modelling process, the structure of the ME wheel was simplified properly on the premise of ensuring the reliability of the results, such as removing some edges and corners of the wheel and ignoring the influence of tread patterns. The rubber layer of the ME wheel was meshed with an 8-node linear brick, reduced integration unit C3D8R, and the elastic rings embedded in the flexible tire body were modelled using linear beam unit B31. The rebar model is that the reinforcement and the base are respectively represented by the rebar element and solid element, and it can express the base and the stiffener in different constitutive relations [31]. When modelling the cord-rubber composites, the rebar model was utilized, and the cord-rubber composites were decomposed into the rubber base part and cord reinforcement part. Other components of the ME wheel, such as suspension hub and hinges, were also simulated with C3D8R [32].

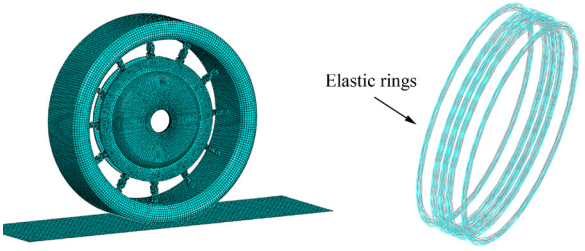

Fig. 3. *FE model of ME wheel*

The hinges and other parts of the wheel were connected by nodes, and a hinge connector was adapted to simulate the rotation of the mechanism. The contact definition between wheel components was defined as general contact, and the contact type between wheel and road surface was defined as surface-to-surface contact. The friction coefficient between the tread and road was assumed to be 0.6. The selection of mesh parameters needs to be of good accuracy and still have high computational efficiency. Under initial boundary condition, a fixed constraint was imposed on the road, and then steady-state transport analysis was used to perform numerical calculations.

2.2 Inflatable Tire Model

The structural characteristics of the inflatable tire are similar to those of the flexible tire body of the ME wheel. As the relative motion between the rim and the bead is small during the rolling process of the inflatable tire, the contact problem between the tire bead and the rim was simplified by limiting the degree of freedom (DOF) of the elements near the rim when the inflatable tire was modelled with the FE method.

As displayed in Fig. 4a, the two-dimensional (2D) axisymmetric FE model of the inflatable tire was established by ABAQUS, and then the 3D FE model of the tire was generated by rotating the 2D section model. The triangular elements and the quadrilateral elements of the rubber material were simulated by the linear axisymmetric hybrid element CGAX3H and the bilinear axisymmetric hybrid element CGAX4H. The

cord was modelled by linear axisymmetric element SFMGAX1. Additionally, to improve the calculation efficiency and obtain more accurate simulation results, mesh refinement was carried out near the contact patch when the 3D FE model of the inflatable tire was generated, as shown in Fig. 4b. The material parameters required for the modelling of tire referred to the data in [33], and the completed tire model consists of 62,328 elements and 69,521 nodes.

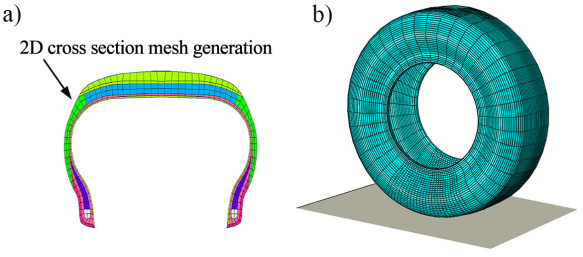

Fig. 4. *a) 2D cross-section; b) 3D FEM model of inflatable tire*

3 FE MODEL VALIDATION

3.1 Stiffness Test

It is necessary to verify the accuracy and reliability of the tire FE model before virtual simulation experiments are carried out. The vertical stiffness, longitudinal stiffness, and lateral stiffness of the ME wheel [33] were tested by a tire test rig, as shown in Fig. 5.

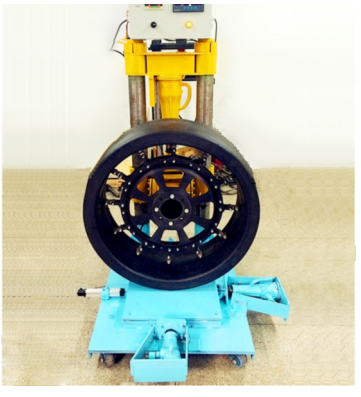

Fig. 5. *Stiffness test of the ME wheel*

The vertical stiffness of the tire has a significant influence on the bearing capacity, vibration and ride comfort of the vehicle. Fig. 6 shows the simulation and test data of wheel deflection under different vertical loads. It is easy to see that the deflection almost increases in line with the increase of the vertical load when the load is small, but as the vertical load increases, the increasing trend of wheel deflection decreases gradually. Moreover, the simulation data and test data are in good agreement.

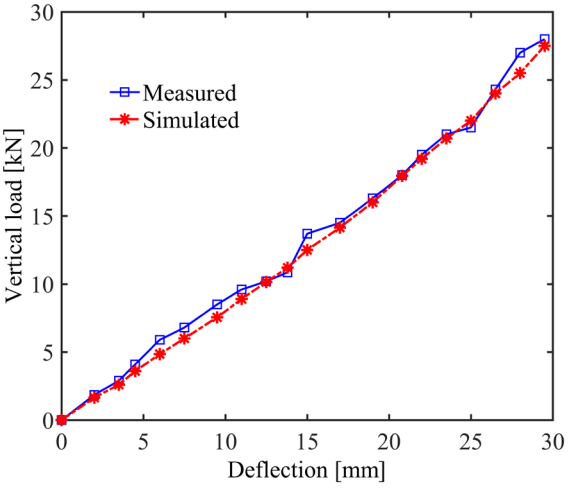

Fig. 6. *The relationship between the vertical load and deflection*

In Fig. 7, the simulation results of the longitudinal and lateral stiffness characteristics of the ME wheel are compared with the test results when the vertical load F_Z is 9.5 kN and 15 kN, respectively. It shows that the predicted variation characteristics of the longitudinal displacement and lateral displacement of the ME wheel are essentially consistent with the experimental data.

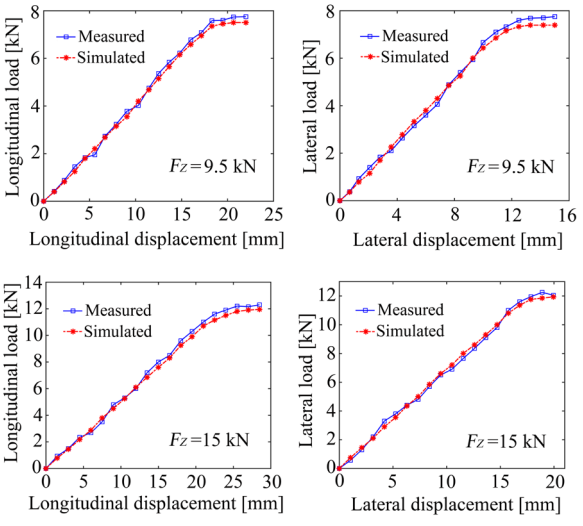

Fig. 7. *Simulation and test data of the longitudinal and lateral stiffness characteristics under different loads*

Table 2 shows the average relative error statistics for the vertical stiffness, longitudinal stiffness and lateral stiffness of the ME wheel. From the data in the

table, it is observed that the average relative errors between the test and simulation values are about 5 %. Therefore, combining the above-mentioned comparative analysis, the following conclusions can be obtained: the numerical simulation model of the ME wheel has fine reliability and accuracy; therefore, it can be used for the subsequent virtual experiment simulation of the wheel's mechanical characteristics under different working conditions.

Table 2. *Average relative error statistics of simulation results*

Stiffness type	Average relative error [%]	
	F_Z = 9.5 kN	F_Z = 15.5 kN
Vertical stiffness	5.12	5.12
Longitudinal stiffness	4.02	4.41
Lateral stiffness	5.28	5.02

3.2 Inflatable Profile and Load Characteristics Test

To verify the accuracy of the FE model of the inflatable tire, the simulation results, including the inflated contour size of the inflatable tire and the relationship between the load and deflection, were compared with the experimental results.

The simulation values and measured values of section width and outer perimeter of the inflatable tire under two different inflation pressure conditions are displayed in Table 3, and the maximum relative error was 1.25 %.

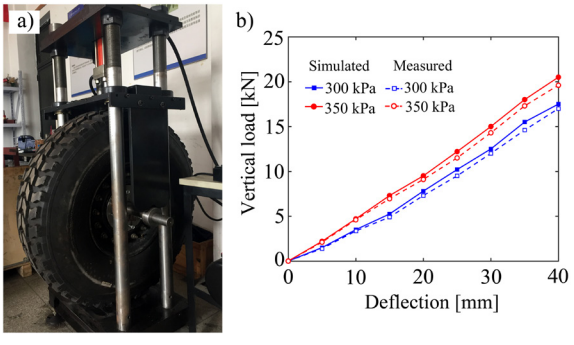

Fig. 8. *a) Load characteristics test; b) comparison between test and simulation data*

As displayed in Fig. 8, the load characteristics tests of the inflatable tire under two different inflation pressures (300 kPa and 350 kPa) were carried out on a vertical loading test rig. It can be seen from Fig. 8b that the test curve of the inflatable tire has a high degree of coincidence with the simulation curve, and the average errors are 3.8 % and 4.3 %, respectively. Consequently, the established FE model of the inflatable tire has high accuracy, and the result of the virtual simulation test is reliable.

4 DETERMINATION OF ROLLING RADIUS

When the tire is rolling at the same translational velocity, different angular velocities correspond to three different rolling states: free rolling, braking, and driving. It is necessary to specify the angular velocity of the tire and the translational velocity of the road surface separately when simulating the steady-state rolling of the tire. Since free rolling is a critical state between braking and driving, the rolling angular velocity and rolling radius of the tire under the free-rolling condition should, therefore, be determined before the steady-state rolling simulation analysis of the tire was carried out. When the tire is in the free-rolling state, the sideslip angle, the camber angle, and the longitudinal force are zero, and the actual radius is the free-rolling radius of the tire.

To determine the free-rolling angular velocity of the tire under a certain load and speed condition, the tire's translational velocity was first divided by an estimated rolling radius, and then an approximate range of the free-rolling angular velocity can be obtained. Under the condition that the tire's translational velocity was kept constant, the longitudinal forces corresponding to different angular velocities within the estimated range were calculated. When the longitudinal force was zero, the corresponding rolling angular velocity was the free-rolling angular velocity of the tire.

Taking the inflatable tire studied in this paper as an example, the free radius is approximately 469.9 mm, and the static radius is 450.08 mm with a tire pressure of 350 kPa and a vertical load of 8000 N. The free-rolling radius should be between the free radius and the static radius, assuming that it is 460 mm, and then the corresponding rolling angular velocity is

Table 3. *Inflated contour size of the inflatable tire*

Inflation pressure [kPa]	Section width [mm]		Relative error [%]	Outer perimeter [mm]		Relative error [%]
	Simulated	Measured		Simulated	Measured	
300	315.22	319	1.18	2953.65	2991	1.25
350	318.56	322	1.06	2986.28	3018	1.05

6.038 rad/s when the translational velocity is 10 km/h. Therefore, the angular velocity range can be set to 5.8 rad/s to 6.2 rad/s, and then the relationship curve between angular velocity and longitudinal force in this interval can be obtained through simulation analysis, as shown in Fig. 9. It can be seen that the angular velocity is 5.97 rad/s when the longitudinal force is 0 kN, and the corresponding free-rolling radius is 465.28 mm. The same method can be used to calculate the free-rolling angular velocity of the ME wheel with a vertical load of 8000 N and a translational velocity of 10 km/h. Finally, the calculated free-rolling angular velocity is 5.96 rad/s, and the corresponding free-rolling radius of the ME wheel is 466.32 mm.

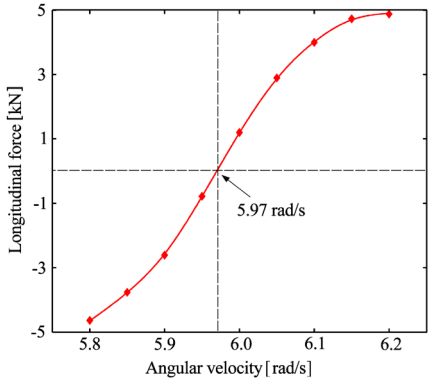

Fig. 9. *Relationship between longitudinal force and angular velocity of inflatable tire*

5 RESULTS AND DISCUSSION

In order to analyse the pressure distribution characteristics in the contact patch of the ME wheel and inflatable tire, as shown in Fig. 10, five sets of path nodes parallel to each other along the length of the ground contact imprint were established on the tread surface of ME wheel and inflatable tire. Each path consists of 17 nodes, of which the path 3 passes through the centre line of the tread surface, and the other four paths are symmetrically distributed on the upper and lower ends of the ground imprint.

5.1 Free-Rolling Condition

To investigate the influence of the camber angle on the ground pressure distribution under the free-rolling condition, the ME wheel or inflatable tire was maintained in a free-rolling state, and the road was rotated along the wheel's motion direction by a certain angle, which was the camber angle for the simulation analysis. When the vertical load was 8 kN, and the translational velocity was 10 km/h, the grounding characteristics of the ME wheel and inflatable tire were analysed. Fig. 11 displays the comparison of the 3D contact pressure distribution curves of the ME wheel and inflatable tire (inflation pressure 350 kPa) when the camber angle γ was 2°, 4°, 6°, and 12°, respectively.

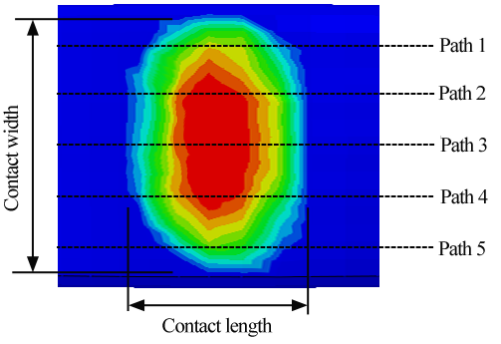

Fig. 10. *The location sketch of the selected node sets along the length of the ground imprint*

Comparing the variation of the contact pressure curves in Fig. 11, it can be seen clearly that the contact pressure is basically symmetrical with respect to the centreline along the width of the ground imprint. As the camber angle increases, the contact pressure of both the ME wheel and the inflatable tire will gradually concentrate on the side of the tread surface. In addition, the ground contact area becomes smaller, and the uniformity of the pressure distribution becomes worse with the increase of the camber angle. Both the ME wheel and the inflatable tire will suffer the partial wear of the tread surface.

Horizontal comparison of the ground pressure of the ME wheel and inflatable tire at the same camber angle was performed. As displayed in Fig. 11, when the camber angle is 2°, the maximum ground pressure of the ME wheel is distributed in the central area of the contact patch and the pressure decreases gradually from the centre to both sides, while the ground pressure of the inflatable tire at the centre of the contact patch is smaller than that of both sides, showing a similar saddle-shaped pressure distribution characteristic. When the camber angle is 4°, the maximum ground pressure of both ME wheel and inflatable tire moves to the roll side, but the moving speed of the maximum pressure of the inflatable tire is obviously higher than the maximum pressure of the ME wheel. At this point, the uniformity of the ground pressure of the ME wheel is slightly better than that of the inflatable tire. When the camber angle rises to 6°, the maximum ground pressure position of both tires is

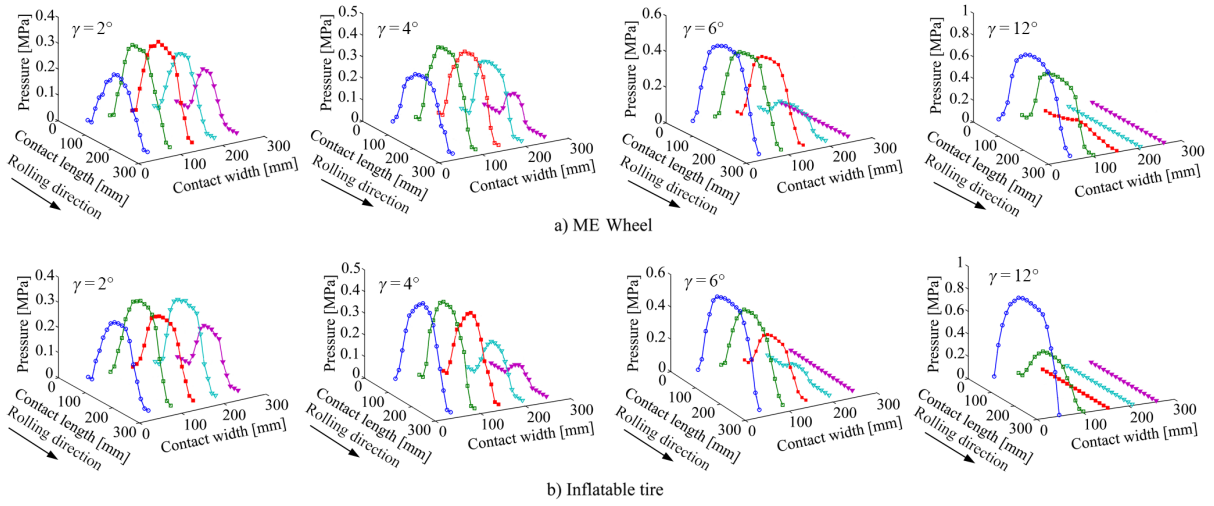

Fig. 11. *Pressure distribution in free-rolling condition with different camber angles*

located at the outermost side of the tire tilt direction. As the camber angle increases, the outermost ground pressure continues to increase, and the uniformity of the pressure distribution further deteriorates. When the camber angle reaches 12°, the ground pressure of the ME wheel and the inflatable tire is almost all concentrated on one side of the shoulder, but the pressure concentration of the inflatable tire is more serious at this time, and the partial wear of the tread will be aggravated.

Table 4 shows the comparison data of the predicted maximum contact pressure of the ME wheel and the inflatable tire under free-rolling conditions. It is observed that the maximum contact pressure of the ME wheel is slightly less than that of the inflatable tire at the same camber angle. Moreover, the growth trend of the maximum contact pressure of both ME wheel and inflatable tire is gradually accelerating as the camber angle increases.

Table 4. *Predicted maximum contact pressure of the ME wheel and inflatable tire in free free-rolling condition*

γ [°]	Maximum contact pressure [MPa]	
	ME wheel	Inflatable tire
2	0.362	0.383
4	0.391	0.425
6	0.464	0.503
12	0.765	0.871

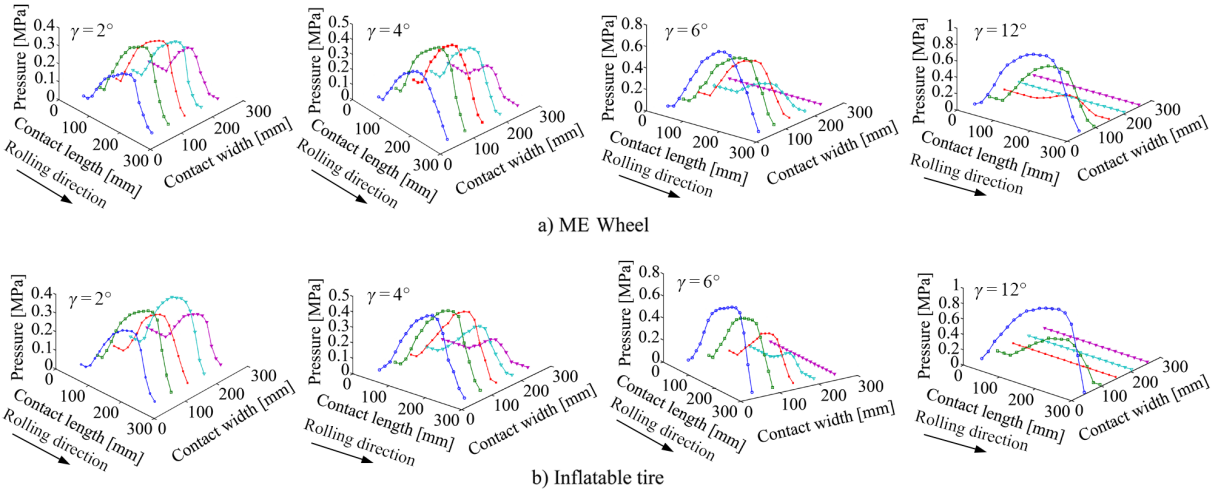

Fig. 12. *Pressure distribution in braking condition with different camber angles*

5.2 Braking Condition

Under braking conditions, different rolling angular velocities will lead to different slip states. The slip ratio formula is defined as:

$$s = (u_x - R_e w) / u_x, \tag{1}$$

where s is the slip ratio of the tire, u_x is translational velocity, R_e is the rolling radius, and w is the angular velocity. When the translational velocity of the ME wheel and inflatable tire was set to 10 km/h and the rolling angular velocity was set to 5.48 rad/s and 5.50 rad/s respectively, the braking slip ratio of both tires was 8 %.

Fig. 12 shows the ground pressure curves of these two tires with a slip ratio of 8 % and a camber angle of 2°, 4°, 6°, and 12°, respectively. By comparing the distribution characteristics of the pressure curves, it is easily observed that the influence of the camber angle on the ground pressure of the two tires is similar to that of the free-rolling state under the braking condition, and the ground pressure is concentrated toward the shoulder portion of the tire roll side, resulting in uneven wear of the tread. However, unlike the free-rolling state, the ground pressure in the braking state is no longer symmetrical about the central line along the width of the ground imprint, and the high ground pressure zone is gradually shifted to the front part of the tire movement direction.

Table 5 shows the maximum contact pressure of the ME wheel and inflatable tire in braking conditions. It can be seen that the variation trend of the maximum pressure value is similar to that of the free-rolling condition, but the maximum pressure under the braking condition is larger than that under the free-rolling condition when the camber angle is the same.

Table 5. *Predicted maximum contact pressure of the ME wheel and inflatable tire in braking condition*

γ [°]	Maximum contact pressure [MPa]	
	ME wheel	Inflatable tire
2	0.360	0.379
4	0.449	0.465
6	0.651	0.683
12	0.835	0.972

5.3 Driving Condition

When the rolling angular velocity of the tire is greater than the free-rolling angular velocity, the longitudinal force generated between the tire and the road surface will push the tire forward, at which time the tire is in the driving condition. To analyse the influence of the slip ratio on the ground pressure, the pressure distribution characteristics of the ME wheel and the inflatable tire at different slip ratios were analysed.

Fig. 13 shows the 3D ground pressure characteristic curves of the ME wheel and inflatable

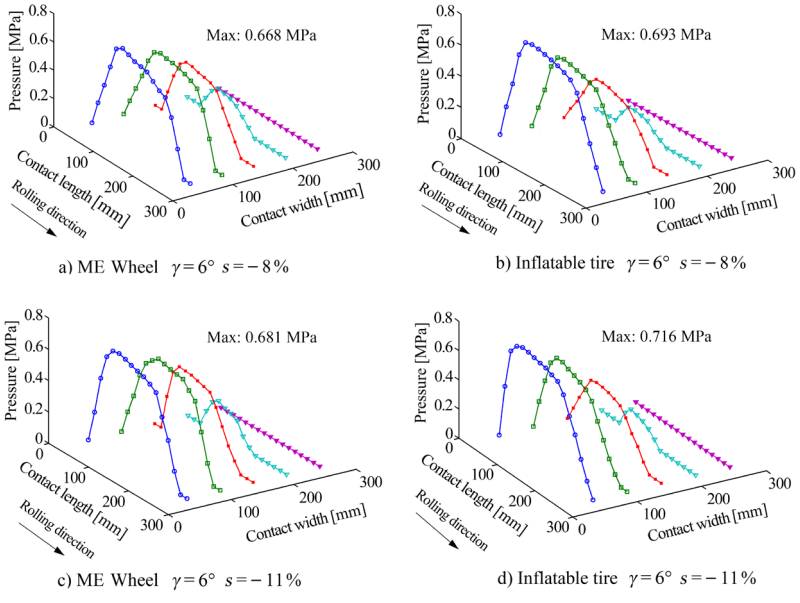

Fig. 13. *Pressure distribution in driving condition*

tire at the slip ratio of –8 % and –11 % when the camber angle is 6°. It can be seen that the pressure distribution of the ME wheel and the inflatable tire in the driving condition is also no longer symmetrical about the centreline along the width of the ground mark; however, the moving direction of the high-pressure zone is opposite to that in the braking condition, and is offset to the back end of the contact area. As seen clearly, for the slip ratio of –8 %, the maximum ground pressure of the ME wheel and the inflatable tire is 0.668 MPa and 0.693 MPa, respectively, and when the slip ratio increases to –11 %, the maximum pressure values of these two tires are 0.681 MPa and 0.716 MPa, respectively. Consequently, it can be concluded that the maximum pressure value of the contact patch increases as the slip ratio increases when the camber angle remains constant.

6 CONCLUSIONS

The grounding characteristics of the ME wheel with a camber angle in free-rolling, braking and driving conditions were studied by finite element analysis and bench tests in this paper, and the simulation results of grounding characteristics for the ME wheel and inflatable tire under the same rolling conditions were compared and analysed. The main conclusions were summarized as follows:

1. The ground pressure of the ME wheel is substantially symmetrical about the centre line along the width direction of the grounding mark in free-rolling condition. Meanwhile, as the camber angle increases, the ground pressure of the ME wheel and inflatable tire will be concentrated toward the roll side, and the uniformity of the pressure distribution gradually deteriorates; therefore, both the ME wheel and inflatable tire will suffer the partial wear of the tread.
2. The moving speed of maximum ground pressure of the ME wheel is significantly less than that of the inflatable tire in free-rolling condition, which results in the pressure concentration of the inflatable tire being more serious than the ME wheel when the camber angle is large, and the resulting tread wear is also aggravated.
3. Under braking condition, the effect of the camber angle on the pressure distribution of the ME wheel is similar to that in free-rolling condition, however, the ground pressure of the ME wheel in braking state is no longer symmetrical with respect to the centre line along the width of the grounding imprint, and the high-pressure zone gradually shifts to the front of the moving direction.
4. The moving direction of the high-pressure zone of the ME wheel in the driving condition is opposite to that in the braking condition, offsetting the rear end of the contact patch. In addition, the maximum pressure of the contact patch increases with the increase of slip ratio when the camber angle remains unchanged.

7 ACKNOWLEDGEMENTS

This work was supported by the Scientific Exploration Fund of the General Armament Department of China (No. NHA13002), the Funding of the Jiangsu Innovation Program for Graduate Education (No. KYLX15_0254) and the Scientific Research Foundation of Shandong University of Science and Technology for Recruited Talents.

8 REFERENCES

[1] Baranowski, P., Malachowski, J., Mazurkiewicz, L. (2016). Numerical and experimental testing of vehicle tyre under impulse loading conditions. *International Journal of Mechanical Sciences*, vol. 106, p. 346-356, **DOI:10.1016/j.ijmecsci.2015.12.028**.

[2] Cho, J.R., Lee, J.H., Jeong, K.M., Kim, K.W. (2012). Optimum design of run-flat tire insert rubber by genetic algorithm. *Finite Element in Analysis and Design*, vol. 52, p. 60-70, **DOI:10.1016/j.finel.2011.12.006**.

[3] Zhao, Y.Q., Zang, L.G., Chen, Y.Q., Li, B., Wang, J. (2015). Non-pneumatic mechanical elastic wheel natural dynamic characteristics and influencing factors. *Journal of Central South University*, vol. 22, no. 5, p. 1707-1715, **DOI:10.1007/s11771-015-2689-1**.

[4] Jin, X.C., Hou, C., Fan, X.L., Sun, Y.L., Lv, J., Lu, C.S. (2018). Investigation on the static and dynamic behaviors of non-pneumatic tires with honeycomb spokes. *Composite Structures*, vol. 187, p. 27-35, **DOI:10.1016/j.compstruct.2017.12.044**.

[5] Kucewicz, M., Baranowski, P., Malachowski, J. (2016). Airless tire conceptions modeling and simulations. *Proceedings of the 13th International Scientific Conference: Computer Aided Engineering*, p. 293-301, **DOI:10.1007/978-3-319-50938**.

[6] Ju, J., Veeramurthy, M., Summers, J.D., Thompso, L. (2013). Rolling resistance of a non-pneumatic tire having a porous elastomer composite shear band. *Tire Science and Technology*, vol. 41, no. 3, p. 154-173, **DOI:10.2346/tire.13.410303**.

[7] Jang, I.G., Sung, Y.H., Yoo, E.J., Kwak, B.M. (2012). Pattern design of a non-pneumatic tire for stiffness using topology optimization. *Engineering Optimization*, vol. 44, no. 2, p. 119-131, **DOI:10.1080/0305215x.2011.569546**.

[8] Narasimhan, A., Ziegert, J., Thompson, L. (2011). Effects of material properties on static load-deflection and vibration of

a non-pneumatic tire during high-speed rolling. *SAE Technical Paper*, no. 2011-01-0101, **DOI:10.4271/2011-01-0101**.

[9] Ma, J.F., Kolla, A., Summers, J.D., Joseph, P.F., Blouin, V.Y., Biggers, S. (2009). Numerical simulation of new generation non-pneumatic tire (TWEELTM) and sand. *Proceedings of the ASME International Design Engineering Technical Conferences and Computers and Information in Engineering Conference*, p. 123-130, **DOI:10.1115/detc2009-87263**.

[10] Kim, K., Kim, D.M.(2011). Contact pressure of non-pneumatic tires with hexagonal lattice spokes. *SAE Technical Paper*, no. 2011-01-0099, **DOI:10.4271/2011-01-0099**.

[11] Du, X.B., Zhao, Y.Q., Wang, Q., Fu, H.X. (2017). Numerical analysis of the dynamic interaction between a non-pneumatic mechanical elastic wheel and soil containing an obstacle. *Proceedings of the Institution of Mechanical Engineers, Part D: Journal of Automobile Engineering*, vol. 231, no. 6, p. 731-742, **DOI:10.1177/0954407016660946**.

[12] Xiao, Z., Zhao, Y.Q., Lin, F., Zhu, M.M., Deng, Y.J. (2018). Studying the fatigue life of a non-pneumatic wheel by using finite-life design for life prediction. *Strojniški vestnik - Journal of Mechanical Engineering*, vol. 64, no. 1, p. 56-67, **DOI:10.554 5/sv-jme.2017.4695**.

[13] Nakajima, Y. (2007). Application of optimisation technique to tire design. International Journal of Vehicle Design, vol. 43, no. 1-4, p. 49-65, **DOI:10.1504/ijvd.2007.012295**.

[14] Veeramurthy, M., Ju, J., Thompson, L., Summers, J.D. (2014). Optimisation of geometry and material properties of a non-pneumatic tyre for reducing rolling resistance. *International Journal of Vehicle Design*, vol. 66, no. 2, p. 193-216, **DOI:10.1504/ijvd.2014.064567**.

[15] Lee, J., Wang, S., Pluymers, B., Kindt, P. (2015). A modified complex modal testing technique for a rotating tire with a flexible ring model. *Mechanical Systems and Signal Processing*, vol. 60-61, p. 604-618, **DOI:10.1016/j.ymssp.2014.12.002**.

[16] Hoever, C., Kropp, W. (2015). A model for investigating the influence of road surface texture and tyre tread pattern on rolling resistance. *Journal of Sound and Vibration*, vol. 351, p. 161-176, **DOI:10.1016/j.jsv.2015.04.009**.

[17] Baranowski, P., Malachowski, J. (2015). Numerical study of selected military vehicle chassis subjected to blast loading in terms of tire strength improving. *Bulletin of Polish Academy of Sciences-Technical Sciences*, vol. 63, no. 4, p. 867-878, **DOI:10.1515/bpasts-2015-0099**.

[18] Song, H.S., Jung, S.P., Park, T.W. (2018). Simulation of temperature rise within a rolling tire by using FE analysis. *Journal of Mechnical Science and Technology*, vol. 32, no. 7, p. 3419-3425, **DOI:10.1007/s12206-018-0645-3**.

[19] Nishiyama, K., Nakashima, H., Yoshida, T., Shimizu, H., Miyasaka, J., Ohdoi, K. (2018). FE-DEM with interchangeable modeling for off-road tire traction analysis. *Journal of Terramechanics*, vol. 78, p. 15-25, **DOI:10.1016/j.jterra.2018.03.005**.

[20] Han, D., Zhu, G.D., Hu, H.M., Li, L.L. (2018). Dynamic simulation analysis of the tire-pavement system considering temperature fields. *Construction and Building Materials*, vol. 171, p. 261-272, **DOI:10.1016/j.conbuildmat.2018.03.071**.

[21] Tamada, R., Shiraishi, M. (2017). Prediction of uneven tire wear using wear process simulation. *Tire Science and Technology*, vol. 45, no. 2, p. 87-100, **DOI:10.2346/tire.17.450201**.

[22] Wei, Y.T., Feng, X.J., Zhou, F.Q., Xiang, D.B. (2016). Simulation of rolling noise based on the mixed Lagrangian-Eulerian method. *Tire Science and Technology*, vol. 44, no. 1, p. 36-50, **DOI:10.2346/tire.16.440103**.

[23] Wei, Y.T., Oertel, C., Shen, X.L. (2012). Tyre rolling kinematics and prediction of tyre forces and moments: Part II – simulation and experiment. *Vehicle System Dynamics*, vol. 50, no. 11, p. 1689-1706, **DOI:10.1080/00423114.2012.694453**.

[24] Anderson, J.R., McPillan, E. (2016). Simulation of the wear and handling performance trade-off by using multi-objective optimization and TameTire. *Tire Science and Technology*, vol. 44, no. 4, p. 280-290, **DOI:10.2346/tire.16.440404**.

[25] Wozniak, R., Taryma, S., Mioduszewski, P. (2015). Tire camber angle influence on tire-pavement noise. *Noise Control Engineering Journal*, vol. 63, no. 3, p. 216-224, **DOI:10.3397/1/376320**.

[26] Kagami, S., Akasaka, T., Shiobara, H., Hasegawa, A. (1995). Analysis of the contact deformation of a radial tire with camber angle. *Tire Science and Technology*, vol. 23, no. 1, p. 26-51, **DOI:10.234 6/1.2137494**.

[27] El-Gawwad, K.A.A., Crolla, D.A., Soliman, A.M.A., El-Sayed, F.M. (1999). Off-road tyre modelling II: effect of camber on tyre performance. *Journal of Terramechanics*, vol. 36, no. 1, p. 25-38, **DOI:10.1016/s0022-4898(98)00032-9**.

[28] Baranowski, P., Malachowski, J., Janiszewski, J., Wekezer, J. (2016). Detailed tyre FE modeling with multistage validation for dynamic analysis. *Materials and Design*, vol. 96, p. 68-79, **DOI:10.1016/j.matdes.2016.02029**.

[29] Guo, H., Bastien, C., Blundell, M., Wood, G. (2014). Development of a detailed aircraft tyre finite element model for safety assessment. *Materials and Design*, vol. 53, p. 902-909, **DOI:10.1016/j.matdes.2013.05.046**.

[30] Du, X.B., Zhao, Y.Q., Lin, F., Xiao, Z. (2017). Parameters determination of Mooney-Rivlin model for rubber material of mechanical elastic wheel. *Applied Mechanics and Materials*, vol. 872, p. 198-203, **DOI:10.4028/www.scientific.net/amm.872.198**.

[31] Wang, H., Al-Qadi, I.L., Stanciulescu, I. (2014). Effect of surface friction on tire-pavement contact stresses during vehicle maneuvering. *Journal of Engineering Mechanics*, vol. 140, no. 10, p. 04014001, **DOI:10.1061/(ASCE)EM.1943-7889.0000691**.

[32] Zhao, Y.Q., Du, X.B., Lin, F., Wang, Q., Fu, H.X. (2018). Static stiffness characteristics of a new non-pneumatic tire with different hinge structure and distribution. *Journal of Mechanical Science and Technology*, vol. 32, no. 7, p. 3057-3064, **DOI:10.1007/s12206-018-0608-8**.

[33] Guan, Y.J., Zhao, G.Q., Cheng, G. (2006). Influence of belt cord angle on radial tire under different rolling states. *Journal of Reinforced Plastics and Composites*, vol. 25, no. 10, p. 1059-1077, **DOI:10.1177/0731684406065000**.

Strojniški vestnik - Journal of Mechanical Engineering 65(2019)5, 297-310

DOI:10.5545/sv-jme.2018.5937 Original Scientific Paper
Received for review: 2018-12-18
Received revised form: 2019-03-22
Accepted for publication: 2019-05-07

Innovative Design of a Vertical and Transverse Elevator in Double Shafts, Based on TRIZ Theory

Jiwen Chen[1,2,*] – Xin Li[1,2] – Hongjuan Yang[3] – Chen Wang[1,2]

[1]Shandong Jianzhu University, Co-Innovation Center for Green Building of Shandong Province, China
[2]Shandong Jianzhu University, School of Mechanical and Electronic Engineering, China
[3]Shandong Jianzhu University, School of Information and Electrical Engineering, China

With the rapid growth of urban populations, the scale of modern buildings is expanding, and the span of buildings is increasing. Traditional elevators can only solve the problem of vertical transportation. Passengers still need to spend time walking to their destination after leaving the elevator. Based on the theory of inventive problem solving (TRIZ), this paper uses functional models, causal analysis, conflict analysis, the Su-Field model, and other tools to innovate on the basis of traditional elevators. A vertical and transverse elevator design proposal for double shafts structures and corresponding control strategies is proposed. Based on C#, simulations of the effect of the vertical and transverse elevator on the passenger mobility efficiency are conducted in an 8-story building at different transverse distances and densities. The simulation results show that the vertical and transverse elevator can effectively improve the mobility efficiency of passengers in the horizontal direction in the studied environment, and the mobility efficiency of all passengers also significantly improves. As the transverse distance increases, the mobility efficiency of all passengers using the proposed elevator also increases.

Keywords: TRIZ, Su-Field model, transverse elevator, Poisson distribution, elevator passengers' flow model

Highlights

- *The vertical and horizontal operation of the elevator is solved based on TRIZ theory.*
- *Vertical and horizontal passenger flow models are generated based on the Poisson distribution and Monte Carlo method.*
- *The efficiency of the vertical and transverse elevator in an 8-story building is verified with a simulation platform designed with C#.*
- *The vertical and transverse elevator can effectively improve the mobility efficiency of passengers in the horizontal direction in the studied environment.*

0 INTRODUCTION

Product innovation refers to the process of creating a new product or redesigning the function of a product [1]. To help engineers quickly generate innovative ideas to complete complex designs, many innovative methods have emerged. Commonly used innovative methods fall into two categories: intuitive methods and logical methods. Intuitive methods do not involve pre-analysis but produce innovative ideas by stimulating a dormant human thought process [2]. Because intuition is usually divergent, many detours generally occur. The logical method is based on the principles of science and engineering, and a large number of existing solutions must be analysed to systematically solve a problem. The theory of inventive problem solving (TRIZ) was proposed by Ahshuler, who analysed more than 2 million high-level patents worldwide and proposed the involving invention, creation and technological innovation based on the principles of multiple disciplines [3]. Because TRIZ theory is highly abstract and can be repeatedly applied in different fields to solve different problems, it is now widely used as a scientific theory.

Elevators, as vertical transport tools in buildings, can solve the problem of vertical passenger transport in high-rise buildings and have been increasingly widely used [4]. Elevators are indispensable in modern high-rise buildings and serve users with high efficiency and quality. With the rapid development of the economy and the rapid growth of the urban population, the scale of modern buildings is expanding, and the span of buildings is increasing [5]. Traditional elevators can only solve the problem of vertical transportation. Passengers still need to spend time walking to their destination after leaving the elevator. Because an elevator cannot move horizontally, it restricts the connections between different elevators with different shafts.

In 1996, the Otis Company first proposed the Odyssey™ elevator system, which uses transmission and traction drives in the vertical direction and a linear motor drive in the horizontal direction to achieve lateral elevator movement [6]. This system is mainly used to solve the transfer problems of elevators in different sections of high-rise buildings and can be applied to improve the mobility efficiency of passengers in large-span buildings. In [7], a rope-

*Corr. Author's Address: Shandong Jianzhu University, School of Mechanical and Electronic Engineering, Fengming Road Lingang Development Zone, Jinan, China, chenjiwen@sdjzu.edu.cn

free elevator system based on planar positioners was proposed as an innovative solution for vertical and horizontal elevator movement based on the use of coordinate planar positioners as the drive source. In [8], the concept of a three-dimensional elevator system was introduced in a super-large building. The proposed virtual three-dimensional elevator system assumed that an elevator car can run in three directions (but obviously not at the same time). In [9], the Thyssen-Krupp Company's multi-elevator system was introduced and released in 2014. The cyclic multicar elevator system driven by a linear motor allows the vertical and horizontal operation of an elevator by installing steering devices at the nodes.

Although [6] to [9] effectively developed elevators that can achieve horizontal movement, due to technical or cost problems, these have not been effectively promoted. Thus, in this letter, we use the innovative principle introduced with the TRIZ theory to design vertical and transverse elevators in double shafts with low cost and broad applicability. To improve the passenger transport efficiency between distant shafts, a control strategy for an elevator with this structure is proposed and verified.

1 TRIZ METHODS

TRIZ provides a multifaceted approach to problem-solving and invention by treating the problem as a system and then trying to solve the related contradictions [10]. TRIZ includes a set of tools and methods for analysing and solving problems. The analysis tools are mainly used for the establishment, analysis and transformation of problem models, including causal analysis, Su-Field model analysis, conflict analysis, functional models as well as the algorithm for inventive problem solving (ARIZ) [11]. The problem-solving tools include inventive principles and scientific effect libraries [12]. These tools are developed by analysing a large number of high-quality patents and learning from existing innovative experiences [13]. When applying TRIZ theory to solve practical engineering problems, first, it is necessary to effectively describe the problems, transform specific engineering problems into general TRIZ problems, and establish a TRIZ problem model [14]. Then, a suitable TRIZ tool is used to solve the problem model and obtain a general solution to the general problem. Finally, the specific solutions of engineering problems are obtained by mapping and comparison, and the solutions are verified and evaluated. When solving an engineering problem, we may use a tool or even multiple TRIZ tools.

Functional models can simplify the structure of technical systems and help engineers understand the interactions among components in technical systems in detail so that a few changes to the system can solve the system problems [15]. By analysing the functional models, we can specify the system function problems and determine the root causes of the problems through causal analysis. Using Su-Field model analysis, the nature of a problem can be determined by the type of problem described and then, referring to the transformation rules and 76 standard solutions of the Su-Field model, design ideas can be provided for designers [16].

In solving engineering problems, the most effective solution is to solve the contradictions in technical problems [17]. The understanding of contradictions and solutions to contradictions are very important concepts in TRIZ theory. In TRIZ, contradictions are divided into technical contradictions and physical contradictions. When improving one characteristic or parameter in a technical system, the contradiction that causes the deterioration of another characteristic or parameter in the system is called a technical contradiction [18]. A physical contradiction is a contradiction of the system itself. Thus, subsystems often have opposite requirements, and systems usually have only one contradiction parameter [19]. A physical contradiction often exists within a technical contradiction. A contradiction matrix is an important tool for solving technical contradiction problems. This matrix organically links 39 general engineering parameters with 40 inventive principles of TRIZ and establishes the corresponding relations. When dealing with technical contradictions, the problem is described

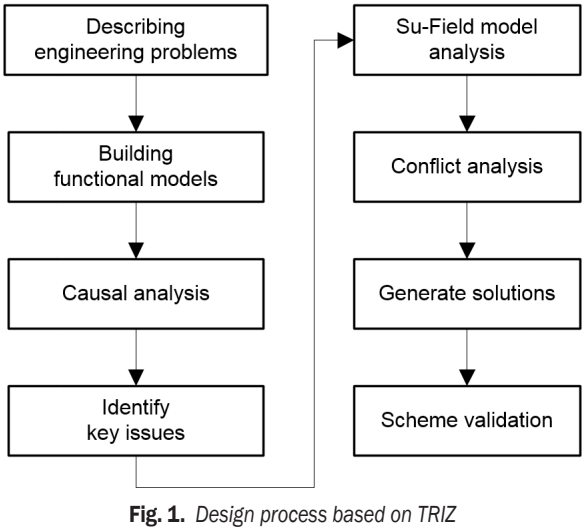

Fig. 1. *Design process based on TRIZ*

as a conflict between any two of the 39 parameters [20]. The problem is solved by finding the inventive principle in the contradiction matrix. When dealing with physical contradictions, the separation principles can be used to solve problems.

The flow chart of solving the elevator horizontal movement problem is shown in Fig. 1. The key problems that must be solved are identified by functional models and causal analysis. The analysis and transformation problems are solved using the Su-Field model. Contradiction analysis is used to solve the problem and generate the solution. Then, the feasibility of the solution is verified by simulation experiments.

2 DESIGN PROCESS

2.1 Functional Models

Functional models describe the functions of technical and hyper-technical system components, as well as useful functions, performance levels, and cost levels [21]. In functional models, functions can be divided into useful functions and harmful functions. Useful functions include basic functions, auxiliary functions, and additional functions [22]. The performance level of a function is normal, excessive, insufficient or harmful. The graphical symbols are shown in Fig. 2.

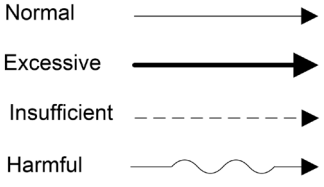

Fig. 2. *Symbols of the performance levels of functions*

Elevators are vertical transportation devices installed in building shafts that are mainly composed of a traction system, a guiding system, a door system, a weight balance system, and a safety protection system. The elevator core components, including the traction system, guidance system, and weight balance system, are selected for analysis. Then, the functions of the above components are summarized, and the function registration and performance level features are determined. The elevator system function model can then be established, as shown in Fig. 3.

By analysing the functional models, we find that there are two reasons that an elevator cannot move horizontally: 1. the elevator traction system cannot drive the car horizontally, and 2. the guiding device has a specific orientation to the car. To further explore the main causes of the problem, a causal analysis was performed for the above problem.

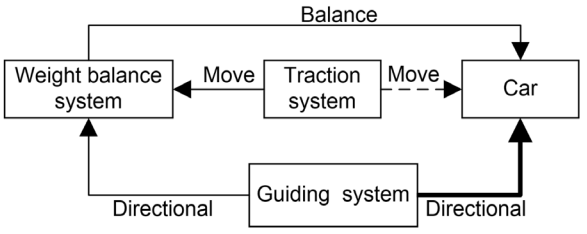

Fig. 3. *Function model of an elevator*

2.2 Causal Analysis

Causal analysis is a method of studying the relationship between development-based results and the causes of these results [23]. Starting from the problems that exist in a system, the causes of these phenomena are sequentially analysed, and the factors affecting the causality are analysed [24]. This paper chooses causal chain analysis starting from the problems to be solved, lists the direct causes of the problems, and uses these reasons as the results. Then, we search for the causes of these results and repeat the steps above until the root causes are found. Each cause and result are connected with arrows, and the arrow direction points from the cause to the result. When there are multiple causes of the problem, they are connected by "and" (multiple causes lead to results only if they exist at the same time) or "or" (multiple causes lead to results if only one exists). The causal chain model of a car that cannot move horizontally is shown in Fig. 4.

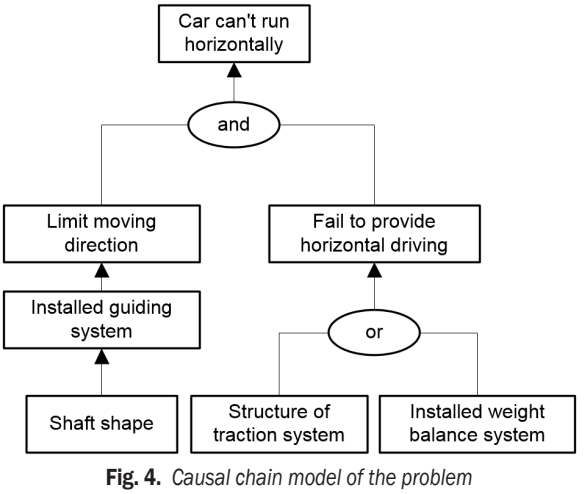

Fig. 4. *Causal chain model of the problem*

The causal chain model shows that the main reasons that the car cannot move horizontally are as

follows: 1. the shaft shape is columnar and there is no space for horizontal movement, and 2. the structure of the traction system or the installed weight balance system does not allow the traction system to provide horizontal movement. After using causal analysis to find the root cause of the problem, the Su-Field model is used to model the problem, and the practical engineering problem is transformed into a general TRIZ problem.

2.3 Su-Field Model Analysis

The Su-Field model is the smallest complete system composed of two substances (S) and one field (F) [25]. The function of the system is expressed by the Su-Field triangle, which is composed of these three elements and clearly reflects the problems that exist in the system [26]. Typically, S1 acts as a recipient, S2 is the originator, and F is the interaction term. In the Su-Field model, the ideal state is F acting on S1 and changing S1 through S2 [27]. According to the theory of TRIZ, the Su-Field model of the minimal system of elevator car movement is constructed, and the relevant elements of the Su-Field model are determined as follows: S1 is the car; S2 is the traction system; and F1 is the mechanical force driving car movement, as shown in Fig. 5.

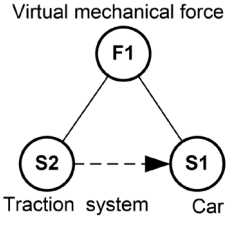

Fig. 5. *Su-Field model of the minimal system of elevator car movement*

According to TRIZ theory, the Su-Field model is analysed. The system is a complete Su-Field model with three complete elements. However, the car can only move in the vertical direction for transportation and not in the horizontal direction. A general solution of the Su-Field model was found: (1) replace the original field F1 with another field F2; (2) add another field F2 to enhance the practical effect; and (3) increase S3 and add another field F2 to enhance the effect [19]. Due to the lack of horizontal drive in the car system, solution (2) is selected to increase the horizontal driving force F2 on the car to strengthen the usefulness of the system, as shown in Fig. 6. However, due to the directional effect of the guiding system, the car is subjected to an excessive vertically guided mechanical force, and the vehicle still does not move horizontally. The Su-Field model in question is shown in Fig. 7.

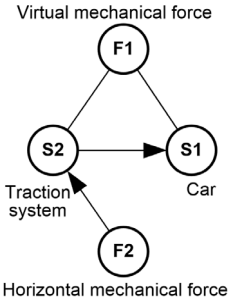

Fig. 6. *Su-Field model after adding F2*

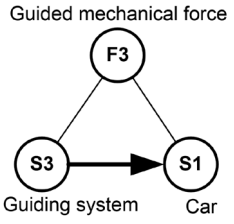

Fig. 7. *Su-Field model of the guiding system*

According to TRIZ theory, the Su-Field model is analysed, and the system is a complete Su-Field model with three elements, but the guiding device produces limits the orientation of the car, which yields a harmful complete model. The general solution of the look-up Su-Field model is as follows. (1) Add another substance S3 to prevent harmful effects. S3 can be an existing substance, variations of S1 and S2, or a substance obtained by decomposing the environment. (2) Add another field, F2, to balance the field that produces harmful effects [19].

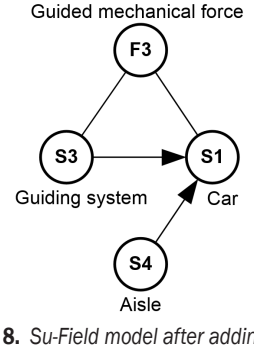

Fig. 8. *Su-Field model after adding S4*

According to the results of causal analysis, the orientation limitation of the car and the guiding system is caused by the shape of the shaft. Therefore, according to solution (1), aisle S4 is added to change the shape of the shaft, allow the car to move horizontally and overcome the excessive vertical guiding mechanical force of the guiding system, as shown in Fig. 8. When the car runs vertically in the shaft, it runs horizontally in the aisle to avoid influencing the car when it moves. The complete Su-Field model after eliminating insufficient and excessive performance factors is shown in Fig. 9.

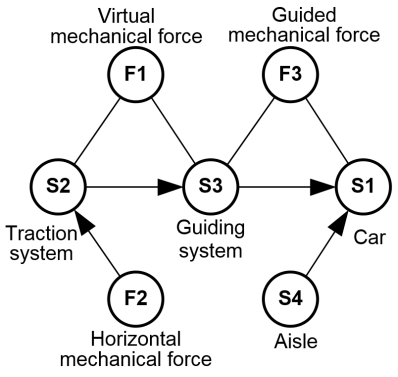

Fig. 9. *Complete Su-Field model*

2.4 Conflict Analysis

In the solution obtained from the analysis of the Su-Field model, the car should be able to complete both vertical and horizontal operations, and there is a problem associated with the car running direction that must be solved. Elevator operation requires both vertical and horizontal car operations, which are physical contradictions. Using separation principles is an important way to solve physical contradiction problems. TRIZ summarizes the separation principle into four categories: separation in space, separation in time, separation between the whole and its parts, and separation based on conditions [28]. Different separation principles correspond to different inventive principles.

After analysing the problem, the space separation principle is selected. Separation in space involves separating the two sides of a conflict in different spaces to reduce the difficulty of solving the problem. In the space separation principle [28], the available inventive principles are No. 1: segmentation, No. 2: taking out, No. 3: local quality, No. 4: asymmetry, No. 7: nested doll, No. 13: the other way round, No. 17: another dimension, No. 24: intermediary, No. 26: copying, and No. 30: flexible membranes / thin films. One or more of the given invention principles can be selected to solve the invention problem.

2.5 Generate Solutions

According to the analysis of physical contradictions, many inventive principles are obtained. Each inventive principle is a suggestion. By referring to these suggestions, the invention principle(s) most suitable for the current problem can be selected, the system can be changed, and the contradictions in the system can be eliminated [17]. According to the analysis, the inventive principles most suitable for solving the elevator horizontal movement problem are selected, and the solutions are generated.

No. 1. Segmentation
Divide an object into independent parts.

The invention principle is analysed, and a design scheme is proposed to divide the car into two parts to run independently according to the direction of operation. The car is divided into a vertical car and a transverse car. The vertical car runs vertically in the elevator shaft. Only the passengers who need to move vertically are transported. The transverse car runs in the aisle and conveys passengers who need to move horizontally.

No. 24. Intermediary
Use an intermediary carrier article or intermediary process.

According to this invention principle, a design scheme is proposed to realize horizontal movement by adding a driving device at the bottom of the moving car with reference to rail-guided vehicle and metro systems. The wheel-rail system, which is widely applied in the field of rail transit, is used as the driving device and installed at the bottom of the transverse car. The track is laid on the running path of the transverse car. However, because passengers who require horizontal movement usually need to move vertically as well, the transverse car must also run vertically. Therefore, the driving system must be further designed for the transverse car.

No. 2. Taking out
Extract the only necessary part (or property) of an object.

According to this invention principle, a design scheme that allows the vertical driving of the transverse car using the existing traction system is proposed. In the current scheme, the vertical car runs vertically and is driven by the traction system, so the existing traction system is used to drive the transverse car to move vertically. When a transverse car needs to run vertically, it enters the shaft and performs vertical operations through the traction system. In this scheme, the connection between the transverse car and the existing traction system should be considered.

No. 17. Another dimension
Go from a single story or layer to a multi-storey or multilayer system.

No. 7. Nested doll
Place one object inside another.

Based on the two inventive principles above, the design proposal of a double-decker car is proposed. The vertical car is divided into two layers. The upper-deck car is responsible for transporting the passengers who need to move vertically. The lower-deck car transports the passengers horizontally. A guide rail is installed at the bottom of the lower-deck car. When the transverse car needs to run vertically, it enters the lower-deck portion of the shaft from the passageway and runs vertically to the target layer driven by the driving traction system. The operation flow is shown in Fig. 10.

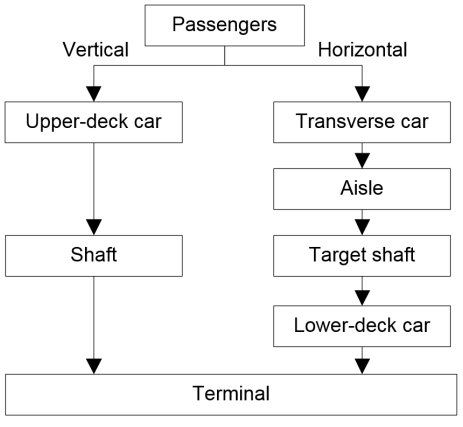

Fig. 10. *Operation flow of the vertical and transverse elevator*

However, in this scheme, there is often an angle at the junction between the aisle and the shaft where the car needs to be turned, as shown in Fig. 11. The size of the transverse car is relatively small, and the transverse car must run smoothly in the steering process to avoid passenger discomfort; therefore, an appropriate driving device for the transverse car must be designed.

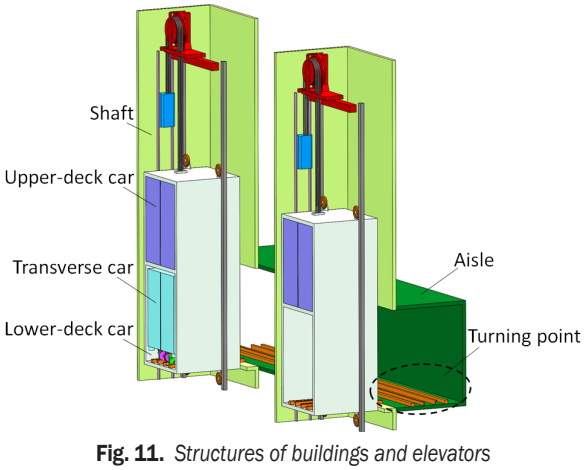

Fig. 11. *Structures of buildings and elevators*

No. 13: The other way round

Invert the action used to solve the problem.

The driving device of the transverse car must effectively perform driving and steering functions. The harmful factor is the steering function. When the car turns, the positions of the passengers in the car will also rotate, which will cause discomfort. According to this invention principle, a design scheme is proposed in which the main body of the car remains motionless while steering and only the driving device rotates. An active steering device and a fixing device are installed at the turning point of the passage, and a passively driven steering device is added to the transverse car. When the transverse car needs to change direction, the fixing device keeps the main body of the transverse car motionless, and the active steering device drives the passive steering device to rotate 90 degrees, changing the direction of motion of the driving device. The structures of the active steering device and fixing device are shown in Fig. 12. The structure of the transverse car is shown in Fig. 13. To ensure the safety of the transverse car, an anti-roll device and brake device are installed at the driving device. The structure of the driving device is shown in Fig. 14.

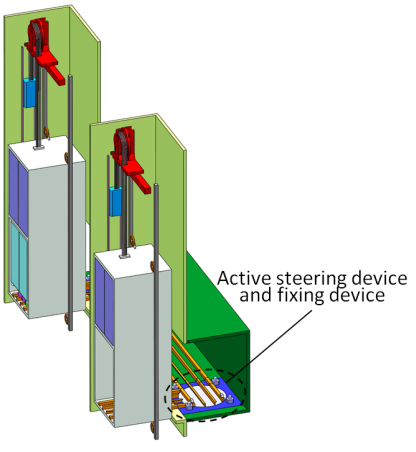

Fig. 12. *The structure of the active steering device and fixing device*

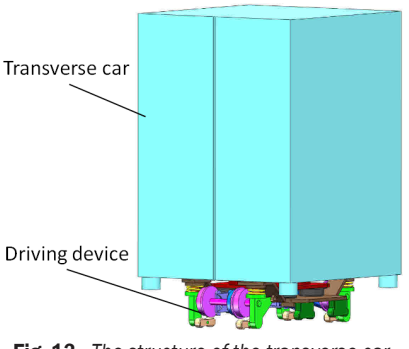

Fig. 13. *The structure of the transverse car*

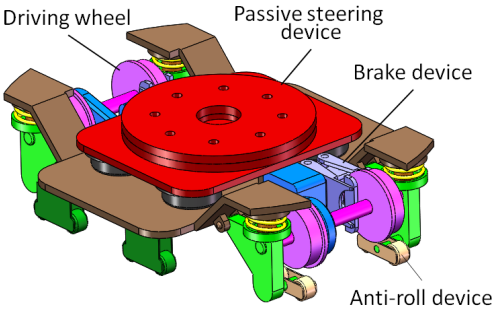

Fig. 14. *The structure of the driving device*

When the transverse car needs to move horizontally to the target shaft, it leaves the lower-deck car and enters the turning point of the current shaft. Then, the transverse car moves horizontally in the aisle to the turning point of the target shaft path to change direction. The number of the aisle is according to the type of buildings and the number of passengers. Finally, the transverse car enters the lower-deck car of the target shaft. The transverse car is then driven vertically by the traction system, as shown in Fig. 15.

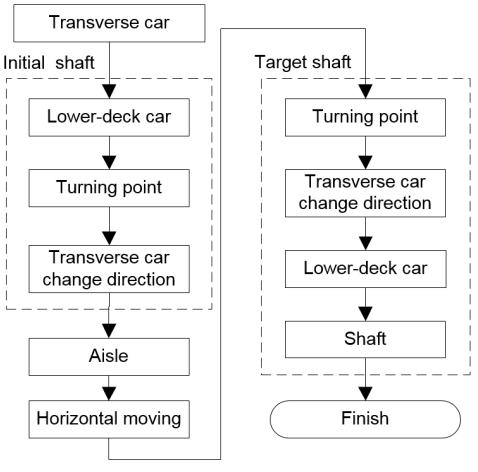

Fig. 15. *Operation flow of vertical and transverse elevator*

To further verify the design scheme obtained through TRIZ, a vertical and transverse elevator model is constructed, as shown in Fig. 16. The elevator model has two aisles, four floors, one transverse car and two shafts. The elevator control system is based on an Advanced RISC Machine (ARM). The stepping motor is used as the traction motor, and the transverse car receives and sends instructions by wireless communication. A digital steering gear is used to drive the active steering device, and an electromagnetic brake is installed in the passive steering device to ensure the accuracy of steering.

Fig. 16. *Vertical and transverse elevator model*

3 SIMULATION VERIFICATION

To verify the operational efficiency of the vertical and transverse lift elevator, the simulation of an 8-floor building is performed. Two shafts and two transverse cars are placed in the building, as shown in Fig. 17. The control strategy of the elevator is applied in this environment. The operational processes for the elevator are simulated with C# by employing an object-oriented design and multithreading method.

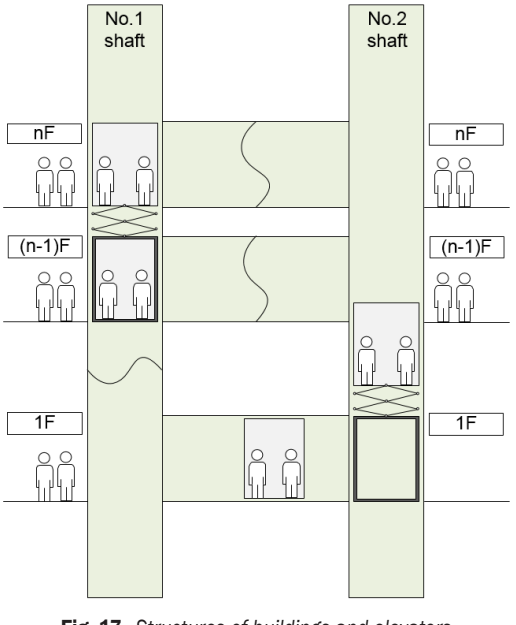

Fig. 17. *Structures of buildings and elevators*

3.1 Control Strategy

The control strategy of vertical and transverse elevators should satisfy the real-time dispatching schemes of upper-deck and transverse cars, coordinate the operation of each car to avoid conflicts, and plan the optimal dispatching scheme for elevators [29]. To reduce the complexity of the control strategy, the transverse car is abstracted as a passenger using an elevator that can issue a landing call and a car call. The vertical cars in the two shafts operate independently and respond dynamically to the instructions of passengers and the transverse cars. It is necessary to control the horizontal movement of the transverse car to make it run smoothly and orderly in the aisle. Therefore, the control strategy of the vertical and transverse elevators is proposed. A horizontal call button is added to the call ladder panel. The horizontal call ladder does not distinguish between upward and downward directions. When the call signal for the transverse car is activated, the transverse car moves to the waiting area of the target shaft.

The variable y is used to record the shaft number (y = 1, 2). When the transverse car enters the lower-deck car, variable i is changed. The variable k_y is used to record the upper-deck car on a given floor. Because the upper-deck car and the lower-deck car can answer the call at the same time, and the upper-car is one floor apart from the lower-car, the vertical control of the vertical and transverse elevator is determined relative to the upper-deck car on the floor. Sets are used to store transverse car and passenger instructions, as shown in Table 1. Because the control strategies of the cars in the No. 1 and No. 2 shafts are the same, only the control strategy in the No. 1 shaft (y = 1) is shown in Fig. 18.

Table 1. *Detailed simulation parameters*

Set	Function
Vu_y	Records upward passenger landing calls for vertical transport
Vd_y	Records downward passenger landing calls for vertical transport
Vn_y	Records upper-deck car calls
Hh_y	Records transverse car calls for horizontal transport
Hv_y	Records transverse car calls for vertical transport
U_y	Records transverse car calls for lower-deck car
h_i	Records the floor where the transverse car is located

S1: The elevator operates vertically. When the upper-deck car satisfies the upward movement constraint and is located at the highest floor of the current call path, the direction of operation changes to the downward direction, as shown in Eq. (1):

$$k_1 \in \max(Vu_1 \cup U_1 \cup Hh_1 \cup Vn_1). \quad (1)$$

When the lower-deck car moves downward to the lowest floor of the current call instruction, the direction of operation changes to the upward direction, as shown in Eq. (2):

$$k_1 \in \min(Vd_1 \cup U_1 \cup Hh_1 \cup Vn_1). \quad (2)$$

S2: The elevator stops answering vertical calls when Eq. (3) is satisfied:

$$k_1 \in Vu_1 \cup Vd_1 \cup U_1 \cup Hh_1 \cup Vn_1. \quad (3)$$

S3: Open and close the door of the upper-deck car. Load or unload the passengers who move vertically and update the instructions Vn_1 for the upper-deck car.

S4: The transverse car answers calls from the ladder in the waiting area. When the transverse car arrives at the target shaft, it sends out a call and waits

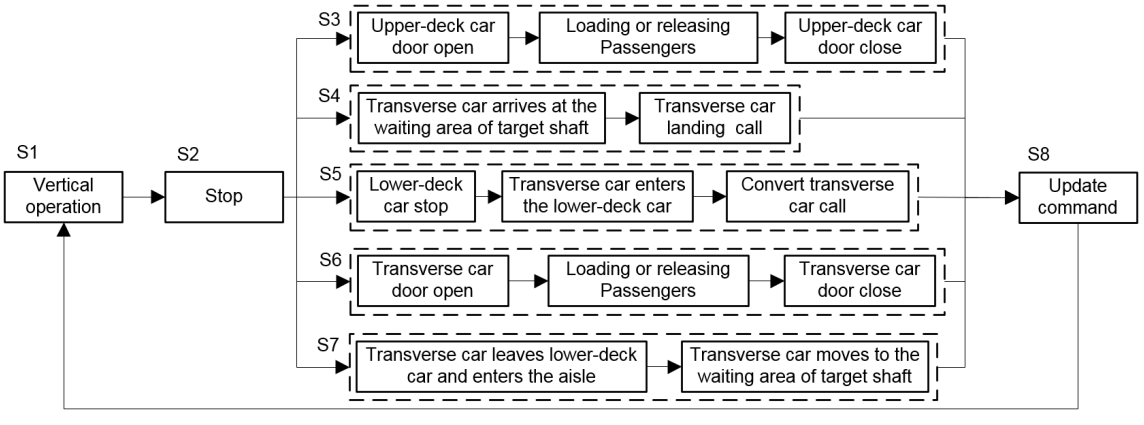

Fig. 18. *Control strategy of vertical and transverse elevator*

for the response of the lower-deck car, as shown in Eq. (4):

$$U_1=\{h_2\}. \tag{4}$$

S5: The transverse car enters the lower-deck car of the target shaft. When the lower-deck car reaches the target floor, the transverse car enters the lower-deck car and updates the number i of the transverse car and converts the horizontal call of the transverse car to a vertical call of the transverse car in the current shaft, as shown in Eq. (5):

$$Hv_1=Hh_1. \tag{5}$$

The horizontal call of the transverse car is cleared, as shown in Eq. (6):

$$Hh_1=\varnothing. \tag{6}$$

S6: Transverse car open and close the door. Load or release passengers who are running horizontally and update the transverse car call horizontal Hh_1 and vertical Hv_1.

S7: Transverse car into the aisle and moving horizontally. When there are no passengers to be released in the transverse car, as shown in Eq. (7):

$$Hv_1=\varnothing, \tag{7}$$

and the transverse car is on the lowest floor or highest floor, as shown in Eq. (1) or Eq. (2), the transverse car enters the aisle of the current floor and moves to the waiting area of the target shaft. If the current floor aisle is occupied, the transverse car moves up or down one floor, and choose a free aisle.

S8: Update all instructions.

In addition, the control system monitors the position of each car and the passengers in the car in real time. When the upper-deck car or transverse car is overloaded, the overloaded car only responds to release passengers, and the non-overloaded car runs normally.

3.2 Passengers' Flow Model

Passengers taking the elevator is a random process that is commonly modelled as a stochastic process. Passenger requests for elevator service time are stochastic. The passenger-starting floor and target floor are uncertain. A Poisson process is a more reasonable arrival model for dynamic service systems [30]. Assuming that the arrival intervals of passengers adjacent to the elevator are independently, negatively, and exponentially distributed, the arrival process of passengers within 5 minutes obeys the Poisson process, and the passenger arrival rate λ is as follows [31]:

$$\rho=\frac{(\lambda T)^n e^{-\lambda T}}{n!}, \quad (n=1,2,3...). \tag{8}$$

$$\lambda=\frac{CE\times Q}{300}, \tag{9}$$

where ρ is the probability of n passengers requesting elevator service within period T; λ passenger arrival rate, i.e., the average number of passengers using the elevator per unit time; CE_1 number of passengers using an elevator within 5 minutes; and Q total number of elevators in use.

Eq. (8) can be used to obtain the time between when passengers request and receive elevator service:

$$\begin{cases} t_0 = A \\ t_i = t_{i-1} - \dfrac{\ln(r)}{\lambda}, \ (i=1,2,3...) \end{cases}, \tag{10}$$

where t_0 is the start time of the passenger service request, that is, the start time of the system simulation; t_i first passenger service request for the elevator; and r random number generated in the interval of (0,1).

The Monte Carlo method is used to generate the starting and target floors of passengers in different traffic modes according to the proportions of up-peak, down-peak, and inter-floor passengers. The percentage of horizontal passengers to the total number of passengers is recorded as the transverse density. The numbers of horizontal and vertical passengers are determined by the Monte Carlo method.

3.3 Simulation Platform

To study the elevator's effect of the vertical and traversing on the passenger mobility efficiency, a vertical and transverse elevator simulation platform was developed. The simulation platform was designed with C# and used a multithreading method to simulate the operation of vertical and transverse elevators. The simulation platform mainly includes an interactive interface, a passengers' flow simulation module, an elevator operation module and a data statistics module. The simulation interface is mainly used to configure the parameters of each module and display the running status of the elevator. The passengers' flow simulation module generates passengers' flows under different traffic modes according to the Poisson distribution and Monte Carlo method. In the same passengers' flow environment, the elevator operation module simulates the operation of the vertical and transverse elevator

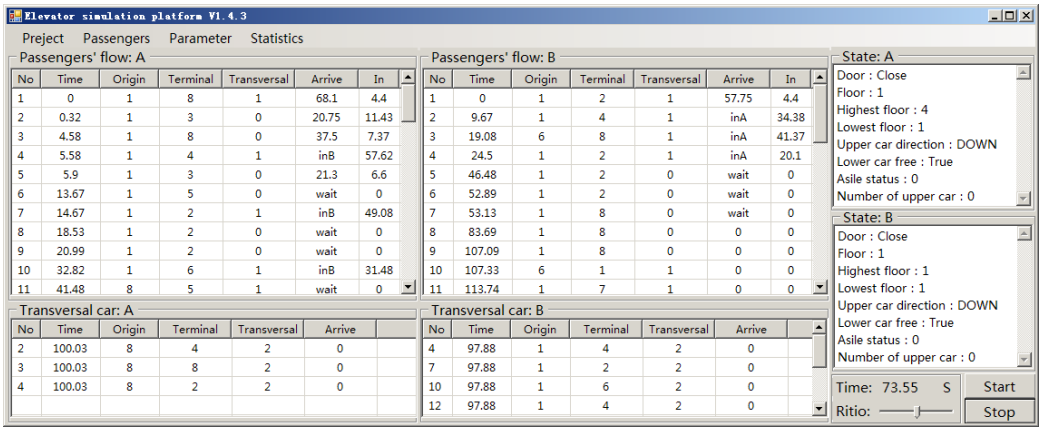

Fig. 19. *Elevator simulation platform*

and the ordinary elevator. The ordinary elevator is a single-deck car elevator without an installed aisle. The data statistics module is responsible for recording the operation parameters and times of elevator operations and calculating the average waiting time, average riding time, and passenger mobility efficiency. The elevator simulation platform is shown in Fig. 19.

3.4 Simulation Case

Vertical and transverse elevators are arranged in an eight-floor building. The system consists of two vertical cars and two transverse cars. In total, 640 passengers are distributed evenly among the eight floors, generating 300 s of passengers' flow data per simulation, and the elevator simulation parameters are shown in Table 2. The simulation is conducted in the up-peak, down-peak, and inter-floor traffic modes. The configuration of traffic modes is shown in Table 3. By comparing the arrival times of multi-direction elevator passengers and ordinary elevator passengers based on the same parameters, the influence of the newly proposed elevator on the passenger mobility efficiency is obtained. The 'averagesimulation' code was executed five times for each group to ensure the accuracy of the experiment.

Table 2. *Detailed simulation parameters*

Parameters	Value
Story height	4 m
Number of elevator users	640
Aisle length	200 m
Passenger arrival rate	0.128
Vertical speed of the elevator	1.5 m/s
Horizontal speed of the elevator	8 m/s
Acceleration	1.5 m/s^2
Passenger walking speed	1 m/s
Number of upper-deck car	10
Number of transverse cars	10
Opening/closing door time	1 s
Entry/exit time for each passenger	0.5 s

Table 3. *Distribution of different traffic modes*

	Up-peak	Inter-floor	Down-peak
Upward ratio [%]	80	10	10
Inter-floor ratio [%]	10	80	10
Downward ratio [%]	10	10	80

The effect of the vertical and transverse elevator on the arrival efficiency of all passengers is shown in Fig. 20, and the effect on the arrival efficiency of horizontal-moving passengers is shown in Fig. 21. The data analysis indicated that the efficiency of horizontal-moving passengers was significantly improved by adding the transverse car, and the total efficiency of all passengers also significantly improved. The efficiency of the vertical and transverse elevator was high, especially in the up-peak and inter-floor traffic modes.

Additional data analysis indicated that the run of the transverse car will have an impact on the vertical passengers. The average waiting times of vertical passengers for the ordinary elevator and vertical and transverse elevators are compared for different transverse densities, as shown in Fig. 22. In down-peak traffic mode, the vertical and transverse elevator has an obvious impact on the average waiting time of vertical passengers, and lesser effects are observed in the up-peak and inter-floor traffic modes.

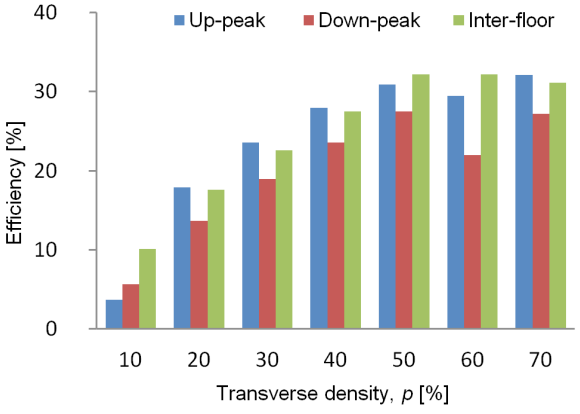

Fig. 20. *The arrival efficiency of all passengers*

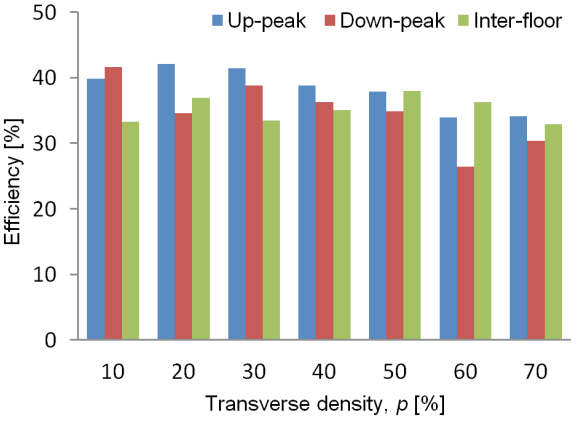

Fig. 21. *The arrival efficiency of horizontal moving passengers*

To study the influence of the transverse distance on the vertical and transverse elevator effectiveness, the transverse distance is set to 300 metres and 400 metres. In the simulation, other parameters remain unchanged. The transverse distances are 200 metres, 300 metres and 400 metres, and the effect of the vertical and transverse elevator on the arrival efficiency of all passengers is shown in Fig. 23.

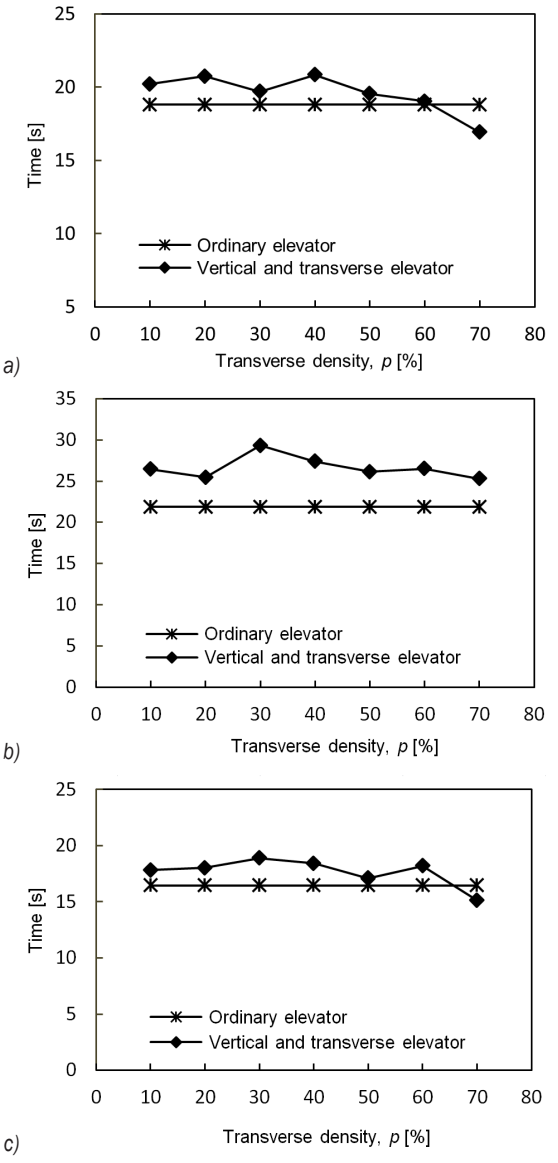

Fig. 22. *Comparison of average waiting time for vertical passengers when the aisle is 200 meters; a) up-peak traffic mode, b) inter-floor traffic mode, and c) down-peak traffic mode*

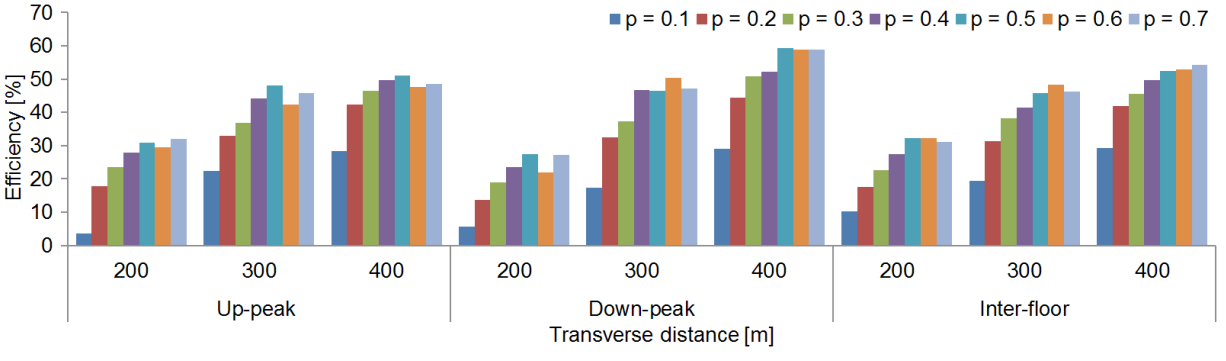

Fig. 23. *The arrival efficiency of all passengers when the transverse distance is 200,300 and 400 meters*

As the transverse distance increases, the efficiency of the vertical and transverse elevator for all passengers increases. The average waiting times of vertical passengers for the ordinary elevator and vertical and transverse elevator are compared for a transverse distance of 400 metres, as shown in Fig. 24. A comparison of Figs. 22 and 24 shows that the average waiting time of vertical passengers does not significantly increase as the transverse distance of the vertical and transverse elevator increases.

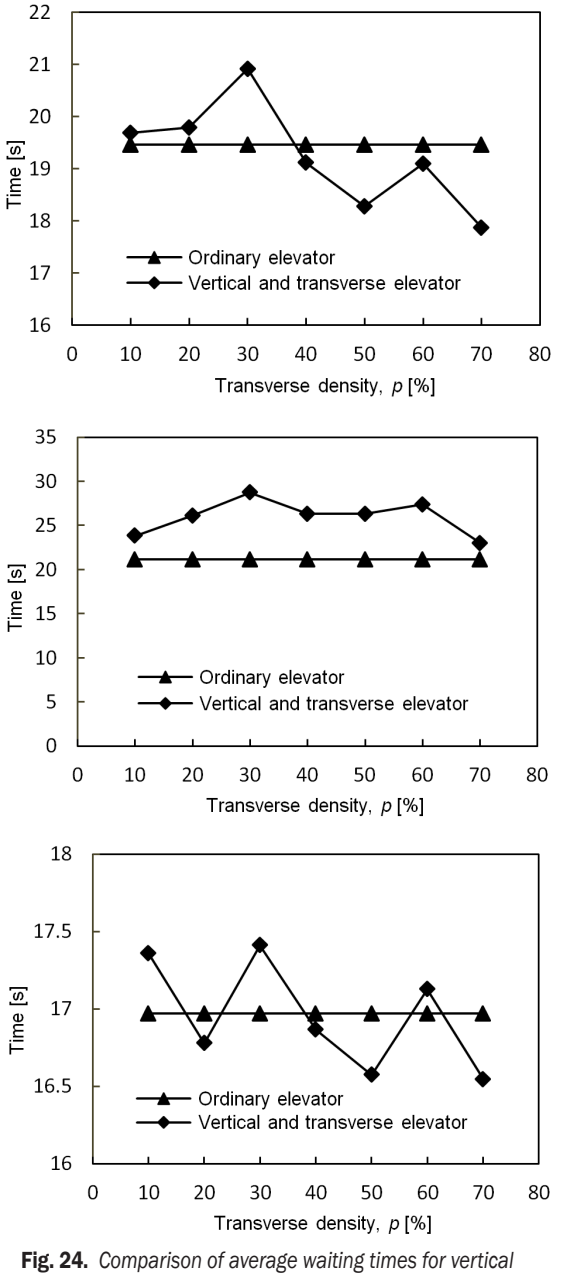

Fig. 24. *Comparison of average waiting times for vertical passengers when the aisle is 400 meters; a) up-peak traffic mode, b) inter-floor traffic mode, and c) down-peak traffic mode*

4 DISCUSSION

In the above cases, the efficiency of the vertical and transverse elevator for horizontal passengers is significantly improved, mainly because the passengers using the ordinary elevator must walk horizontally to their destination and the horizontal moving speed of the transverse car is much higher than that of the walkers. However, the operation of the transverse car also has an impact on the efficiency of the vertical passengers, especially in the down-peak traffic mode, as shown in Figs. 22b and 24b. Among the three traffic modes, passengers in the down-peak traffic mode are more dispersed on the initial and target floors. As a result, the number of transverse car stops required to answer the calls in the vertical direction is greater than that in other cases, so the average waiting time for vertical passengers has a notable impact on the overall system efficiency. However, compared with the improvement in the horizontal mobility efficiency of passengers, the impact on the vertical passengers is negligible.

In the cross-control strategy of the vertical and transverse elevator, when the transverse car responds to the passenger elevator signal, it does not distinguish between the movement directions of the passenger (i.e., horizontal vs vertical). However, the passenger in an ordinary elevator must wait when the elevator runs in the direction opposite their direction of travel. Therefore, under certain conditions, the average vertical passenger time of the vertical and transverse elevator may be less than that of the ordinary elevator. As shown in Fig. 24a, the average waiting time of vertical passengers using the vertical and transverse elevator is lower than that of the ordinary elevator when the transverse distance is 400 metres, and the transverse density p is greater than 0.4. Therefore, in the future, we can conduct in-depth research on this phenomenon and optimize the control strategy in down-peak traffic mode to reduce the average waiting time of vertical passengers and improve operational efficiency.

5 CONCLUSIONS

Based on TRIZ theory, this paper uses functional models, causal analysis, conflict analysis, the Su-Field model and other tools to innovate on the basis of traditional elevators. A vertical and transverse elevator design proposal for a double shafts structure is proposed. The control strategy is designed according to the vertical and transverse elevator structure design. A simulation platform for the elevator structure is

developed with C# to investigate the operational efficiency for different traffic modes and transverse distances. The simulation results show that the vertical and transverse elevator can effectively improve the mobility efficiency of passengers in the horizontal direction in the pre-set environment, and the mobility efficiency of all passengers also significantly improves.

6 ACKNOWLEDGEMENTS

The authors would like to thank the support of the National Natural Science Foundation of China (Grant No. 61303087), the Key R & D project of Shandong Province (Grant No. 2016GGX103042) and Innovation Team Support Project of Co-Innovation Center for Green Building of Shandong Province in Shandong Jianzhu University (No. X18024Z). Jiwen Chen and Xin Li contributed equally to this work.

7 REFERENCES

[1] Chai, K.-H., Zhang, J., Tan, K.-C. (2005). A TRIZ-based method for new service design. *Journal of Service Research*, vol. 8, no. 1, p. 48-66, **DOI:10.1177/1094670505276683**.

[2] Lin, S.Y., Wu, C.T. (2016). Application of TRIZ inventive principles to innovate recycling machine. *Advances in Mechanical Engineering*, vol. 8, no. 5, p. 1-8, **DOI:10.1177/1687814016647303**.

[3] Altshuller, G.S. (1984). *Creativity as Exact Science: The Theory of the Solution of Inventive Problems*. Gordon & Breach Science Publishers, London.

[4] Ikuta, M., Takahashi, K., Inaba, M. (2013). Strategy selection by reinforcement learning for multi-car elevator systems. *IEEE International Conference on Systems, Man, and Cybernetics*, p. 2478-2484, **DOI:10.1109/SMC.2013.423**.

[5] So, A., Al-Sharif, L., Hammoudeh, A. (2016). Concept design and derivation of the round trip time for a general two-dimensional elevator traffic system. *Journal of Building Engineering*, vol. 5, p. 165-177, **DOI:10.1016/j.jobe.2015.12.006**.

[6] Barker, F.H. (1997). A technical primer: the Otis odyssey system. *Proceedings of International Conference on Council on Tall Buildings and Urban Habitat*, p. 55–76.

[7] Trochimczuk, R., Huścio, T. (2017). Rope-free elevator system based on planar positioners for vertical and horizontal transport. *Mechanika*, vol. 23, no. 1, p. 120-125, **DOI:10.5755/j01.mech.23.1.13868**.

[8] So, A., Al-Sharif, L., Hammoudeh, A. (2018). Traffic analysis of a three-dimensional elevator system. *Building Services Engineering Research and Technology*, vol. 39, no. 1, p. 5-20, **DOI:10.1177/0143624417710106**.

[9] Appunn, R., Frantzheld, J., Jetter, M., Löser, F. (2018). MULTI® - rope-less elevator demonstrator at test tower Rottweil. *Transportation Systems and Technology*, vol. 4, no. 3, p. 80-89, **DOI:10.17816/transsyst20184380-89**.

[10] Srinivasan, R., Kraslawski, A. (2006). Application of the TRIZ creativity enhancement approach to design of inherently safer chemical processes. *Chemical Engineering & Processing: Process Intensification*, vol. 45, no. 6, p. 507-514, **DOI:10.1016/j.cep.2005.11.009**.

[11] Liu, W., Cao, G., Tan, R. (2016). Research on optimization of TRIZ application driven by design needs and targets. *Procedia CIRP*, vol. 39, p. 33-38, **DOI:10.1016/j.procir.2016.01.162**.

[12] Petković, D., Issa, M., Pavlović, N.D., Zentner, L. (2013). Application of the TRIZ creativity enhancement approach to the design of a passively adaptive compliant robotic gripper. *Assembly Automation*, vol. 33, no. 3, p. 231-239, **DOI:10.1108/AA-10-2013-079**.

[13] Gronauer, B., Naehler, H. (2016). TRIZ as an amplifier for corporate creativity and corporate innovation ability. *Procedia CIRP*, vol. 39, p. 185-190, **DOI:10.1016/j.procir.2016.01.186**.

[14] Wang, Y.-H., Lee, C.-H., Trappey, A.J.C. (2017). Service design blueprint approach incorporating TRIZ and service QFD for a meal ordering system: A case study. *Computers & Industrial Engineering*, vol. 107, p. 388-400, **DOI:10.1016/j.cie.2017.01.013**.

[15] Efimov-Soini, N.K., Chechurin, L.S. (2016). Method of ranking in the function model. *Procedia CIRP*, vol. 39, p. 22-26, **DOI:10.1016/j.procir.2016.01.160**.

[16] Mi, J.S., Lee, J.-G., Park, J.-M., Lee, S. (2012). Triggering navigators for innovative system design: the case of lab-on-a-chip technology. *Expert Systems with Applications*, vol. 39, no. 16, p. 12451-12459, **DOI:10.1016/j.eswa.2012.04.068**.

[17] Cho, C.-H. , Chae, S.-W., Kim, K.-H. (2014). Search for a new design of deburring tools for intersecting holes with TRIZ. The *International Journal of Advanced Manufacturing Technology*, vol. 70, no. 9-12, p. 2221-2231, **DOI:10.1007/s00170-013-5459-y**.

[18] Petković, D., Issa, M., Pavlović, N.D., Zentner, L. (2013). Application of the triz creativity enhancement approach to design of passively compliant robotic joint. *International Journal of Advanced Manufacturing Technology*, vol. 67, no. 1-4, p. 865-875, **DOI:10.1007/s00170-012-4530-4**.

[19] Savransky, S.D. (2002). *Engineering of Creativity.* CRC Press, New York.

[20] Hsieh, H.T., Chen, J.L. (2010). Using TRIZ methods in friction stir welding design. *International Journal of Advanced Manufacturing Technology*, vol. 46, no. 9-12, p. 1085-1102, **DOI:10.1007/s00170-009-2172-y**.

[21] Cao, G.Z., Guo, H.X., Liang, T., Tan, R.H. (2011). Function modeling, solving and simulation based on effect in TRIZ. *Advanced Materials Research*, vol. 418-420, p. 2190-2194, **DOI:10.4028/www.scientific.net/AMR.418-420.2190**.

[22] Busov, B., Mann, D., Jirman, P. (1999). Case studies in TRIZ: a novel heat exchanger (use of function analysis modelling to find and eliminate contradictions). *The 3rd European Invention Machine User Group Conference*, Munich.

[23] Aurisicchio, M., Bracewell, R., Armstrong, G. (2013). The function analysis diagram: intended benefits and coexistence with other functional models. *Artificial Intelligence for Engineering Design, Analysis and Manufacturing*, vol. 27, no. 3, p. 1-26, **DOI:10.1017/S0890060413000255**.

[24] Liu, W., Cao, G., Tan, R. (2016). Research on optimization of TRIZ application driven by design needs and targets. *Procedia CIRP*, vol. 39, p. 33-38, **DOI:10.1016/j.procir.2016.01.162**.

[25] Cui, S.-h., Mei, J.-p., Zhang, L., Du, X. (2017). Based on the theory of TRIZ solving the problem of 18650 battery electrolyte filling. *IOP Conference Series: Earth and Environmental Science*, p. 1-5, **DOI:10.1088/1755-1315/104/1/012018**.

[26] Chou, J.R. (2014). An ideation method for generating new product ideas using TRIZ, concept mapping, and fuzzy linguistic evaluation techniques. *Advanced Engineering Informatics*, vol. 28, no. 4, p. 441-454, **DOI:10.1016/j.aei.2014.06.006**.

[27] Fan, D.L., Hu, J.W., Yu, H.L. (2011). Application of Su-Field analysis method to the innovation of decision-making. *Applied Mechanics and Materials*, vol. 130-134, p. 135-138, **DOI:10.4028/www.scientific.net/AMM.130-134.135**.

[28] Hipple, J. (2012). *TRIZ Separation Principles. In: The Ideal Result*. Springer, New York.

[29] Tanaka, S., Hoshino, D., Watanabe, M. (2016). Group control of multi-car elevator systems without accurate information of floor stoppage time. *Flexible Services and Manufacturing Journal*, vol. 28, no. 3, p. 461-494, **DOI:10.1007/s10696-016-9238-6**.

[30] So, A.T., Chan, W.L. (2009). *Intelligent Building Systems*. Johnson Controls Asia, Hong Kong.

[31] Pan, Z., Luo, F., Xu, Y. (2007). Elevator traffic flow model based on dynamic passenger distribution. *IEEE International Conference on Control and Automation*, p. 2386-2390, **DOI:10.1109/ICCA.2007.4376789**.

Strojniški vestnik - Journal of Mechanical Engineering 65(2019)5, 311-318
DOI:10.5545/sv-jme.2018.5938
Original Scientific Paper
Received for review: 2018-12-18
Received revised form: 2019-03-29
Accepted for publication: 2019-05-07

Determination of the Effect of Cold Working Compression on Residual Stress Reduction in Quenched Aluminium Alloy 2219 Block

Abdulrahaman Shuaibu Ahmad[1,2] – Wu Yunxin[1,2,*] – Gong Hai[1,2] – Liu Lei[2]
[1]Central South University, College of Mechanical and Electrical Engineering, China
[2]Central South University, State Key Laboratory of High-Performance Complex Manufacturing, China

Residual stresses are induced in components during mechanical, thermal, machining, and plating operations. If not carefully considered in the design process, residual stress can be a significant factor in the failure of components, particularly when subjected to alternating service loads or corrosive environments. The induced residual stresses in three quenched aluminium alloy 2219 blocks were experimentally investigated, and cold working compression was performed at room temperature to relieve the stresses. High residual stresses were observed in the blocks after quenching. Therefore, their reduction became necessary to improve the tolerance of machined parts and avoid their failure. The samples were cold-worked at various compression ratios (CR). The residual stresses were significantly relieved, and it was discovered that 2 % CR offers a considerable effective reduction in the residual stress. Relieving these residual stresses will improve the reliability of the samples and the components to be manufactured.

Keywords: residual stress, aluminium alloy 2219, quenching, cold working compression

Highlights

- *Residual stresses were analysed after quenching the 2219 aluminium samples.*
- *The samples were cold compressed using various CR after quenching.*
- *The residual stress relieving efficiencies of the selected CR were compared.*
- *The final results show that 2 % CR is the most effective in residual stress reduction.*

0 INTRODUCTION

Residual stresses are locked-in stresses that remain in solid materials after the removal of the external cause of stresses [1]. Residual stresses are induced in components during most manufacturing processes, such as material deformation, heat treatment, machining, or processing operations that transform the shape or change the properties of the material [1]. They develop when a body undergoes inhomogeneous plastic deformation or is exposed to a non-uniform temperature distribution, such as in the case of welding, warm forming, casting, and quenching processes [2] to [4].

A material's ability to resist fatigue, and crack initiation and propagation at ambient temperature, brittle fracture, machining distortion, and corrosion cracking is adversely affected by residual stresses [3] and [5] to [7]. These effects regularly cause significant costs of repairs or replacement of parts [5]. Analysis of residual stresses is considered as one of the necessary steps in the design of structural elements and components, which aid in predicting their reliability under different loading conditions during operation [6]. Extensive studies revealed that the fatigue strength of welded elements is drastically reduced due to high residual stresses induced at the weld bead and heat-affected zone (HAZ) [8] and [9]. Webster et al. reported that residual stress, which can be in excess of the yield strength of the material, could develop at the HAZ: is the region near the weld zone that is not melted during welding, but its properties have been severely altered due to the effect of the welding torch [10] to [12]. Therefore, the effects of residual stresses are comparably the same as that of stress concentration. Residual stresses are now considered one of the leading factors influencing the properties of metallic materials. Thus, they should be given due consideration during the design and manufacturing of parts and components. Due to their self-equilibrating nature, the presence of residual stresses may not be readily evident, and so they may not be carefully considered during engineering design. However, they are stresses and must be given due consideration in the same way as stresses due to external loading.

The hole-drilling technique based on ASTM E-837-13a standard [13] is used to measure the residual stresses, as presented in this paper; the residual stresses cannot be measured directly [14]. Usually, the elastic strains resulting from the relieved stresses initially present at hole position are measured directly, then, the residual stresses can be computed using mathematical relations.

*Corr. Author's Address: Central South University, College of Mechanical and Electrical Engineering, Changsha, China, wuyunxin@mail.csu.edu.cn

Aluminium alloy 2219 is the material used in this experiment; it is a commonly used material for the manufacture of components used for high-temperature applications, high strength weldment, supersonic aircraft structures as well as space industry applications [15] to [17]. It requires strengthening through heat treatment before the parts mentioned above are manufactured; during the process, high residual stresses are induced. Therefore, their reduction becomes necessary to improve the reliability of the manufactured parts.

The techniques for relieving residual stresses are mainly categorized into the thermal methods (i.e., heat treatment and mechanical methods, which include cold working compression) stretching, and some other mechanical surface treatment techniques, etc. [18] to [20]. Based on experimental and manufacturing outcomes, stretching appears to be more effective in relieving residual stresses, but it is practically impossible to stretch an unsymmetrical and non-rectangular shaped component due to handling difficulties and non-symmetrical loading. As such, compression processes are favourably considered and commonly employed [2]. Hence, compression is mainly applied to parts having simple geometries and parallel surfaces. Cost-effectiveness, availability, and accessibility to equipment also decides the technique to be used for relieving residual stresses. Muammer et al. compared the compression and stretching techniques of residual stress reduction for quenched aluminium 7050 [2]. Up to 90 % reduction in residual stresses for 2 % (CR) was reported.

A quenching experiment was performed in the first section of this paper, and the residual stresses induced in three quenched aluminium alloy 2219 blocks are determined using the hole-drilling method. In the second section, the cold working compression for relieving the induced residual stresses was carried out; different CRs were applied for each sample. Moreover, the residual stresses were measured for the compressed Al 2219 blocks. Finally, the x and y components residual stresses before and after compression were compared, and the average relieved residual stresses for each selected CR was also presented.

1 QUENCHING EXPERIMENT

Three samples of an aluminium alloy 2219 block of the same dimensions 200 mm × 160 mm × 130 mm were heated to an elevated temperature of 540 ℃ and held for 4 hours in the furnace; the samples were then quenched in the water of 40 ℃ for 10 minutes. The quenching conditions are shown in Table 1. The blocks were allowed to cool to room temperature before the residual stress measurement was carried out, Figs. 1 and 2 show the samples prepared for heat treatment.

Table 1. *Conditions for the heat treatment*

Parameters	Symbol	Value
Blocks temperature before quenching	T_0	540 ºC
Quenching medium temperature	T_t	40 ºC
Blocks temperature after quenching	T_1	40 ºC
Quenching duration	t	600 s

Fig. 1. *Aluminum 2219 block samples*

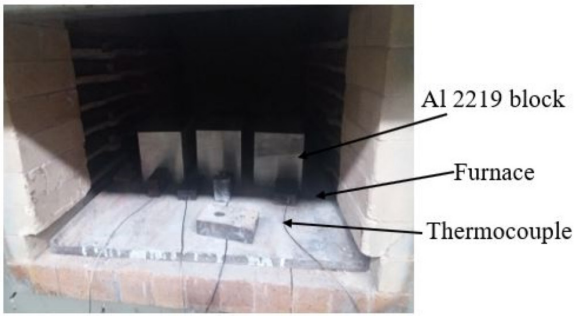

Fig. 2. *Samples prepared in a furnace*

1.1 Material Properties

The average density of the Al 2219 used in this work is 2820 kg/m³ [21], the temperature-dependent properties of the Al 2219 shown in Figs. 3 to 7 were measured at the Nonferrous, Advanced Structure Materials and Manufacturing Research Center, Central South University, China.

The residual stresses induced during the quenching process were then measured using the hole - drilling method base on the uniform stress method.

1.2 Residual Stress Measurement using Hole-drilling Technique

Based on the ASTM E837-13a standard [13], the hole-drilling measurement can be performed using the

uniform or non-uniform stress method to examine the residual stresses.

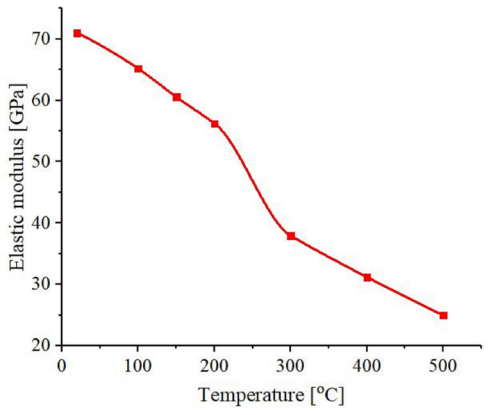

Fig. 3. *The elastic modulus of aluminum 2219; Poisson ratio = 0.33 at all temperatures*

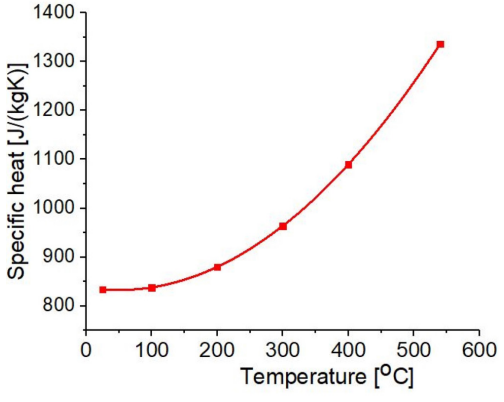

Fig. 4. *Specific heat of aluminum 2219*

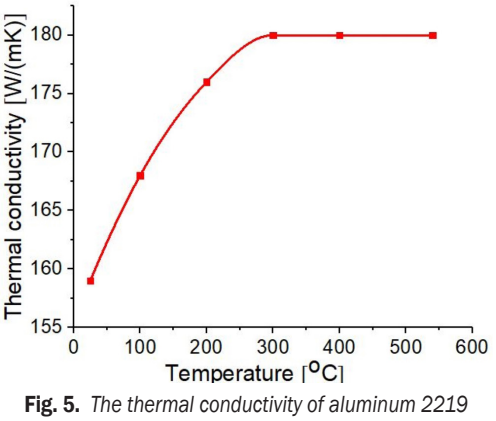

Fig. 5. *The thermal conductivity of aluminum 2219*

(a) *Uniform stress method*: In this approach, the in-plane stresses are considered uniform throughout the drilled hole depth for material whose thickness is larger in comparison with the strain gage circle and hole diameter. Therefore, a blind hole can be drilled, and the strain data will be recorded after reaching the required depth (maximum of 2 mm).

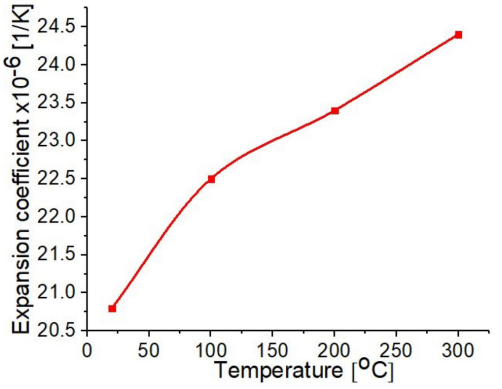

Fig. 6. *Thermal expansion of aluminum 2219*

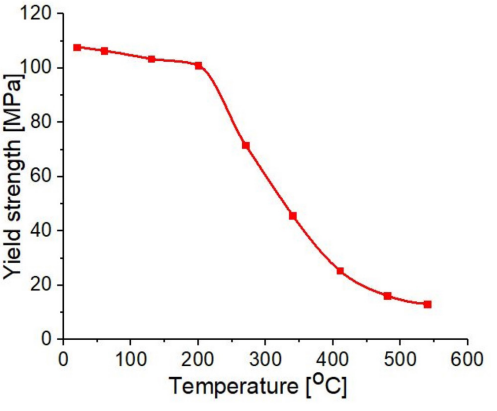

Fig. 7. *The yield stress of aluminum 2219; plastic strain = 0, at the given temperature range*

(b) *Non-uniform stresses method*: in this approach, the in-plane stresses are considered to vary with the depth of the hole. Therefore, an incremental hole drilling method is used; the hole is drilled in steps, depending on the workpiece thickness and the strain gage parameters, and the strains are recorded after every increment [14]. In this paper, considering the thickness of the samples (130 mm), the strain gage circle diameter (5.13 mm), the hole diameter (1.8 mm), and the hole depth (2 mm), which is a near-surface region, the in-plane residual stresses and are considered to be uniform. Therefore, the uniform stress technique was adopted. It is evident that the residual stresses cannot be measured directly using this method, thus, the relieved strains which depends on the residual stresses that existed in the material originally within the drilled hole are determined directly. Therefore, the residual stresses at the drilled-hole locations were evaluated from the relieved strains using the mathematical relations based on the linear

elasticity theory as shown in Eq. (1) [15] and [22]. Fig. 8. Illustrates the in-plane stresses in *x* and *y* directions.

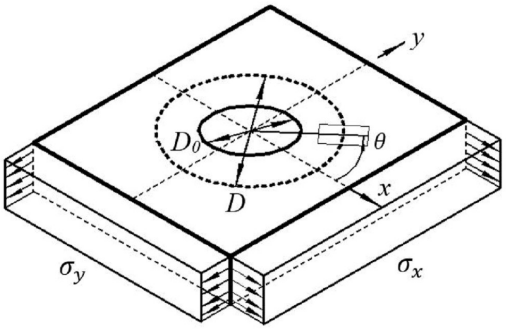

Fig. 8. *Hole geometry and uniform stresses along x and y - components* [13]

$$\varepsilon = \frac{\sigma_x + \sigma_y}{2}\frac{(1+\vartheta)\bar{a}}{E} + \frac{\sigma_x - \sigma_y}{2}\frac{\bar{b}}{E}\cos 2\theta + \\ + \tau_{xy}\frac{\bar{b}}{E}\sin 2\theta. \quad (1)$$

Eq. (1) can also be written as

$$\varepsilon = P\frac{(1+\vartheta)\bar{a}}{E} - Q\frac{\bar{b}}{E}\cos 2\theta + T\frac{\bar{b}}{E}\sin 2\theta,$$

where

$$P = \frac{\sigma_x + \sigma_y}{2}, \quad Q = \frac{\sigma_y - \sigma_x}{2}, \quad T = \tau_{xy}. \quad (2)$$

In Eqs. (1) and (2), and are the "uniform" in-plane stresses and θ is the angle between the strain gage axis and the *x* direction. The terms and are calibration constants that define the strain/stress sensitivity of the measurement. Their numerical values depend on the drilled-hole diameter and depth. *P*, *Q* and *T* are the combination stresses, and represents the Poisson ratio depending on the isotropic strains.

The combination stresses *P*, *Q*, and *T* are corresponding to the combination strains *p*, *q*, and *t*. Therefore, Eq. (2) can be rewritten in terms of the combination stresses, and their corresponding combination strains as follows.

$$P = \frac{\sigma_x + \sigma_y}{2} = \frac{E}{(1+\vartheta)\bar{a}}p, \quad (3)$$

$$Q = \frac{\sigma_y - \sigma_x}{2} = \frac{E}{\bar{b}}q, \quad (4)$$

$$T = \tau_{xy} = \frac{E}{\bar{b}}t, \quad (5)$$

where

$$p = \frac{\varepsilon_3 + \varepsilon_1}{2}, \quad q = \frac{\varepsilon_3 - \varepsilon_1}{2}, \text{ and } t = \frac{\varepsilon_3 - 2\varepsilon_2 + \varepsilon_1}{2}. \quad (6)$$

The combination strains *p*, *q*, and *t* in the Eq. (6) represent the isotropic, 45o shear and axial shear strains, and they are calculated using the above equations. The stresses and are then evaluated using Eqs. (7), (8) and (9) below.

$$\sigma_x = P - Q, \quad (7)$$

$$\sigma_y = P + Q, \quad (8)$$

$$\tau_{xy} = T. \quad (9)$$

Type A strain gage rosette with a circle diameter of 5.13 mm was used in this experiment, the axial strains were deducted directly from the strain gage output display, which were used to obtain all the required parameters using the above equations. Fig. 9 shows the layout of the type A strain gage rosette and Fig. 10 shows the workpiece with the rosette attached.

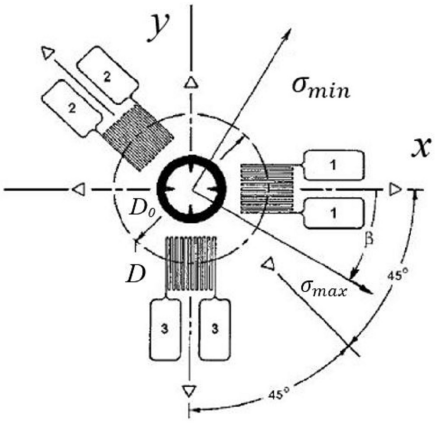

Fig. 9. *Strain gage rosette layout* [9], [13]

2.4 Residual Stresses after Quenching

The residual stresses measurement was carried out using the MTS3000 hole-drilling machine with drilling resolution of 5 μm, and drilling speed range of 0.03 mm/min to 1 mm/min, the residual stresses at three various points on the surfaces of each sample were determined at drilling speed of 0.8 mm/min. Fig. 11 illustrates the selected positions on the workpieces and Fig. 12 shows the drill aligned to the rosette's centre during the measurement.

The relieved strains from the drilled hole at points 1, 2, and 3 were measured directly, then residual stresses are evaluated for each examined

point, the results are shown in Tables 2 to 4, and are also graphically presented in Figs. 13 to 15.

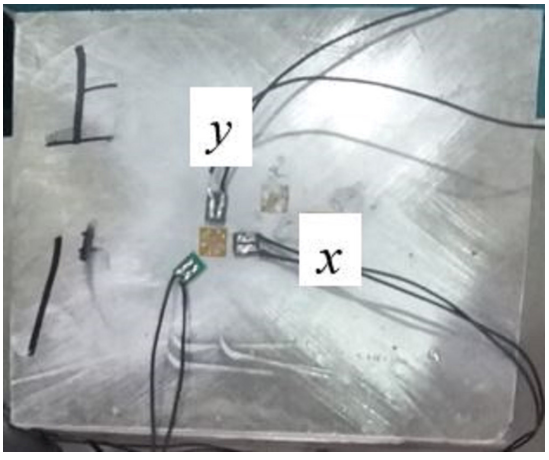

Fig. 10. *Aluminum block sample with rosette attached*

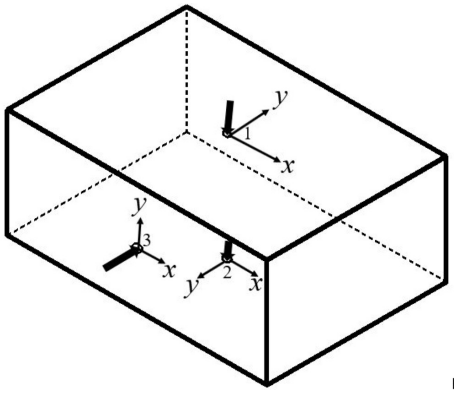

Fig. 11. *Test points on the block*

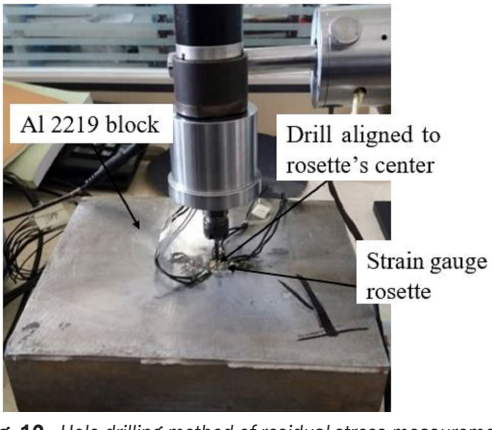

Fig. 12. *Hole-drilling method of residual stress measurement*

The quenching was performed in a stationary medium. Therefore, some parts of the workpiece, i.e. position 2 was first exposed to the quenching water before position 1; this can lead to variation in the residual stress distribution at positions 1 and 2 as the residual stresses are fully induced at the quenching stage.

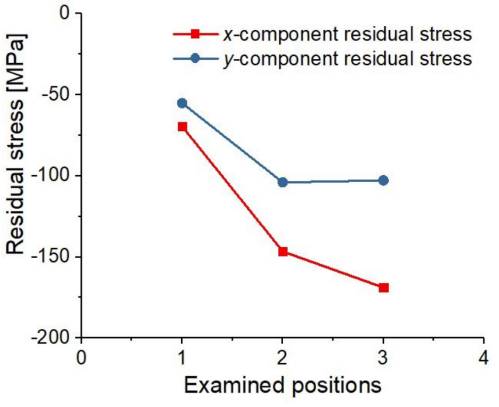

Fig. 13. *Determined residual stresses (RS) in sample 1 after quenching*

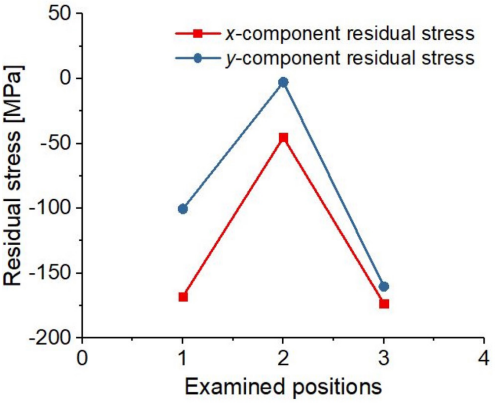

Fig. 14. *Evaluated residual stresses in sample 2 after quenching*

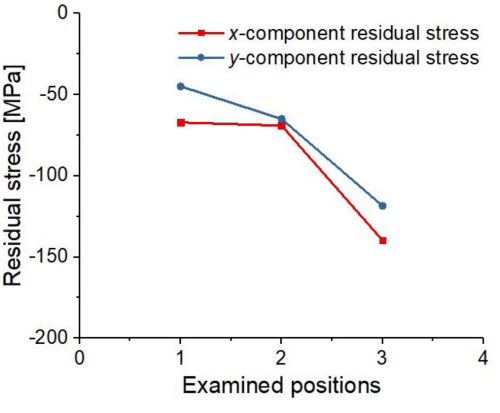

Fig. 15. *Evaluated Residual stresses in sample 3 after quenching*

The above results show the residual stresses induced due to the quenching at three locations on all the samples, the residual stresses are higher along x component (σ_x) of all the three samples, and they are

compressive residual stresses. It was observed that, σ_x = –168.89 MN/m² is the highest residual stress in sample 1, which is observed from point 3, σ_x = –173.41 MN/m² is the highest residual stress in sample 2, and it is obtained from point 3, and σ_x = –139.81 MN/m² is the highest residual stress in sample 3, and it is also determined from point 3 of the block. Therefore, relieving these stresses is very important to improve the reliability of the 2219 aluminium block and also to avoid the failure of manufactured components **[23]** to **[25]**.

3 RELIEF OF RESIDUAL STRESSES THROUGH COLD WORKING COMPRESSION

Cold working compression process with a rigid flat die was performed on the three samples to reduce the residual stresses induced due to quenching. Fig. 16 shows the conceptual view of the process.

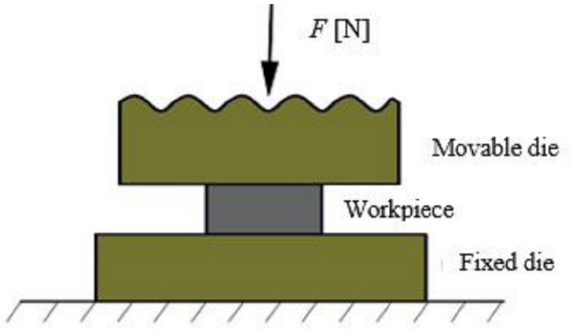

Fig. 16. *The cold working compression process*

Different CRs were selected for each sample to analyse the most efficient ratio in the residual stress reduction. The conditions for cold working compression applied to the samples are shown in Table 2 below.

Table 2. *CR for different samples*

S/N	Samples	CR [%]
1	Sample 1	2
2	Sample 2	3
3	Sample 3	4

4 RESULTS

The three aluminium alloy 2219 blocks were compressed using the assigned CRs; the residual stresses in all the three blocks were measured using the hole-drilling method based on the uniform stress method after the cold working compression. Since the stresses are assumed to be uniform within the in-plane directions *x* and *y*, residual stresses were measured at points corresponding to 1, 2, and 3 on all three blocks. The evaluated σ_x and σ_y are shown in Tables 3 to 5 and Figs. 17 to 19.

Table 3. *Residual stresses after cold working compression for sample 1*

	Examined locations	σ_x [MN/m²]	σ_y [MN/m²]
2 % CR	1	15.61	21.13
	2	14.65	16.28
	3	–12.41	13.24

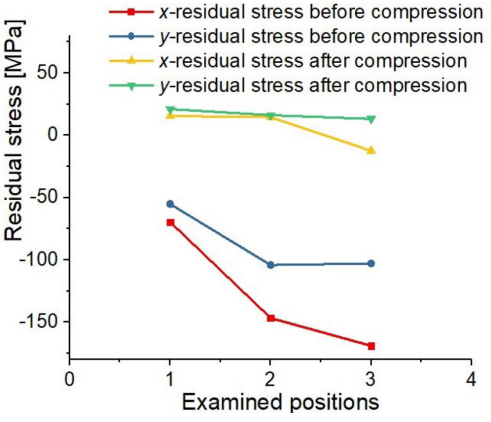

Fig. 17. *Residual stresses before and after compression (CR = 2 %) in sample 1*

Table 4. *Residual stresses after cold working compression for sample 2*

	Examined locations	σ_x [MN/m²]	σ_y [MN/m²]
3 % CR	1	28.93	34.57
	2	–5.74	9.07
	3	23.78	53.39

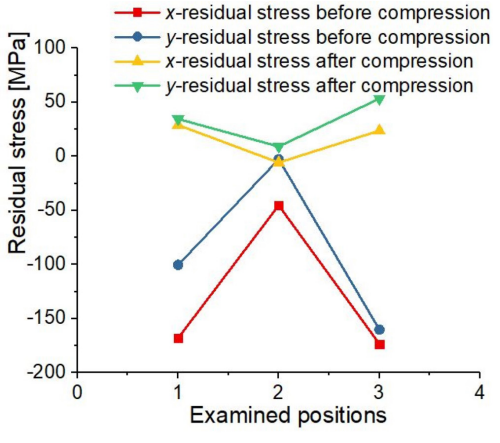

Fig. 18. Residual stresses before and after compression (CR = 3 %) in sample 2

Table 5. *Residual stresses after cold working compression for sample 3*

	Examined locations	σ_x [MN/m²]	σ_y [MN/m²]
4 % CR	1	6.81	15.42
	2	10.33	14.5
	3	–29.22	10.22

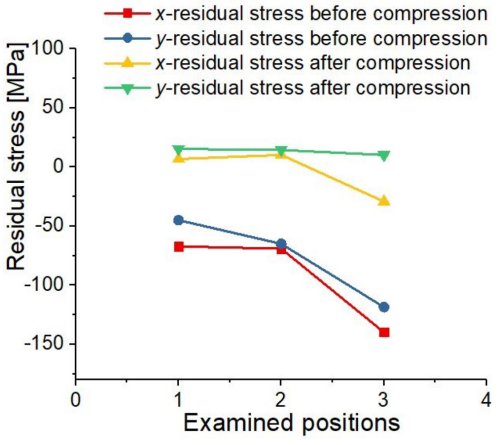

Fig. 19. *Residual stresses before and after compression (CR = 4 %) in sample 3*

5 DISCUSSION

Based on the results obtained after the cold working compression, a significant reduction in the residual stresses was observed. As reported by Koç et al. [2] cold compression using 2 % (CR) can relieve up to 90 % of residual stresses induced due to quenching of Al 7050. As analysed, the same performance can be obtained using the same CR on Al 2219 specimen. Furthermore, comparing the three CRs used, 2 % offers better stress reduction capacity than 3 % and 4 %, but the same may not hold when applying the stretching technique to relieve the stresses. Also, much efficient reduction in the residual stress along x component was observed for all the CR. Therefore, the stresses along x were relieved by a higher percentage compared to y. The average relived stresses are summarized in Table 6.

Table 6. *Average relieved residual stresses*

Samples	Average residual stress relieved [%] x component	Average residual stress relieved [%] y component	CR [%]
1	86.8	81.87	2
2	85.4	46.0	3
3	84.7	51.2	4

6 CONCLUSIONS

The residual stresses induced due to quenching were experimentally investigated and were observed to be very high; if combined with the residual stresses induced during machining, manufacturing processes and externally applied loads can easily cause the failure of manufactured parts. The cold working compression reduces the residual stresses significantly and efficiently based on the compression ratio used for each aluminium alloy 2219 sample. The 2 % compression ratio is observed to have the highest percentage of residual stress reduction. Relieving the residual stress is very important and necessary to enhance the better reliability of components under real service conditions. Therefore, it can be concluded that the cold working compression is a very efficient, effective and practically achievable method of reducing the high amount of residual stresses induced in aluminium 2219 components.

7 ACKNOWLEDGEMENTS

The authors are sincerely grateful to the management of the Central South University, School of mechanical and electrical engineering, Changsha, China, for providing all the required equipment used for the experiments carried out.

8 REFERENCES

[1] Şimşir, C., Gür, C. (2010). A Simulation of the quenching process for predicting temperature, microstructure, and residual stresses. *Strojniški vestnik - Journal of Mechanical Engineering*, vol. 56, no. 2, p. 93-103.

[2] Koç, M., Culp, J., Altan, T. (2006). Prediction of residual stresses in quenched aluminum blocks and their reduction through cold working processes. *Journal of Materials Processing Technology*, vol. 174, no. 1–3, p. 342–354, **DOI:10.1016/j.jmatprotec.2006.02.007**.

[3] Eslampanah, A.H., Aalami-aleagha, M.E., Feli, S., Ghaderi, M.R. (2015). 3-D numerical evaluation of residual stress and deformation due welding process using simplified heat source models. *Journal of Mechanical Science and Technology*, vol. 29, no. 1, p. 341-348, **DOI:10.1007/s12206-014-1240-x**.

[4] Urevc, J., Koc, P., Štok, B. (2009). Numerical simulation of stress relieving of an austenite stainless steel. *Strojniški vestnik - Journal of Mechanical Engineering*, vol. 55, no. 10, p. 590-598.

[5] Sim, W.-M. (2010). Challenges of residual stress and part distortion in the civil airframe industry. *International Journal of Microstructure and Materials Properties*, vol. 5, no. 4-5, p. 446-455, **DOI:10.1504/IJMMP.2010.037621**.

[6] Freborg, A., Ferguson, B., Li, Z. (2012). Predicting distortion and residual stress in a vacuum carburized and gas quenched

steel coupon. *Proceedings from the 6th International Quenching and Control Distortion Conference*, p. 22-33.

[7] Huang, X., Sun, J., Li, J. (2015). Effect of initial residual stress and machining-induced residual stress on the deformation of aluminium alloy plate. *Strojniški vestnik - Journal of Mechanical Engineering*, vol. 61, no. 2, p. 131-137, **DOI:10.5545/sv-jme.2014.1897**.

[8] Ogrinec, P., Čepon, G., Boltežar, M. (2018). Introduction of welds into the dynamic model of laminated structures. *Strojniški vestnik - Journal of Mechanical Engineering*, vol. 64, no. 2, p. 73-81, **DOI:10.5545/sv-jme.2017.4915**.

[9] Lee, J., Hwang, J., Bae, D. (2018). Welding residual stress analysis and fatigue strength assessment at elevated temperature for multi-pass dissimilar material weld between alloy 617 and P92 steel. *Metals and Materials International*, vol. 24, no. 4, p. 877-885, **DOI:10.1007/s12540-018-0086-7**.

[10] Webster, G.A., Wimpory, R.C. (2001). Non-destructive measurement of residual stress by neutron diffraction. *Journal of Materials Processing Technology*, vol. 117, no. 3, p. 395-399, **DOI:10.1016/S0924-0136(01)00802-0**.

[11] Wang, M., Liu, Y., Zan, T., Gao, X., Zhang, Y. (2016). Residual stress test and simulation of incremental hole-drilling method. *7th International Conference on Mechanical and Aerospace Engineering*, p. 257-261, **DOI:10.1109/ICMAE.2016.7549546**.

[12] Bae, D.H., Sohn, I.S., Hong, J.K. (2003). Assessing effects of residual stress on the fatigue strength of spot welds. *Welding Journal*, no. 1, p. 18-23.

[13] ASTM E837-13a (2013). Standard Test Method for Determining Residual Stresses by the Hole-Drilling Strain-Gage Method, West Conshohocken, ASTM International, **DOI:10.1520/E0837-13A**.

[14] Grant, P.V., Lord, J.D., Whitehead, P. (2006). The measurement of residual stresses by the incremental hole-drilling technique. *Measurement Good Practice Guide*, vol. 53, no. 2, p. 63.

[15] Liu, L., Wu, Y., Gong, H., Li, S., Kai W. (2019). Modification of constitutive model and evolution of activation energy on 2219 aluminum alloy during warm deformation process. *Transactions of Nonferrous Metals Society of China*, vol. 29, no. 3, p. 448-459, **DOI:10.1016/S1003-6326(19)64954-X**.

[16] Liu, L., Wu, Y., Gong, H., Li, S., Ahmad, A.S. (2018). A physically based constitutive model and continuous dynamic recrystallization behavior analysis of 2219 Aluminum alloy during hot deformation process. *Materials*, vol. 11, no. 8, 1443, **DOI:10.3390/ma11081443**.

[17] Liu, L., Wu, Y., Gong, H. (2018). Effects of deformation parameters on microstructural evolution of 2219 Aluminum alloy during intermediate thermo-mechanical treatment process. *Materials*, vol. 11, no. 8, 1496, **DOI:10.3390/ma11091496**.

[18] Prime, M.B., Newborn, M.A., Balog, J.A. (2003). Quenching and cold-work residual stresses in aluminum hand forgings: Contour method measurement and FEM prediction. *Materials Science Forum*, vol. 426-432, p. 435-440, **DOI:10.4028/www.scientific.net/MSF.426-432.435**.

[19] Žagar, S., Grum, J. (2011). Surface integrity after mechanical hardening of various Aluminium alloys. *Strojniški vestnik - Journal of Mechanical Engineering*, vol. 57, no. 4, p. 334-344, **DOI:10.5545/sv-jme.2010.092**.

[20] Wang, Y., Yang, H., Zhang, C., Fei Yu, F. (2015). Analysis of the residual stress in zirconium subjected to surface severe plastic deformation. *Metals and Materials International*, vol. 21, no. 2, p. 260-269, **DOI:10.1007/s12540-015-4195-2**.

[21] ASM Handbook Committee (1990). Properties of wrought aluminum and aluminum alloys. P*roperties and Selection: Nonferrous Alloys and Special-Purpose Materials, ASM Handbook*, vol. 2, p 62-122, ASM International, Materials Park, **DOI:10.1361/asm.hb.v02.a0001060**.

[22] Rendler, N.J., Vigness, I. (1966). Hole-drilling strain-gage method of measuring residual stresses. *Experimental Mechanics*, vol. 6, no. 12, p. 577-586, **DOI:10.1007/BF02326825**.

[23] Masoudi, S., Amini, S., Saeidi, E., Eslami-Chalander, H. (2015). Effect of machining-induced residual stress on the distortion of thin-walled parts. *The International Journal of Advanced Manufacturing Technology*, vol. 76, no. 1-4, p. 597-608, **DOI:10.1007/s00170-014-6281-x**.

[24] Zhang, Q.Z., Shu, B.F., Chen, M.B., Liang, Q.B., Fan, C., Feng, Z.Q., Verlinden, P.J. (2015). Numerical investigation on residual stress in photovoltaic laminates after lamination. *Journal of Mechanical Science and Technology*, vol. 29, no. 2, p. 655-662, **DOI:10.1007/s12206-015-0125-y**.

[25] Kang, S.-W., Jang, B.-S., Song, H.-C. (2015). Residual stresses analysis of friction stir welding using one-way FSI simulation. *Journal of Mechanical Science and Technology*, vol. 29, no. 3, p. 1111-1121, **DOI:10.1007/s12206-015-0223-x**.

Strojniški vestnik - Journal of Mechanical Engineering 65(2019)5, 319-325

DOI:10.5545/sv-jme.2018.5965
Short Scientific Paper
Received for review: 2018-12-31
Received revised form: 2019-04-11
Accepted for publication: 2019-05-08

Development of a Mixing Mechanism with a Complex Motion of the End-effector

Alexey Fomin* – Wsevolod Ivanov
Siberian State Industrial University, Russia

This study is focused on the development and analysis of a single-driven mixing mechanism, synthesized with a minimum number of links and joints. The end-effector of this mechanism is designed as a screw ending with a mixing element (blades) moving along a spatial trajectory. The end-effector is set between movable links in the kinematic chain of the mechanism. This allows increasing the working zone of the end-effector. The study provides kinematic analysis via an analytical method of coordinate transformations that have resulted in the detection of variable kinematic parameters (tilt angles and displacements in joints) depending on driving link rotation angle. Based on these results, the motion trajectory of the mixing element has been analytically determined and reproduced. Analytical findings have been verified by results of motion simulations. The presented mechanism is advisable to use for the preparation of various mixtures and levelling the concentrations and temperature of mixed substances. The mechanism can be used in the food, medical, chemical, and construction industries, as well as in agriculture.

Keywords: kinematic pair, mixing mechanism, degree-of-freedom, spatial trajectory, analytical kinematics.

Highlights

- *A novel single-driven mixing mechanism in which an end-effector reproduces a movement with four degrees-of-freedom has been synthesized.*
- *It has been found that the developed mechanism is the simplest one in terms of numbers and types of joints and links for the reproduction of prescribed motion with four degrees-of-freedom.*
- *Kinematic analysis has been carried out with the definition of all variable parameters (tilt angles and displacements in joints), and the spatial trajectory of the end-effector has been calculated and reproduced.*
- *The proposed mechanism can be applied for preparation of various mixtures and the levelling of concentrations and temperatures in mixed substances.*

0 INTRODUCTION

Improvements in the machine-building industry have radically affected the development of associated industries by the introduction of advanced and high-performance techniques. It has become possible to ensure advanced characteristics of created machines and mechanisms as early as at the design stage.

One of the basic stages in the creation of any mechanical system is the structural synthesis (design) of its kinematic scheme, considering the numbers and types of links and joints, as well as their placement in a kinematic chain. One study [1] provides a synthesis method that allows obtaining these parameters for parallel mechanisms based on the theory of linear transformations. Another synthesis method is shown in [2]; it is applied for serial-parallel mechanisms with spatial multi-loop kinematic chains based on the displacement group theory and the Assur principle. In another study [3], the authors show a design method of the five-bar screw-lever manipulator and vary its end-effector's trajectory. The proposed method is based on searching for optimal geometries of links that allow reproducing complex screw trajectories by the end-effector. One study [4] provides fundamental concepts for diverse mechanical systems behind the design, analysis, control, and programming.

Thus, it becomes possible to guarantee the required law motion of a designed system and its high efficiency at the stage of the structural synthesis.

In addition, the provision of the minimum number of drives and movable elements in designed systems is a relevant task, the solution of which allows ensuring advanced reliability, high speed, and efficiency, as well as reducing structural loads in links and joints during its operation. In [5], a systematic procedure for the synthesis of single-loop compliant mechanisms having minimum elements is provided. These mechanisms are applied for adaptive structures. Another study that proposes a synthesis of mechanisms with minimum elements is [6], in which Grubler's method is used for designing mechanisms with two general imposed constraints. In [7], the optimal design of mechanisms considering tolerances on link lengths and clearances in joints is applied for four-bar linkages as the simplest systems. In [8], a multi-objective optimization procedure for a robotic

*Corr. Author's Address: Siberian State Industrial University, Department of Mechanics and Mechanical Engineering, Kirova Str. 42, 654007 Novokuznetsk, Russia, alexey-nvkz@mail.ru

arm is developed based on the implementation of design criteria.

The presented study is focused on the synthesis of mixing mechanisms. Fig. 1 shows the simplest mixing mechanisms based on the kinematic schemes of single-driven planar four-bar linkages: crank-rocker (Fig. 1a) and crank-slider (Fig. 1b). Both linkages include fixed link 1, crank 2, coupler 3, oscillating link 4, and mixing element 5. Oscillating link 4 is made as a rocker in Fig. 1a, when it is made as a slide block in Fig. 1b.

In both mechanisms, the end-effector is coupler 3 that is set between movable links 2 and 4. This feature makes it possible to reach an increased working zone of mixing element 5, which is rigidly mounted on coupler 3 in both mechanisms. The fault of construction of such mechanisms is that mixing element 5 moves along a planar trajectory. If the spatial motion of the mixing element could be reached, the efficiency of the mixing process would be significantly increased.

There are other mechanisms for mixing operations in which end-effectors are guided along spatial trajectories. There is a mechanism that reproduces complex screw trajectories with a curvilinear axis, presented in [3]. A mixing device that provides a complex trajectory with four dependent motions is shown in [9]. Several parallel mechanisms shown in [10] have been synthesized to reach combined spatial motions by their end-effectors.

Despite the opportunity to reproduce the spatial movements of end-effectors in these mechanisms, the efficiency of their functioning for mixing processes can be improved with the development of their kinematic chains, as well as improvement of output trajectories.

This study aims to develop a novel mixing mechanism, which could include a minimum number of movable links, a single drive, only one-degree-of-freedom (DoF) joints, only double-paired links and to provide a movement of the end-effector along a spatial trajectory. Also, the end-effector of the proposed mechanism will be mounted on the intermediate link in the kinematic chain to obtain its increased working zone.

1 SYNTHESIS OF KINEMATIC SCHEME OF MIXING MECHANISM

Simple mechanisms, those that have a minimal number of links and joints, are preferable for practical reasons. The design issue of such mechanisms is directly related to finding the ratio between the number of DoF of a designed system, the numbers and types of links and joints, as well as the number of general constraints imposed on a whole system. These parameters are considered in the universal formula of mobility [11], written below:

$$W_m = (6-m)n - \sum_{k-m=1}^{k=5} (k-m)\, p_k, \qquad (1)$$

where W_m is the mobility of a mechanical system determining the number of its DoF, m is the number of general constraints imposed on the entire mechanical system, n is the number of movable links, k is a class of kinematic pairs (joints) determining their DoF, from 5 to 1. Eq. (1) can be used to calculate structural parameters for synthesis of mechanisms with mobility $W_m > 0$, or kinematic chains with $W_m < 0$, or groups of zero mobility (Assur groups) with $W_m = 0$ [12] and [13]. This formula also allows carrying out structural

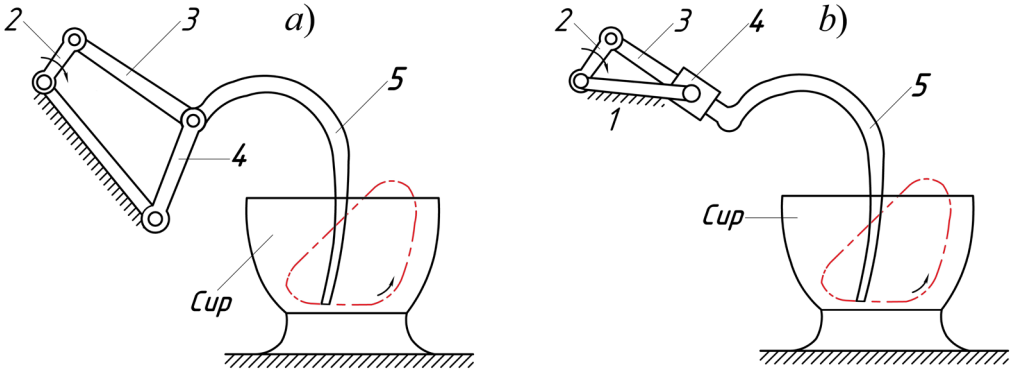

Fig. 1. *Kinematic schemes of mixing mechanisms based on planar four-bar linkages: a) crank-rocker, and b) crank-slider*

analysis of mentioned kinematic chains with different mobility.

For the aim of this study, accept the following conditions for the synthesized mechanism: having single drive (W_m=1); provision of one DoF for all joints ($p_5 \neq 0$, p_4=0, p_3=0, p_2=0, p_1=0); using only double-paired links (i.e., links that form two joints among themselves); ensuring a spatial motion with four DoF by the end-effector (m=2). According to these conditions, Eq. (1) is transformed into the following form:

$$n = (3p_5 + 1)/4. \quad (2)$$

According to (2), parameter n can take following values 1, 4, 7, 10, 13, ..., when p_5 is equal to 1, 5, 9, 13, 17, etc. The first solution when n=1 and p_5=1 describes the simplest mechanism, a crank or a slider. The next solution is when n=4 and p_5=5. According to this solution, the kinematic scheme of the planar mechanism shown in Fig. 1b will be transformed into the spatial form. At the same time, the position of all links in one or several parallel planes will be provided to minimize dynamic loads during movement.

The mechanism designed on this idea and included calculated parameters is shown in Fig. 2. This mechanism involves fixed link 1, crank 2, coupler 3, screw 4, at the end of which mixing element with blades 5 is rigidly mounted, and rocker 6 made in the form of a nut. Kinematic pairs of links 1-2, 2-3, 3-4, and 1-6 are rotational, and pair of links 4-6 is a screw. Moreover, the geometrical axes of joints 1-2, 2-3, and 1-6 are parallel to each other, and the geometrical axes of joints 3-4 and 4-6 lie in the perpendicular plane to them.

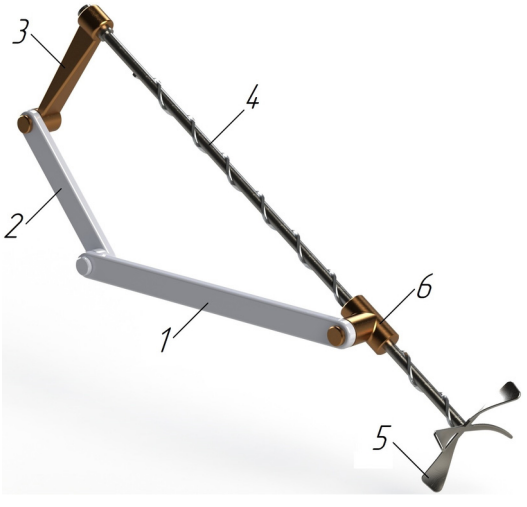

Fig. 2. *Mixing mechanism with a complex motion of the end-effector*

The input motion in this mechanism is realized by rotation of crank 2 around the geometric axis of links 1-2. According to Eq. (1), the mobility of the mechanism is equal to one (W_2=1). As distinct from the other four DoF mechanisms, such as 3T1R parallel manipulators shown in **[14]**, models of delta-robot shown in **[15]** and **[16]**, the proposed mixing mechanism has different types of end-effector motions. The end-effector, screw 4 with blades 6, has three motions (two prismatic and one rotational) in a single plane and additional rotational motion around the axial axis of screw 4.

The operational principle of this mechanism is in the following. When crank 2 is actuated, it drives coupler 3, which puts in motion screw 4. The distance between joints 3-4 and 4-6 will be changed, and rocker 6 will incline screw 4 with blades 5. Due to the presence of screw joint 4-6 and rotational joint 3-4 having an identical spinning axis, screw 4 has additional rotation around its axial axis.

Thus, the developed mechanism has a minimum number of links and single drive, while it realizes a spatial movement of blades 5 with four DoF. A minimum number of links and the presence of only one-DoF joints ensure the simplicity of the mechanism's design and increase the reliability of its functioning.

The application of this mechanism can be associated with performing various operations related to mixing. It can be used in the food, medical, chemical, and construction industries, as well as agriculture as a device for the preparation of homogeneous mixtures, as well as a device providing intensification of mass and heat exchange processes, equalizing the concentration and temperature of mixed substances.

2 KINEMATIC ANALYSIS OF MIXING MECHANISM

Regarding the motion trajectory definition of blades 5, it is appropriate to apply an analytical method of coordinate transformation for the kinematic analysis of the discussed mechanism as blades 5 are directed along a spatial trajectory. This method is widely used in analysing open and closed spatial kinematic chains. In **[17]**, this method is applied to the analysis of the biped robot Pasibot as open kinematic chain. The analysis of closed kinematic chains is presented in **[18]**, in which a 3CPS parallel manipulator is studied, and in **[19]**, in which the mechanism for internal surfaces cutting is investigated. Fig. 3 shows the kinematic scheme of the mixing mechanism, in which spatial coordinate systems are connected with

each link. The origin of coordinate system $O_1x_1y_1z_1$ is connected with link 1 and located in joint 1-2.

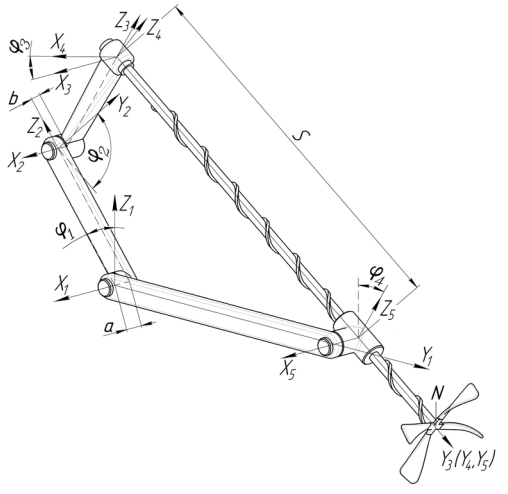

Fig. 3. *Toward a kinematic analysis of the mixing mechanism*

The origin of the coordinate system $O_2x_2y_2z_2$ is connected with crank 2 and located in joint 2-3. Axes x_1 and x_2 are parallel to each other. The mechanism is actuated by the rotation of crank 2 around axis x_1 at angle φ_1, which is a given parameter. The position of coordinate system $O_2x_2y_2z_2$ in system $O_1x_1y_1z_1$ is determined with the following Denavit and Hartenberg matrix:

$$\mathbf{T}^{(2,1)} = \begin{pmatrix} 1 & 0 & 0 & 0 \\ -a & 1 & 0 & 0 \\ -l_2\sin\varphi_1 & 0 & \cos\varphi_1 & -\sin\varphi_1 \\ l_2\cos\varphi_1 & 0 & \sin\varphi_1 & \cos\varphi_1 \end{pmatrix}, \quad (3)$$

where a is given structural dimension; l_2 is the length of crank 2. Parameters a and l_2 define the displacement of coordinate system $O_2x_2y_2z_2$ relative to system $O_1x_1y_1z_1$.

The origin of the coordinate system $O_3x_3y_3z_3$ is connected with coupler 3 and located in joint 3-4. Axes x_2 and x_3 are parallel to each other. The position of coordinate system $O_3x_3y_3z_3$ in system $O_2x_2y_2z_2$ is described using a Denavit and Hartenberg matrix, written in the following form:

$$\mathbf{T}^{(3,2)} = \begin{pmatrix} 1 & 0 & 0 & 0 \\ -b & 1 & 0 & 0 \\ -l_3\sin\varphi_2 & 0 & \cos\varphi_2 & \sin\varphi_2 \\ l_3\cos\varphi_2 & 0 & -\sin\varphi_2 & \cos\varphi_2 \end{pmatrix}, \quad (4)$$

where b is given structural dimension; l_3 is the length of coupler 3; φ_2 is a variable parameter describing the rotation of coupler 3 relative to crank 2. Parameters b and l_3 define the displacement of coordinate system $O_3x_3y_3z_3$ relative to system $O_2x_2y_2z_2$.

The origin of coordinate system $O_4x_4y_4z_4$ is connected with screw 4 and located in joint 3-4, where axes y_3 and y_4 are coincident. The position of coordinate system $O_4x_4y_4z_4$ in system $O_3x_3y_3z_3$ is defined with the following Denavit and Hartenberg matrix:

$$\mathbf{T}^{(4,3)} = \begin{pmatrix} 1 & 0 & 0 & 0 \\ 0 & \cos\varphi_3 & 0 & -\sin\varphi_3 \\ 0 & 0 & 1 & 0 \\ 0 & \sin\varphi_3 & 0 & \cos\varphi_3 \end{pmatrix}, \quad (5)$$

where φ_3 is a variable parameter describing the rotation of screw 4 relative to coupler 3.

The origin of coordinate system $O_5x_5y_5z_5$ is connected with rocker 6 and located in joint 6-1. The position of coordinate system $O_5x_5y_5z_5$ in system $O_4x_4y_4z_4$ is described with the following Denavit and Hartenberg matrix:

$$\mathbf{T}^{(5,4)} = \begin{pmatrix} 1 & 0 & 0 & 0 \\ 0 & \cos\varphi_3 & 0 & \sin\varphi_3 \\ S & 0 & 1 & 0 \\ 0 & -\sin\varphi_3 & 0 & \cos\varphi_3 \end{pmatrix}, \quad (6)$$

where S is a variable parameter describing the distance between joints 3-4 and 4-6. Parameters S and φ_3 are linked through screw pitch p, which is a given parameter.

The position of coordinate system $O_1x_1y_1z_1$ in system $O_5x_5y_5z_5$ is described with the following Denavit and Hartenberg matrix:

$$\mathbf{T}^{(1,5)} = \begin{pmatrix} 1 & 0 & 0 & 0 \\ a+b & 1 & 0 & 0 \\ -l_1\cos\varphi_4 & 0 & \cos\varphi_4 & -\sin\varphi_4 \\ -l_1\sin\varphi_4 & 0 & \sin\varphi_4 & \cos\varphi_4 \end{pmatrix}, \quad (7)$$

where φ_4 is a variable parameter describing the rotation of rocker 6 relative to fixed link 1; l_1 is the length of fixed link 1.

The closedness equation of the closed contour of the investigated mechanism is written as:

$$\mathbf{T}^{(2,1)}\mathbf{T}^{(3,2)}\mathbf{T}^{(4,3)}\mathbf{T}^{(5,4)}\mathbf{T}^{(1,5)} = \mathbf{E}, \quad (8)$$

where $\mathbf{E}$ is identity matrix.

The position of end point N at screw 4 (Fig. 3) in coordinate system $O_1x_1y_1z_1$ is defined by radius-vector $\bar{r}_N$ from the following equation:

$$\overline{r}_N = \begin{pmatrix} 1 \\ a+b \\ y_{1N} \\ z_{1N} \end{pmatrix} = \mathbf{T}^{(2,1)}\mathbf{T}^{(3,2)}\mathbf{T}^{(4,3)} \begin{pmatrix} 1 \\ 0 \\ l_4 \\ 0 \end{pmatrix}, \quad (9)$$

where y_{1N} and z_{1N} are coordinates of point N in system $O_1x_1y_1z_1$; l_4 is the length of screw 4. The numerical values of angles φ_2, φ_3, φ_4 and displacement S are found from Eq. (8).

3 RESULTS AND DISCUSSION

For the numerical calculation, the following parameters have been accepted: l_1=600 mm, l_2=300 mm, l_3=246 mm, l_4=1040 mm, a=40 mm, b=25 mm, and p=100 mm. Table 1 provides the numerical values of angles φ_2, φ_3, φ_4, displacement S, coordinates y_{1N}, z_{1N} and the length of radius-vector $\overline{r}_N$ depending on angle φ_1.

Fig. 4 provides a graphical interpretation of the dependences of angles φ_2, φ_3, φ_4 and displacement S on angle φ_1, defining a position of the driving link. These graphics have are in accordance with the analytical values shown in Table 1.

Based on the obtained results, a spatial motion trajectory of blade 5 has been analytically reproduced. It is presented in Fig. 5 relative to base coordinates $O_1x_1y_1z_1$ having a centre in joint 1-2. The motion trajectory in Fig. 5 is fundamentally different from

Table 1. *Numerical values of variable parameters (φ_2, φ_3, φ_4, S, y_{1N}, z_{1N} and r_{1N}) depending on angle φ_1 for twelve positions of mixing mechanism*

φ_1 [deg]	φ_2 [deg]	φ_3 [deg]	φ_4 [deg]	S [mm]	y_{1N} [mm]	z_{1N} [mm]	r_{1N} [mm]
0	48.06	39.07	48.06	624.16	877.29	–309.33	930.23
30	28.24	–532.05	58.24	457.79	906.50	–495.00	1032.84
60	5.18	–1191.86	65.18	278.93	919.42	–690.80	1150.02
90	–34.97	–1576.95	55.03	171.96	1097.56	–711.29	1307.89
120	–102.40	–1191.86	17.60	278.93	1325.46	230.10	1345.28
150	–151.76	–532.04	–1.76	457.79	1181.94	17.93	1182.08
180	–185.07	39.04	–5.07	624.16	1014.22	36.73	1014.89
210	–211.06	520.92	–1.06	754.70	885.25	5.30	885.27
240	–233.54	818.86	6.46	837.46	801.25	–22.8	801.57
270	–254.15	879.21	15.85	865.78	767.60	–47.59	769.07
300	–273.74	818.86	26.26	837.46	781.64	–89.60	786.76
330	–292.85	520.92	37.15	754.70	827.41	–172.29	845.16

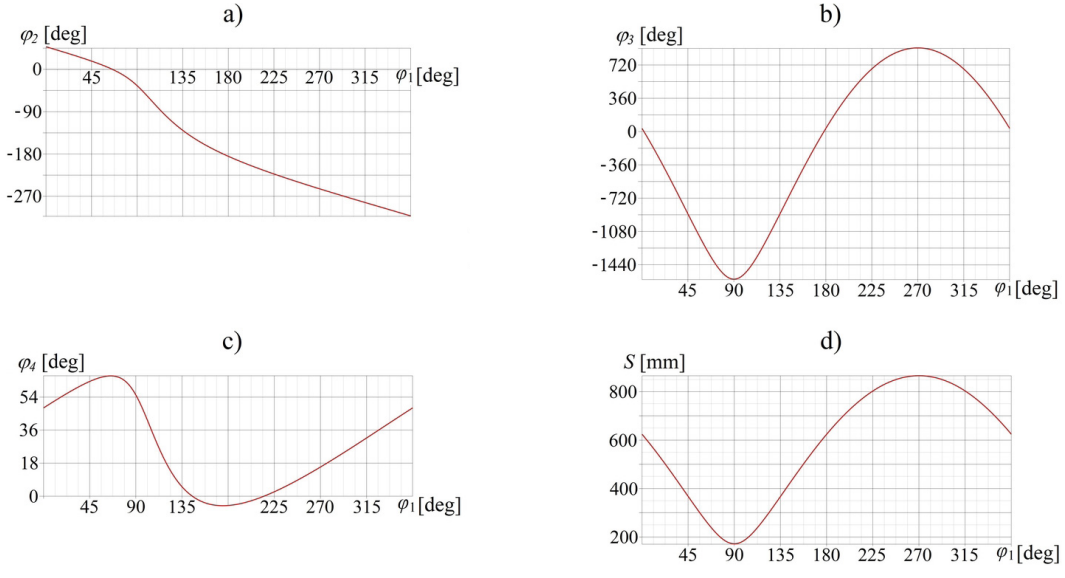

Fig. 4. *Graphical interpretation of dependences of variable parameters: a) φ_2, b) φ_3, c) φ_4, and d) S on angle φ_1*

motion trajectories reproduced by conventional screw mechanisms, proposed in [20] and [21], where the geometric axes of end-effector motions are rectilinear. In the developed mechanism, this axis is made as a closed curvilinear line, the geometry of which is determined by lengths of links l_1, l_2, l_3 and l_4. When changing these parameters, such a trajectory can be varied.

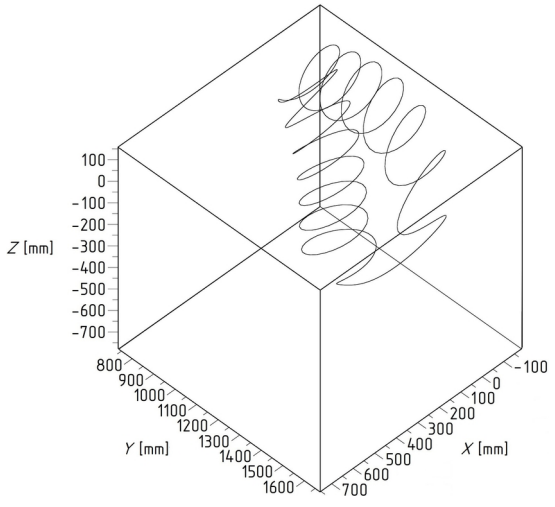

Fig. 5. *Analytical motion trajectory of the end-effector that defines the working zone of the mixing mechanism*

The results of analytical calculations have been verified using simulation modelling in this study. Specifically, the analytical trajectory of the end-effector presented in Fig. 5 has been reproduced through CAD modelling. Fig. 6 provides a simulated motion trajectory of the mixing mechanism, where the left figure shows the trajectory of the single blade, while the right one shows the trajectories of the four blades. A comparison of analytical and simulated trajectories provides their identity: the simulated trajectory entirely duplicates the analytical one.

4 CONCLUSIONS

This study presents a new single-driven mixing mechanism, which includes a minimum number of movable links and joints. To ensure design simplicity and speedwork of this mechanism, all links have been created as double-paired and interconnected only by one-DoF joints. The end-effector is designed as a screw that is set between movable links in the kinematic chain of the mechanism. This placement of the end-effector provides its increased working zone.

Analytical kinematics of the developed mechanism has been solved, and the spatial trajectory of the end-effector that determines its working zone has been reproduced. The trajectory has also been obtained through simulation modelling, which verified analytical calculations. The developed mechanism can be widely applied in various mixing operations and can be used in the food, medical, chemical, and construction industries, as well as in agriculture as a device for creating homogeneous materials and

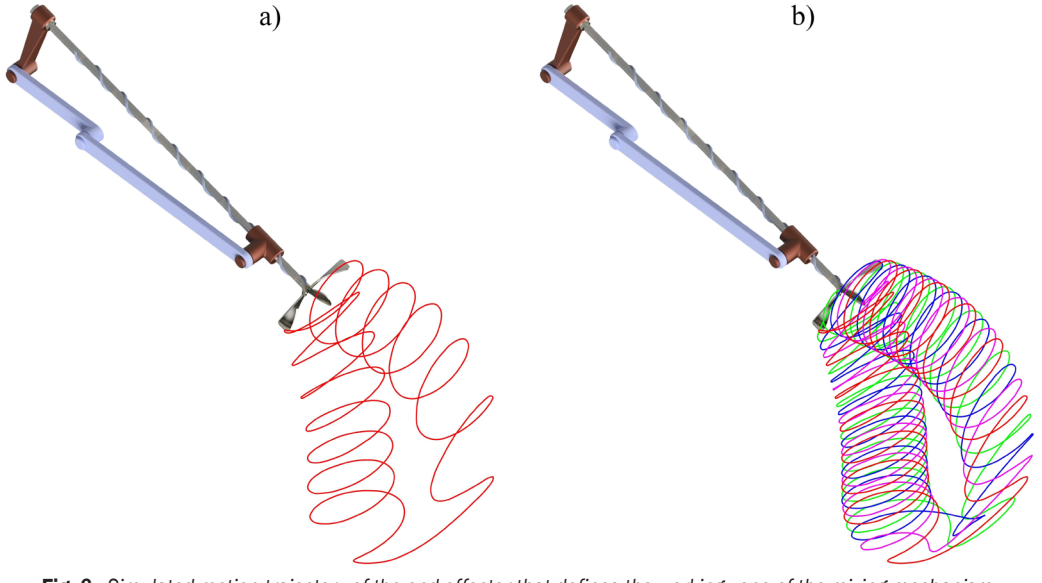

Fig. 6. *Simulated motion trajectory of the end-effector that defines the working zone of the mixing mechanism: a) trajectory of the single blade, and b) trajectories of the four blades*

levelling the concentrations and temperature of mixed substances.

5 ACKNOWLEDGEMENTS

The reported study was funded by *RFBR* according to the research project № 18-31-00440.

6 REFERENCES

[1] Gogu, G. (2004). Structural synthesis of fully-isotropic translational parallel robots via theory of linear transformations. *European Journal of Mechanics - A/Solids*, vol. 23, no. 6, p. 1021-1039, **DOI:10.1016/j.euromechsol.2004.08.006**.

[2] Zeng, Q., Fang, Y. (2012). Structural synthesis and analysis of serial-parallel hybrid mechanisms with spatial multi-loop kinematic chains. *Mechanism and Machine Theory*, vol. 49, p. 198-215, **DOI:10.1016/j.mechmachtheory.2011.10.008**.

[3] Fomin A., Ivanov W., Paik J. (2017). Design of five-bar screw-lever manipulator and optimization of its output link path of motion. *Procedia Engineering*, vol. 206, p. 1703-1708, **DOI:10.1016/j.proeng.2017.10.701**.

[4] Angeles, J. (1987). *Fundamentals of Robotic Mechanical Systems: Theory, Methods and Algorithms*. Springer, New York, **DOI:10.1007/978-3-319-01851-5**.

[5] Saggere, L., Kota, S. (2001). Synthesis of planar, compliant four-bar mechanisms for compliant-segment motion generation. *Journal of Mechanical Design*, vol. 123, no. 4, p. 535-541, **DOI:10.1115/1.1416149**.

[6] Fomin, A., Paramonov, M. (2016). Synthesis of the four-bar double-constraint mechanisms by the application of the grubler's method. *Procedia Engineering*, vol. 150, p. 871-877, **DOI:10.1016/j.proeng.2016.07.034**.

[7] Rhyu, J.H., Kwak, B.M. (1988). Optimal stochastic design of four-bar mechanisms for tolerance and clearance. *Journal of Mechanisms, Transmissions, and Automation in Design*, vol. 110, no. 3, p. 255-262, **DOI:10.1115/1.3267455**.

[8] Castejón, C., Carbone, G., García Prada, J.C., Ceccarelli, M. (2010). A multi-objective optimization of a robotic arm for service tasks. *Strojniski vestnik - Journal of Mechanical Engineering*, vol. 56, no. 5, p. 316-329.

[9] Gileta, V.P., Choosovitin, N.A. (2008). Parametric analysis of device for the mixing with the equal angles overlap and pressure. *Proceedings* of the *Third International Forum on Strategic Technologies*, p. 414-416, **DOI:10.1109/IFOST.2008.4602954**.

[10] Kheilo, S.V., Glazunov, V.A., Shirinkin, M.A., Kalendarev, A.V. (2013). Possible applications of mechanisms of parallel structure. *Journal of Machinery Manufacture and Reliability*, vol. 42, no. 5, p. 359-363, **DOI:10.3103/S1052618813050063**.

[11] Fomin, A., Dvornikov, L., Paramonov, M., Jahr, A. (2012). To the theory of mechanisms subfamilies. *IOP Conference Series: Materials Science and Engineering*, vol. 124, no. 1, **DOI:10.1088/1757-899X/124/1/012055**.

[12] Li, S., Dai, J.-S. (2012). Structure synthesis of single-driven metamorphic mechanisms based on the augmented assur groups. *Journal of Mechanisms and Robotics*, vol. 4, no. 3, 031004, **DOI:10.1115/1.4006741**.

[13] Dvornikov, L.T. (2008). Towards question about classification of planar Assur groups. *Theory of Mechanisms and Machines*, vol. 2, no. 6, p. 18-25.

[14] Kong, X., Gosselin, C.M. (2004). Type synthesis of 3T1R 4-DOF parallel manipulators based on screw theory. *IEEE Transactions on Robotics and Automation*, vol. 20, no. 2, p. 181-190, **DOI:10.1109/TRA.2003.820853**.

[15] Pierrot, F., Company, O. (1999). H4: a new family of 4-DOF parallel robots. *IEEE/ASME International Conference on Advanced Intelligent Mechatronics*, p. 508-513, **DOI:10.1109/AIM.1999.803222**.

[16] Rey, L., Clavel R. (1999). The Delta Parallel Robot. Boër, C.R., Molinari-Tosatti, L., Smith, K.S. (eds), *Parallel Kinematic Machines. Advanced Manufacturing*. Springer, London, p. 401-417, **DOI:10.1007/978-1-4471-0885-6_29**.

[17] Meneses, J., Castejón, C., Corral, E., Rubio, H., García-Prada, H.C. (2011). Kinematics and dynamics of the quasi-passive biped "PASIBOT". *Strojniški vestnik - Journal of Mechanical Engineering*, vol. 57, no. 12, p. 879-887, **DOI:10.5545/sv-jme.2010.210**.

[18] Cheng, G., Xu, P., Yang, D., Li, H., Liu, H. (2013). Analysing kinematics of a novel 3CPS parallel manipulator based on rodrigues parameters. *Strojniški vestnik - Journal of Mechanical Engineering*, vol. 59, no. 5, p. 291-300, DOI:10.5545/sv-jme.2012.727.

[19] Fomin, A., Paramonov, M. (2019). Structural and kinematic analysis of internal surfaces cutting. *Journal of Machinery Manufacture and Reliability*, vol. 4, p. 14-21, **DOI:10.1134/S0235711919040072**.

[20] Jones, M.H., Velinsky, S.A. (2012). Kinematics of roller migration in the planetary roller screw mechanism. *Journal of Mechanical Design*, vol. 134, no. 6, 061006, **DOI:10.1115/1.4006529**.

[21] Wei, C.C., Lin, J.F. (2004). Kinematic analysis of the ball screw mechanism considering variable contact angles and elastic deformations. *Journal of Mechanical Design*, vol. 125, no. 4, p. 717-733, **DOI:10.1115/1.1623761**.

Vsebina

Strojniški vestnik - Journal of Mechanical Engineering
letnik 65, (2019), številka 5
Ljubljana, maj 2019
ISSN 0039-2480

Izhaja mesečno

Razširjeni povzetki (extended abstracts)

Jernej Klemenc, Bojan Podgornik: Izboljšan model za napoved S-N krivulj in njihovih raztrosov SI 35
Xi Zhang, Tianlu Zhang, Xiangyu Geng, Jianfeng Hong, Jinjun Wu: Študija vplivov hierarhične valovite morfologije na pretok skozi reže SI 36
Xianbin Du, Youqun Zhao, Qiang Wang, Hongxun Fu, Fen Lin: Lastnosti stika s podlago nepnevmatskega mehanskega elastičnega kolesa s previsom med kotaljenjem SI 37
Jiwen Chen, Xin Li, Hongjuan Yang, Chen Wang: Inovativna zasnova vertikalnega in transverzalnega dvigala v dvojnih jaških na osnovi teorije TRIZ SI 38
Abdulrahaman Shuaibu Ahmad, Wu Yunxin, Gong Hai, Liu Lei: Ugotavljanje vpliva hladnega tlačnega preoblikovanja na zmanjšanje preostalih napetosti v bloku iz gašene aluminijeve zlitine 2219 SI 39
Alexey Fomin, Wsevolod Ivanov: Razvoj mešalnega mehanizma s kompleksnim gibanjem vrha SI 40

Strojniški vestnik - Journal of Mechanical Engineering 65(2019)5, SI 35

Prejeto v recenzijo: 2018-12-07
Prejeto popravljeno: 2019-04-24
Odobreno za objavo: 2019-05-10

Izboljšan model za napoved S-N krivulj in njihovih raztrosov

Jernej Klemenc[1,*] – Bojan Podgornik[2]
[1]Univerza v Ljubljani, Fakulteta za strojništvo, Slovenija
[2]Inštitut za kovinske materiale in tehnologije, Slovenija

Za zanesljivo napoved dobe trajanja izdelka je treba poznati njegovo geometrijo, obremenitveno stanje in zdržljivost materiala. Zdržljivost materiala pri ponavljajočih se obremenitvah opišemo s S-N krivuljo. Zaradi različnih naključnih dejavnikov, ki vplivajo na dinamično trdnost materiala, ima S-N krivulja vedno določen raztros okoli povprečnega trenda. Poznavanje tega raztrosa je nujno za napoved mejne dobe trajanja pri ponavljajočih se obremenitvah.

V članku je predstavljen nadgrajen model nevronske mreže, s katerim je mogoče modelirati S-N krivulje in njihov raztros v področju časovne trdnosti in trajne dinamične trdnosti. Pri tem model upošteva povečanje raztrosa dinamične trdnosti na prehodu iz časovne v trajno dinamično trdnost. Raztros S-N krivulje je modeliran z dvoparametrično Weibullovo gostoto porazdelitve verjetnosti, pri kateri sta tako parameter velikosti kot parameter oblike odvisna ob obremenitvenega nivoja. Parameter velikosti je modeliran s funkcijo, ki je izpeljana iz Coffin-Mansonove enačbe, parameter oblike pa je modeliran z modificirano logistično funkcijo. Celoten model je tako opisan s sedmimi parametri, ki jih je potrebno določiti s pomočjo eksperimentalnih podatkov. Ta model S-N krivulje in njenega raztrosa je bil nato zaporedno vgrajen v nevronsko mrežo z večravninskim perceptronom. Na ta način smo upoštevali odvisnost parametrov S-N krivulje in njenega raztrosa od proizvodnega postopka materiala. V članku sta z ustreznimi enačbami prikazana in razložena tako model S-N krivulje in njenega raztrosa kot tudi uporabljena zaporedna hibridna nevronska mreža.

Predstavljeni model smo preskusili na primeru vzmetnega jekla 51CrV4. Polizdelki za preizkušance so bili izdelani z dvema različnima postopkoma: na konvencionalni način in z elektro-pretaljevanjem pod žlindro. Ohlajanje polizdelkov je bilo izvedeno z dvema različnima hitrostima. Za množico eksperimentalnih podatkov smo najprej določili S-N krivulje in njihove raztrose ločeno za vsako kombinacijo proizvodnega procesa in hitrosti ohlajanja. Kljub temu, da je bilo kar nekaj eksperimentalnih rezultatov nepopolnih (t.j. da ni prišlo do utrujenostnega loma pred koncem preskusa) smo z modelom ustrezno opisali tako trende S-N krivulj, kot tudi njihove raztrose v vsem območju amplitudnih napetosti. Nato smo izdelali enovit model s prej omenjeno zaporedno hibridno nevronsko mrežo. Ugotovili smo, da je z uporabljeno nevronsko mrežo mogoče dobro modelirati odvisnost S-N krivulj in njihovih raztrosov od proizvodne tehnologije. Kot problematična se je izkazala le kombinacija proizvodnega procesa in hitrosti hlajenja, ki je rezultirala v večjem številu nepopolnih podatkov pri utrujenostnih preskusih. Če je nabor eksperimentalnih podatkov omejen, je treba uporabiti manjšo topologijo nevronske mreže, kar lahko vpliva na njeno sposobnost generalizacije.

Inovativnost predstavljene raziskave se kaže v dveh točkah: i.) s samo sedmimi parametri modela smo uspeli konsistentno modelirati prehod S-N krivulje in njenega raztrosa iz časovne trdnosti v trajno dinamično trdnost, česar še nismo zasledili v ustrezni literaturi; ii.) predstavljeni model smo vgradili v zaporedno hibridno nevronsko mrežo, izpeljali ustrezne enačbe za učenje nevronske mreže in pokazali, da je mogoče parametre modela S-N krivulje in njenega raztrosa povezati s proizvodnimi tehnologijami, ki so bile uporabljene za izdelavo materiala preizkušancev. V prihodnosti želimo model preveriti še za druge vrste kovinskih in polimernih materialov.

Ključne besede: jeklo 51CrV4, konvencionalne izdelovalne tehnologije, elektro-pretaljevanje pod žlindro, S-N krivulja, zaporedna hibridna nevronska mreža

*Naslov avtorja za dopisovanje: Univerza v Ljubljani, Fakulteta za strojništvo, Aškerčeva 6, 1000 Ljubljana, Slovenija, jernej.klemenc@fs.uni-lj.si

Strojniški vestnik - Journal of Mechanical Engineering 65(2019)5, SI 36

Prejeto v recenzijo: 2018-12-17
Prejeto popravljeno: 2019-03-18
Odobreno za objavo: 2019-04-11

Študija vplivov hierarhične valovite morfologije na pretok skozi reže

Xi Zhang[1,*] – Tianlu Zhang[1] – Xiangyu Geng[1] – Jianfeng Hong[1] – Jinjun Wu[2]
[1]Kitajska rudarska in tehniška univerza, Šola za mehaniko, elektroniko in informatiko, Kitajska
[2]Kitajska znanstveno-tehniška strojniška akademija, Kitajska

Majhna viskoznost vode je povezana s slabo mazalnostjo in povečanim puščanjem skozi reže. Veliko naporov je bilo vloženih v izboljševanje triboloških lastnosti in tesnjenja s premišljeno zasnovo morfologije površin, manj pozornosti pa je bilo posvečene vplivom hierarhične morfologije na tok skozi reže. Mnoge biološke snovi imajo hierarhično strukturo z valovito morfologijo in v članku je podan predlog hierarhične sinusne morfologije za oblikovanje rež med sosednjimi površinami delov vodnih hidravličnih sistemov, za katere je zaradi manjše viskoznosti vode značilna slabša mazalnost in večja lekaža. Navdih zanje so bile omenjene posebne naravne hierarhične strukture.

Oblikovani so bili trije sinusni modeli ničtega, prvega in drugega reda. Za model prvega reda je za razliko od modela ničtega reda značilna sinusna valovitost z amplitudo A_1 in valovno dolžino λ_1. Pri sinusni valovitosti drugega reda je na sinusno površino prvega reda naložena še dodatna sinusna struktura z amplitudo $A_2 < A_1$ in valovno dolžino $\lambda_2 < \lambda_1$. Preizkušanci s sinusno strukturo ničtega, prvega in drugega reda so bili izdelani s 3D-tiskalnikom Lite 600 3D z natančnostjo 0,05 mm, uporabljen pa je bil material akrilonitril butadien stiren (ABS). Lekaža skozi reže modelov s sinusnimi strukturami ničtega, prvega in drugega reda je bila določena na hidravličnem preizkuševališču z obročasto režo.

Opravljena je bila tudi numerična analiza vpliva valovitih površin različnih amplitud in valovnih dolžin na lekažo s komercialnim paketom za CFD ANSYS FLUENT. Q_0, Q_1 in Q_2 so lekažni tokovi ničtega, prvega in drugega reda. Parameter ε_1 je definiran kot razmerje A_1/λ_1. Najmanjši lekažni tok Q_1 je bil dosežen pri vrednostih $A_1 = 1$ mm in $\varepsilon_1 = 4$, relativno zmanjšanje toka ($1 = Q_1/Q_0$) pa je bilo 43,3-odstotno. Parameter ε_2 je definiran kot razmerje A_2/λ_2. Lekaže pri modelih drugega reda so bile manjše kot pri modelih prvega reda. Največja stopnja zmanjšanja lekaže ($1 = Q_2/Q_1$) je znašala 18 %, kar pomeni, da lahko sinusna morfologija drugega reda učinkovito izboljša učinkovitost tesnjenja.

Nadaljnje študije pretočnega polja so pokazale, da so za občutno zmanjšanje lekaže pri sinusni strukturi drugega reda zaslužni dodatni vrtinci različnih velikosti v valovitih dolinah drugega reda, kjer se porazgubi več kinetične energije fluida. Ti vrtinci so torej mehanizem, ki prispeva k zmanjšanju lekaže. K manjši lekaži prav tako prispevata manjša širina glavnega toka in manjša komponenta hitrosti X pri modelih drugega reda v primerjavi z modeli prvega reda. Valovite površine poleg tega povzročajo variabilno debelino filma fluida, s tem pa prispevajo k dodatni nosilnosti in zmanjšujejo obrabo.

V članku je podan predlog hierarhične sinusne morfologije za oblikovanje rež med sosednjimi površinami. Preučen je vpliv valovitosti površine z različnimi amplitudami in valovnimi dolžinami na lekažo. Rezultati eksperimentov in simulacij kažejo, da lahko hierarhične sinusne strukture v režah med sosednjimi površinami prispevajo k zmanjšanju lekaže. Pozitiven vpliv hierarhičnih valovitih površin kaže na ogromen potencial za zmanjšanje energijskih izgub v hidravličnih sistemih in odpira nov pristop k snovanju rež med sosednjimi površinami.

Ključne besede: hierarhična sinusna morfologija, pretok skozi režo, voda, lekaža

*Naslov avtorja za dopisovanje: Kitajska rudarska in tehniška univerza, Šola za mehaniko, elektroniko in informatiko, Peking, Kitajska, zhangx@cumtb.edu.cn

Strojniški vestnik - Journal of Mechanical Engineering 65(2019)5, SI 37

Prejeto v recenzijo: 2018-11-28
Prejeto popravljeno: 2019-03-22
Odobreno za objavo: 2019-04-03

Lastnosti stika s podlago nepnevmatskega mehanskega elastičnega kolesa s previsom med kotaljenjem

Xianbin Du[1,*] –Youqun Zhao[2] – Qiang Wang[1] - Hongxun Fu[3] – Fen Lin[2]

[1]Znanstveno tehniška univerza v Shandongu, Kolidž za transport, Kitajska
[2]Univerza za aeronavtiko in astronavtiko v Nanjingu, Kolidž za energetiko in elektroenergetiko, Kitajska
[3]Tehniška univerza v Shandongu, Šola za transport in avtomobilsko tehniko, Kitajska

Stik kolesa s podlago vpliva na kotalni upor, enakomernost obrabe ter na vodljivost in stabilnost vozila. Inovativno nepnevmatsko mehansko elastično kolo »ME« odpravlja dejavnike tveganja v primeru preboda, uhajanja zraka ali celo eksplozije tradicionalnih pnevmatik. V članku je predstavljena raziskava lastnosti stika s podlago kolesa ME s previsom med prostim kotaljenjem, zaviranjem in vožnjo, ki je bila opravljena s simulacijo po metodi končnih elementov (MKE) in eksperimentalno. Kolo ME s svojo konstrukcijo zagotavlja udobje in manevrirne sposobnosti običajnih pnevmatik, obenem pa tudi vzdržljivost in obstojnost proti poškodbam, kot je značilna za kolesa, ki niso polnjena z zrakom.

Model kolesa ME po MKE je bil postavljen na osnovi konstitutivnega modela Mooney-Rivlin in opisuje vedenje gumijastega materiala. Kompozit gume in elastičnih ojačitvenih obročev je bil simuliran po modelu armature. Preizkušena je bila tudi togost kolesa ME za preverjanje točnosti in zanesljivosti modela po MKE. Prednosti kolesa ME so bile določene v primerjavi z referenčno pnevmatiko, ki je bila prav tako modelirana po MKE. Napovedane lastnosti stika s podlago za obe kolesi z različnim kotom previsa so bile analizirane in primerjane za pogoje prostega kotaljenja, zaviranja in vožnje. Uporabljene so bile tudi različne vrednosti zdrsa kolesa ME in pnevmatike v pogojih vožnje za analizo vpliva zdrsavanja na stik s podlago.

Rezultati so pokazali, da je tlak kolesa ME na podlago med prostim kotaljenjem simetričen glede na srednjico po širini območja stika s podlago. Tlak kolesa ME in pnevmatike na podlago se s povečevanjem kota previsa koncentrira na strani kotaljenja, enakomernost porazdelitve tlaka pa postopoma izginja. Zato je treba tako pri kolesu ME kakor tudi pri pnevmatiki računati z neenakomernim obrabljanjem tekalne površine. Hitrost premikanja največjega tlaka na podlago kolesa ME v pogojih prostega kotaljenja je bistveno manjša kot pri pnevmatiki, zaradi česar je koncentracija tlaka pri velikem kotu previsa pri pnevmatiki intenzivnejša kot pri kolesu ME, posledično pa je večja tudi obraba tekalne površine. Vpliv kota previsa na porazdelitev tlaka v pogojih zaviranja pri kolesu ME je podobna kot v pogojih prostega kotaljenja, toda porazdelitev ni več simetrična glede na srednjico po širini stika s podlago in območje visokega tlaka se postopoma premika v smeri gibanja. Smer gibanja območja visokega tlaka med vožnjo je pri kolesu ME nasprotna kot pri zaviranju in se premika proti zadnjemu delu območja stika s podlago. Poleg tega največji tlak v območju stika pri nespremenjenem kotu previsa raste s povečevanjem vrednosti zdrsa.

Rezultati raziskave so pomembna osnova za optimizacijo konstrukcije in celovito analizo mehanskih lastnosti kolesa ME. V modelu ni bil upoštevan vzorec tekalne površine, zato bodo prihodnje raziskave osredotočene na preučevanje vpliva različnih vzorcev na stik kolesa ME s podlago.

Ključne besede: kolo, lastnosti stika s podlago, analiza po metodi končnih elementov, kontaktni tlak, kot previsa, obraba tekalne površine

*Naslov avtorja za dopisovanje: Znanstveno tehniška univerza v Shandongu, Kolidž za transport, Qingdao, Kitajska, duxianbin@sdust.edu.cn

Strojniški vestnik - Journal of Mechanical Engineering 65(2019)5, SI 38

Prejeto v recenzijo: 2018-12-18
Prejeto popravljeno: 2019-03-22
Odobreno za objavo: 2019-05-07

Inovativna zasnova vertikalnega in transverzalnega dvigala v dvojnih jaških na osnovi teorije TRIZ

Jiwen Chen[1,2] – Xin Li[1,2] – Hongjuan Yang[3] – Chen Wang[1,2]

[1]Univerza Shandong Jianzhu, Soinovacijsko središče za zelene gradnje province, Kitajska
[2]Univerza Shandong Jianzhu, Šola za strojništvo in elektroniko, Kitajska
3Univerza Chongqing Jiaotong, Šola za informatiko in elektrotehniko, Kitajska

Klasična dvigala rešujejo le problem vertikalnega transporta in uporabniki se morajo po izstopu iz dvigala še vedno sprehoditi do svojega cilja. Zaradi nezmožnosti gibanja dvigal v horizontalni smeri je omejena pretočnost med dvigali v različnih jaških. V članku je predstavljena inovativna zasnova vertikalnih in transverzalnih dvigal v dvojnih jaških na osnovi teorije TRIZ, ki zagotavlja nizke stroške in široko uporabnost. Za izboljšanje učinkovitosti transporta potnikov med oddaljenimi jaški je predstavljena in verificirana strategija vodenja dvigal z opisano zasnovo.

Vpeljani so funkcijski modeli, kavzalna analiza, analiza protislovij, model Su-Field in druga orodja po teoriji TRIZ, ki omogočajo inoviranje z izhodiščem v klasičnih dvigalih. Predlagana je zasnova vertikalnega in transverzalnega dvigala z dvojnimi jaški in ustrezno strategijo vodenja. Razvita je bila tudi platforma za simulacije dvigala v programskem jeziku C#, ki omogoča preučevanje operativne učinkovitosti pri različnih prometnih režimih in transverzalnih razdaljah.

Ključne težave, ki jih je treba razrešiti, so identificirane s funkcionalnimi modeli in kavzalno analizo. Analitični in transformacijski problemi so razrešeni po modelu Su-Field. Pot do rešitve problema je vključevala analizo protislovij, ki ji je sledilo preverjanje izvedljivosti rešitve s simulacijami.

Rezultati simulacij kažejo, da lahko vertikalno in transverzalno dvigalo izboljša učinkovitost transporta potnikov v horizontalni smeri, občutno pa se izboljša tudi mobilnost za vse potnike. S povečevanjem transverzalne razdalje se izboljšuje mobilnost vseh uporabnikov predlaganega dvigala. Transverzalna kabina v navzkrižni strategiji vodenja vertikalnega in transverzalnega dvigala pri odzivu na potnikov klic ne loči med horizontalno in vertikalno smerjo potnikovega premika. Uporabniki običajnih dvigal morajo nasprotno počakati, če se dvigalo trenutno premika v smeri, ki je nasprotna želeni smeri vožnje. Povprečni čas vertikalnega gibanja je tako lahko pri vertikalnem in transverzalnem dvigalu krajši kot pri običajnih dvigalih. Povprečni čakalni čas za vertikalne potnike pri vertikalnem in transverzalnem dvigalu je krajši kot pri običajnih dvigalih, če znaša transverzalna razdalja 400 m in je transverzalna gostota p večja od 0,4. V prihodnje bo mogoče opraviti bolj poglobljene raziskave tega pojava ter optimizirati strategijo vodenja v režimu pretežnega spuščanja uporabnikov za skrajšanje povprečnega čakalnega časa vertikalnih potnikov in izboljšanje operativne učinkovitosti.

Problem vertikalnega in horizontalnega delovanja dvigala je razrešen na osnovi teorije TRIZ. Modeli pretoka vertikalnih in horizontalnih potnikov so pripravljeni s Poissonovo porazdelitvijo in po metodi Monte Carlo. Učinkovitost vertikalnega in transverzalnega dvigala v osemnadstropni stavbi je preverjena s simulacijo v programskem jeziku C#. Vertikalno in transverzalno dvigalo lahko učinkovito izboljša učinkovitost transporta potnikov v vodoravni smeri v obravnavanem okolju.

Ključne besede: C#, TRIZ, model Su-Field, transverzalno dvigalo, Poissonova porazdelitev, model pretoka uporabnikov dvigala

*Naslov avtorja za dopisovanje: Univerza Shandong Jianzhu, Soinovacijsko središče za zelene gradnje province, Fengming Road Lingang Development Zone, Jinan, Kitajska, chenjiwen@sdjzu.edu.cn

Strojniški vestnik - Journal of Mechanical Engineering 65(2019)5, SI 39

Prejeto v recenzijo: 2018-12-18
Prejeto popravljeno: 2019-03-29
Odobreno za objavo: 2019-05-07

Ugotavljanje vpliva hladnega tlačnega preoblikovanja na zmanjšanje preostalih napetosti v bloku iz gašene aluminijeve zlitine 2219

Abdulrahaman Shuaibu Ahmad[1,2,*] – Wu Yunxin[1,2] – Gong Hai[1,2] – Liu Lei[2]
[1]Univerza srednjega juga, Kolidž za strojništvo in elektrotehniko, Kitajska
[2]Univerza srednjega juga, Državni laboratorij za visokozmogljivo kompleksno obdelavo, Kitajska

Gašenje se uporablja za zagotavljanje želenih lastnosti kovinskih in plastičnih materialov, denimo za povečanje trdote ali zmanjšanje velikosti kristalnih zrn. Pri tej toplotni obdelavi pa se tvorijo velike preostale napetosti, ki škodujejo odpornosti materiala proti utrujanju in povečajo tveganje odpovedi zaradi obremenitev med obratovanjem. Zato je za doseganje želene zmogljivosti in zanesljivosti materiala zelo pomembno, da se preostale napetosti zmanjšajo na minimum.

V članku je predstavljena analiza možnosti za zmanjšanje preostalih napetosti v aluminijevi zlitini Al 2219 pri različnih kompresijskih razmerjih (CR). Trije preizkušanci, izdelani iz materiala Al 2219, so bili v peči enakomerno ogrevani pri temperaturi 540 °C za štiri ure, nato pa so bili 10 minut gašeni v mirujoči vodi s temperaturo 40 °C. Preostale napetosti po gašenju so bile določene s tehniko vrtanja lukenj po standardu ASTM E837-13a (metoda enakomernih napetosti). Trije preizkušanci so bili nato hladno tlačno preoblikovani pri sobni temperaturi za razbremenitev napetosti.

Metoda ima prednost zato, ker so imeli vsi preizkušanci preprosto geometrijo in vzporedne površine, proces pa je tudi znatno stroškovno ugodnejši od natezanja. Pri preizkušancih 1, 2 in 3 je bilo uporabljeno kompresijsko razmerje (CR) v vrednosti 2, 3 oz. 4 % debeline preizkušanca. Hladno tlačno preoblikovanje je bilo izvedeno v ravnem orodju, temu pa je sledila analiza napetosti.

Rezultati kažejo, da je stopnja razbremenitve preostalih napetosti največja pri 2 % CR, znašala pa je 86,8 %. Plastično deformiranje kovinskega predmeta s tlačnim preoblikovanjem povzroči prerazporeditev preostalih napetosti in s tem njihovo zmanjšanje. Izbira vrednosti CR je odvisna od preoblikovalne trdnosti materiala in opisani rezultati pri izbranih vrednostih CR tako veljajo samo za zlitino Al 2219.

V prihodnjih raziskavah bo mogoče analizirati zmanjšanje preostalih napetosti še pri drugih vrednostih CR, npr. 1 %. Rezultati opisujejo znatno zmanjšanje preostalih napetosti po hladnem tlačnem preoblikovanju, in sicer predvsem komponente napetosti v osi x. Tehnika tlačnega preoblikovanja je omejena na dele s preprostimi oblikami in vzporednimi površinami, debelina obdelovanca pa mora biti manjša od največjega dovoljenega toplotno obdelanega prereza. Preostale napetosti kot posledica različnih proizvodnih procesov vplivajo predvsem na dimenzijsko stabilnost, trajno nihajno trdnost, integriteto ter na mehanske zmogljivosti komponent in konstrukcij, zato jih je treba za doseganje boljših zmogljivosti materiala zmanjševati na sprejemljivo raven. V literaturi ni bilo mogoče najti podatkov o najbolj učinkovitih vrednostih CR za razbremenitev preostalih napetosti v aluminijevi zlitini 2219, ki se uporablja v letalski in vesoljski industriji npr. za izdelavo rezervoarjev za gorivo, kakor tudi pri izdelavi komponent, ki obratujejo pri visokih temperaturah.

V članku je zato predstavljena eksperimentalna analiza za določitev najprimernejših vrednosti CR za zmanjšanje preostalih napetosti v materialu Al 2219.

Ključne besede: gašenje, preostale napetosti, kompresijsko razmerje, Al 2219, hladno tlačno preoblikovanje, metoda vrtanja lukenj

*Naslov avtorja za dopisovanje: Univerza srednjega juga, Kolidž za strojništvo in elektrotehniko, Changsha, Kitajska, wuyunxin@mail.csu.edu.cn

Strojniški vestnik - Journal of Mechanical Engineering 65(2019)5, SI 40

Prejeto v recenzijo: 2018-12-31
Prejeto popravljeno: 2019-04-11
Odobreno za objavo: 2019-05-08

Razvoj mešalnega mehanizma s kompleksnim gibanjem vrha

Alexey Fomin, Wsevolod Ivanov
Sibirska državna industrijska univerza, Rusija

Namen predstavljene študije je razvoj novega mešalnega mehanizma, ki ima en sam pogon in najmanjše število premičnih členov v dvojnih parih, povezanih v sklepe z eno prostostno stopnjo, omogoča pa gibanje vrha po kompleksni prostorski trajektoriji. Namenjena je tudi izboljšanju obstoječih mešalnih mehanizmov z razvojem nove in učinkovite trajektorije gibanja vrha.

Definirana je bila analitična rešitev za sintezo novega mešalnega mehanizma. Rešitev podaja numerične vrednosti za vse komponente predlaganega mehanizma, torej število in vrsto/prostostne stopnje sklepov in členov, glede na različne omejitve in mobilnost celotnega sistema. Novi mehanizem je bil ustvarjen na osnovi te rešitve in načel konstruiranja mehanskih sistemov.

Uporabljen je bil metodološki pristop sinteze konstrukcije mehanskih sistemov za zahtevano mobilnost. Študija vključuje tudi analitične metode kinematične analize oz. metodo matričnih transformacij za identifikacijo različnih kotov in translacije sklepov. Za izvedbo matematičnih transformacij in izračun trajektorije vrha so bila razvita orodja v programu Mathcad, simulacija gibanja in verifikacija analitičnih rezultatov študije pa je bila opravljena s programskimi paketi za CAD.

Predmet študije so algoritmi za sintezo konstrukcij, teorija in metodologija konstruiranja, analitična in računalniška kinematika ter CAD-modeliranje in simulacija.

Rezultat študije je nov mešalni mehanizem z enim samim pogonom, ki ima najmanjše število premičnih členov in sklepov za reprodukcijo kompleksne trajektorije. Vsi členi so za čim preprostejšo zasnovo in hitro delovanje mehanizma povezani v dvojne pare in povezani s sklepi, ki imajo eno samo prostostno stopnjo. Vrh mehanizma je izveden kot polž, ki je umeščen med premičnimi členi v kinematični verigi mehanizma, njegova lega pa omogoča povečanje delovne ovojnice.

V študiji je predstavljena kinematična analiza razvitega mehanizma in identifikacija prostorske trajektorije vrha. Študija prinaša nov pristop k sintezi in analizi, ki ga bo mogoče uporabiti tudi pri drugih ročičnih mehanizmih s štirimi prostostnimi stopnjami ali kompleksno prostorsko trajektorijo vrha.

Razviti mehanizem omogoča pripravo homogenih snovi ter izenačevanje koncentracij in temperature zmesi za številne mešalne operacije v živilski industriji, medicini, kemični industriji in gradbeništvu, kakor tudi v kmetijstvu.

Možni smeri prihodnjih raziskav na tem področju bosta razvoj drugih vrst ročičnih mehanizmov na osnovi pridobljene analitične rešitve in dinamična analiza predlaganega mešalnega mehanizma za opredelitev reakcij v sklepih in momenta pogonskega člena glede na štiri prostostne stopnja vrha mehanizma.

Novosti predstavljene študije so razvoj fundamentalno novega mehanizma s štirimi prostostnimi stopnjami vrha, novi analitični podatki kinematične analize in edinstvena prostorska trajektorija vrha mehanizma. Vrednost študije je tudi v novem algoritmu za sintezo in analizo mehanizmov tega tipa. Predlagani algoritem za sintezo omogoča ustvarjanje podobnih mehanizmov.

Ključne besede: kinematični par, mešalni mehanizem, prostostna stopnja, prostorska trajektorija, analitična kinematika

*Naslov avtorja za dopisovanje: Sibirska državna industrijska univerza, Oddelek za mehaniko in strojništvo, Kirova Str. 42, 654007 Novokuznetsk, Rusija, alexey-nvkz@mail.ru

Information for Authors

All manuscripts must be in English. Pages should be numbered sequentially. The manuscript should be composed in accordance with the Article Template given above. The maximum length of contributions is 10 pages. Longer contributions will only be accepted if authors provide juastification in a cover letter. For full instructions see the Information for Authors section on the journal's website: http://en.sv-jme.eu .

SUBMISSION:

Submission to SV-JME is made with the implicit understanding that neither the manuscript nor the essence of its content has been published previously either in whole or in part and that it is not being considered for publication elsewhere. All the listed authors should have agreed on the content and the corresponding (submitting) author is responsible for having ensured that this agreement has been reached. The acceptance of an article is based entirely on its scientific merit, as judged by peer review. Scientific articles comprising simulations only will not be accepted for publication; simulations must be accompanied by experimental results carried out to confirm or deny the accuracy of the simulation. Every manuscript submitted to the SV-JME undergoes a peer-review process.

The authors are kindly invited to submit the paper through our web site: http://ojs.sv-jme.eu. The Author is able to track the submission through the editorial process - as well as participate in the copyediting and proofreading of submissions accepted for publication - by logging in, and using the username and password provided.

SUBMISSION CONTENT:

The typical submission material consists of:

- A **manuscript** (A PDF file, with title, all authors with affiliations, abstract, keywords, highlights, inserted figures and tables and references),
- Supplementary files:
  - a **manuscript** in a WORD file format
  - a **cover letter** (please see instructions for composing the cover letter)
  - a ZIP file containing **figures** in high resolution in one of the graphical formats (please see instructions for preparing the figure files)
  - possible **appendicies** (optional), cover materials, video materials, etc.

Incomplete or improperly prepared submissions will be rejected with explanatory comments provided. In this case we will kindly ask the authors to carefully read the Information for Authors and to resubmit their manuscripts taking into consideration our comments.

COVER LETTER INSTRUCTIONS:

Please add a **cover letter** stating the following information about the submitted paper:

1. Paper **title**, list of **authors** and their **affiliations**.
2. **Type of paper**: original scientific paper (1.01), review scientific paper (1.02) or short scientific paper (1.03).
3. A **declaration** that neither the manuscript nor the essence of its content has been published in whole or in part previously and that it is not being considered for publication elsewhere.
4. State the **value of the paper** or its practical, theoretical and scientific implications. What is new in the paper with respect to the state-of-the-art in the published papers? Do not repeat the content of your abstract for this purpose.
5. We kindly ask you to suggest at least two **reviewers** for your paper and give us their names, their full affiliation and contact information, and their scientific research interest. The suggested reviewers should have at least two relevant references (with an impact factor) to the scientific field concerned; they should not be from the same country as the authors and should have no close connection with the authors.

FORMAT OF THE MANUSCRIPT:

The manuscript should be composed in accordance with the Article Template. The manuscript should be written in the following format:

- A **Title** that adequately describes the content of the manuscript.
- A list of **Authors** and their **affiliations**.
- An **Abstract** that should not exceed 250 words. The Abstract should state the principal objectives and the scope of the investigation, as well as the methodology employed. It should summarize the results and state the principal conclusions.
- 4 to 6 significant **key words** should follow the abstract to aid indexing.
- 4 to 6 **highlights;** a short collection of bullet points that convey the core findings and provide readers with a quick textual overview of the article. These four to six bullet points should describe the essence of the research (e.g. results or conclusions) and highlight what is distinctive about it.
- An **Introduction** that should provide a review of recent literature and sufficient background information to allow the results of the article to be understood and evaluated.
- A **Methods** section detailing the theoretical or experimental methods used.
- An **Experimental section** that should provide details of the experimental set-up and the methods used to obtain the results.
- A **Results** section that should clearly and concisely present the data, using figures and tables where appropriate.
- A **Discussion** section that should describe the relationships and generalizations shown by the results and discuss the significance of the results, making comparisons with previously published work. (It may be appropriate to combine the Results and Discussion sections into a single section to improve clarity.)
- A **Conclusions** section that should present one or more conclusions drawn from the results and subsequent discussion and should not duplicate the Abstract.
- **Acknowledgement** (optional) of collaboration or preparation assistance may be included. Please note the source of funding for the research.
- **Nomenclature** (optional). Papers with many symbols should have a nomenclature that defines all symbols with units, inserted above the references. If one is used, it must contain all the symbols used in the manuscript and the definitions should not be repeated in the text. In all cases, identify the symbols used if they are not widely recognized in the profession. Define acronyms in the text, not in the nomenclature.
- **References** must be cited consecutively in the text using square brackets [1] and collected together in a reference list at the end of the manuscript.
- **Appendix(-icies)** if any.

SPECIAL NOTES

Units: The SI system of units for nomenclature, symbols and abbreviations should be followed closely. Symbols for physical quantities in the text should be written in italics (e.g. *v*, *T*, *n*, etc.). Symbols for units that consist of letters should be in plain text (e.g. ms^{-1}, K, min, mm, etc.). Please also see: http://physics.nist.gov/cuu/pdf/sp811.pdf .

Abbreviations should be spelt out in full on first appearance followed by the abbreviation in parentheses, e.g. variable time geometry (VTG). The meaning of symbols and units belonging to symbols should be explained in each case or cited in a **nomenclature** section at the end of the manuscript before the References.

Figures (figures, graphs, illustrations digital images, photographs) must be cited in consecutive numerical order in the text and referred to in both the text and the captions as Fig. 1, Fig. 2, etc. Figures should be prepared without borders and on white grounding and should be sent separately in their original formats. If a figure is composed of several parts, please mark each part with a), b), c), etc. and provide an explanation for each part in Figure caption. The caption should be self-explanatory. Letters and numbers should be readable (Arial or Times New Roman, min 6 pt with equal sizes and fonts in all figures). Graphics (submitted as supplementary files) may be exported in resolution good enough for printing (min. 300 dpi) in any common format, e.g. TIFF, BMP or JPG, PDF and should be named Fig1.jpg, Fig2.tif, etc. However, graphs and line drawings should be prepared as vector images, e.g. CDR, AI. Multi-curve graphs should have individual curves marked with a symbol or otherwise provide distinguishing differences using, for example, different thicknesses or dashing.

Tables should carry separate titles and must be numbered in consecutive numerical order in the text and referred to in both the text and the captions as Table 1, Table 2, etc. In addition to the physical quantities, such as *t* (in italics), the units [s] (normal text) should be added in square brackets. Tables should not duplicate data found elsewhere in the manuscript. Tables should be prepared using a table editor and not inserted as a graphic.

REFERENCES:

A reference list must be included using the following information as a guide. Only cited text references are to be included. Each reference is to be referred to in the text by a number enclosed in a square bracket (i.e. [3] or [2] to [4] for more references; do not combine more than 3 references, explain each). No reference to the author is necessary.

References must be numbered and ordered according to where they are first mentioned in the paper, not alphabetically. All references must be complete and accurate. Please add DOI code when available. Examples follow.

Journal Papers:

Surname 1, Initials, Surname 2, Initials (year). Title. Journal, volume, number, pages, DOI code.

[1] Hackenschmidt, R., Alber-Laukant, B., Rieg, F. (2010). Simulating nonlinear materials under centrifugal forces by using intelligent cross-linked simulations. *Strojniški vestnik - Journal of Mechanical Engineering,* vol. 57, no. 7-8, p. 531-538, DOI:10.5545/sv-jme.2011.013.

Journal titles should not be abbreviated. Note that journal title is set in italics.

Books:

Surname 1, Initials, Surname 2, Initials (year). Title. Publisher, place of publication.

[2] Groover, M.P. (2007). *Fundamentals of Modern Manufacturing*. John Wiley & Sons, Hoboken.

Note that the title of the book is italicized.

Chapters in Books:

Surname 1, Initials, Surname 2, Initials (year). Chapter title. Editor(s) of book, book title. Publisher, place of publication, pages.

[3] Carbone, G., Ceccarelli, M. (2005). Legged robotic systems. Kordić, V., Lazinica, A., Merdan, M. (Eds.), Cutting Edge Robotics. Pro literatur Verlag, Mammendorf, p. 553-576.

Proceedings Papers:

Surname 1, Initials, Surname 2, Initials (year). Paper title. Proceedings title, pages.

[4] Štefanić, N., Martinčević-Mikić, S., Tošanović, N. (2009). Applied lean system in process industry. *MOTSP Conference Proceedings*, p. 422-427.

Standards:

Standard-Code (year). Title. Organisation. Place.

[5] ISO/DIS 16000-6.2:2002. *Indoor Air – Part 6: Determination of Volatile Organic Compounds in Indoor and Chamber Air by Active Sampling on TENAX TA Sorbent, Thermal Desorption and Gas Chromatography using MSD/FID.* International Organization for Standardization. Geneva.

WWW pages:

Surname, Initials or Company name. Title, from http://address, date of access.

[6] Rockwell Automation. Arena, from *http://www.arenasimulation.com,* accessed on 2009-09-07.

EXTENDED ABSTRACT:

When the paper is accepted for publishing, the authors will be requested to send an **extended abstract** (approx. one A4 page or 3500 to 4000 characters). The instruction for composing the extended abstract are published on-line: http://www.sv-jme.eu/information-for-authors/ .

COPYRIGHT:

Authors submitting a manuscript do so on the understanding that the work has not been published before, is not being considered for publication elsewhere and has been read and approved by all authors. The submission of the manuscript by the authors means that the authors automatically agree to transfer copyright to SV-JME when the manuscript is accepted for publication. All accepted manuscripts must be accompanied by a Copyright Transfer Agreement, which should be sent to the editor. The work should be original work by the authors and not be published elsewhere in any language without the written consent of the publisher. The proof will be sent to the author showing the final layout of the article. Proof correction must be minimal and executed quickly. Thus it is essential that manuscripts are accurate when submitted. Authors can track the status of their accepted articles on http://en.sv-jme.eu/.

PUBLICATION FEE:

Authors will be asked to pay a publication fee for each article prior to the article appearing in the journal. However, this fee only needs to be paid after the article has been accepted for publishing. The fee is 380 EUR (for articles with maximum of 6 pages), 470 EUR (for articles with maximum of 10 pages), plus 50 EUR for each additional page. The additional cost for a color page is 90.00 EUR. These fees do not include tax.

Strojniški vestnik -Journal of Mechanical Engineering
Aškerčeva 6, 1000 Ljubljana, Slovenia,
e-mail: info@sv-jme.eu

9 770039 248001
ISSN 0039-2480

http://www.sv-jme.eu

Contents

Papers

265 Jernej Klemenc, Bojan Podgornik:
An Improved Model for Predicting the Scattered S-N Curves

276 Xi Zhang, Tianlu Zhang, Xiangyu Geng, Jianfeng Hong, Jinjun Wu:
Study on the Effects of Hierarchical Wavy Morphology on Clearance Flow

287 Xianbin Du, Youqun Zhao, Qiang Wang, Hongxun Fu, Fen Lin:
Grounding Characteristics of a Non-Pneumatic Mechanical Elastic Tire in a Rolling State with a Camber Angle

297 Jiwen Chen, Xin Li, Hongjuan Yang, Chen Wang:
Innovative Design of a Vertical and Transverse Elevator in Double Shafts, Based on TRIZ Theory

311 Abdulrahaman Shuaibu Ahmad, Wu Yunxin, Gong Hai, Liu Lei:
Determination of the Effect of Cold Working Compression on Residual Stress Reduction in Quenched Aluminium Alloy 2219 Block

319 Alexey Fomin, Wsevolod Ivanov:
Development of a Mixing Mechanism with a Complex Motion of the End-effector